AN ECOPHYSIOLOGICAL FRAMEWORK FOR THE MORPHOLOGICAL EVOLUTION OF BLUEGILL SUNFISH

A Dissertation

by

ANTHONY PAPADOPOULOS

Submitted to the Office of Graduate Studies of
Texas A&M University
in partial fulfillment of the requirements for the degree of

DOCTOR OF PHILOSOPHY

May 2007

Major Subject: Wildlife and Fisheries Sciences

AN ECOPHYSIOLOGICAL FRAMEWORK FOR THE MORPHOLOGICAL EVOLUTION OF BLUEGILL SUNFISH

A Dissertation

by

ANTHONY PAPADOPOULOS

Submitted to the Office of Graduate Studies of
Texas A&M University
in partial fulfillment of the requirements for the degree of

DOCTOR OF PHILOSOPHY

Approved by:

Chair of Committee, Thomas J. DeWitt
Committee Members, William H. Neill
Thomas D. Olszewski
Daniel L. Roelke
Head of Department, Thomas E. Lacher

May 2007

Major Subject: Wildlife and Fisheries Sciences

ABSTRACT

An Ecophysiological Framework for the Morphological
Evolution of Bluegill Sunfish. (May 2007)
Anthony Papadopoulos, B.S., Syracuse University;
M.S., Texas A&M University
Chair of Advisory Committee: Dr. Thomas J. DeWitt

Body shape affects the capacity and efficiency of swimming in fishes, and places constraints on foraging and reproductive performance. Hence, fitness components, such as aerobic swimming capacity and efficiency, can be determined from analysis of swimming energetics using active respirometry. In particular, body shape adaptations, such as streamlining, aim at reducing hydrodynamic drag (resistance), thereby increasing swimming efficiency in the presence of water flow, which is a principal contributor to resistance for fish inhabiting rivers. For two populations of bluegill sunfish, one from the Brazos River and the other from Moelman's Slough (a Brazos River oxbow lake), the metabolic transport rate (MTR) was determined to evaluate differences in swimming efficiency. The standard cost of swimming (SCOS) was also determined to evaluate differences in swimming capacity, which represents the overall capacity of the skeletal muscles to generate mechanical power to overcome hydrodynamic resistance. The MTR and the SCOS describe holistic swimming performance, where the MTR specifies the hydrodynamic response due to swimming, and the SCOS specifies the physiologic response due to swimming. The differences in swimming performance are mainly attributed to factors affecting hydrodynamic resistance and could be predicted by morphology; because body shape, like water flow, is also a principal contributor to resistance. Multivariate body shape, from generalized Procrustes analysis, was used to assess the influence of multiple shape traits on swimming costs. This measure of shape related to swimming performance using partial least-squares analysis showed the two

bluegill populations to be significantly different. The results were as follows: the shallow-bodied condition in bluegills was highly correlated with efficient swimming and low swimming capacities; whereas, deep-bodied bluegills were highly correlated with inefficient swimming and high swimming capacities. This is an empirical case of divergent natural selection. For convergence, however, the position of the caudal peduncle is consistent with optimal swimming speed (U_m), which depends on standard metabolic rate (SMR), or metabolic maintenance. Bluegills with erect caudal peduncles have a high range of swimming speeds without suffering much cost of swimming ability compared to bluegills with prone caudal peduncles. The adaptive physiological response to high U_m is due to a low SCOS because swimming efficiency is low and metabolic maintenance is high. In other words, bluegills that are inefficient swimmers and require a high energy intake cannot survive unless they gain the ability to increase their foraging capacity by thrust or metabolic power reduction. This is perhaps one of the most remarkable adaptive physiological responses due to the joint effects of shape and SMR.

This dissertation is dedicated to my family—
parents, Georgia and Sotirios Papadopoulos, sister, Maria, and wife, Kostandina

Από τήν καθοδήγηση, αγάπη, καί στηρίξη, αποκτίσα σοφία.

From their guidance, love, and support, I obtained wisdom.

ACKNOWLEDGEMENTS

I am grateful to my mentor, Thomas DeWitt, who shaped this dissertation by his enthusiasm and patience, and contributed much to my learning; working with him has been a fruitful and wonderful experience. I would like to thank William Neill for providing ideas that became an integral and valuable part of my work on the analysis of the hydrodynamics-based power function and its application in fish swimming energetics. I also would like to thank Thomas Olszewski and Daniel Roelke for providing helpful comments that improved this dissertation. I especially would like to acknowledge my wife, Kostandina, for devotion of her time to assisting with fieldwork vital to the empirical analyses of chapter VI.

TABLE OF CONTENTS

Page

ABSTRACT iii
DEDICATION v
ACKNOWLEDGEMENTS vi
TABLE OF CONTENTS vii
LIST OF FIGURES x
LIST OF TABLES xiii
CHAPTER

I INTRODUCTION 1

Preface 1
Organization 3
Contextualization 3
Eigen- and Singular-Value Decompositions 6
Generalized Procrustes Analysis 10

II DISTORTED REALITY: VISUALIZATION PROBLEMS AND SOLUTIONS IN MULTIVARIATE MORPHOMETRICS 21

Introduction 21
Ordination Methods 22
Burnaby's (1966) Method 27
Objectives 28
Independent Variable Surrogates 28
Burnaby's (1966) Method – Revisited 32
Designed Dataset 36
Results 38
Shared and Unique Features of Diversification 43

CHAPTER Page

III FORCES OF NATURE: BODY SHAPE, WATER FLOW, AND THE CONCEPT OF THE FINENESS RATIO IN FLUID DYNAMICS……55

Introduction 55
Force of Resistance and Body Shape 60
Force of Resistance and Water Flow....62
Specimens....63
Diversification between River and Oxbow Lake 64
Diversification among Oxbow Lakes....69
Diversification of Body Shape in Bluegills....74

IV ON THE HYDRODYNAMICS-BASED POWER FUNCTION……76

Introduction 76
Conceptual Framework 80
Mathematical Framework 82

V ON A UNIFIED MODEL OF ACTIVE RESPIROMETRY……..88

Introduction 88
The Concept of Even and Odd Functions 89
Limit of a Sequence....92

VI BODY SHAPE ADAPTATIONS IN BLUEGILL SUNFISH: TRADE-OFFS BOTH IN SWIMMING PERFORMANCE AND METABOLIC MAINTENANCE…….94

Introduction 94
Materials and Methods 96
Respirometric Analysis 97
Morphometric Analysis....109
Statistical Analysis 110
Covariation between Shape and Respirometric Variables ...116
Discussion 128

CHAPTER Page

VII CONCLUSION……...131

Chapter Synthesis 131

REFERENCES 135

APPENDIX A 141

APPENDIX B 142

VITA 143

LIST OF FIGURES

FIGURE Page

1.1 Three Quadrilaterals in Their Original Configuration 12

1.2 Three Quadrilaterals Translated to Center on Origin 14

1.3 Three Quadrilaterals Translated and Scaled to Unit j(*i*) 16

1.4 Reference Configuration 18

1.5 Three Quadrilaterals Translated, Scaled to Unit j(*i*), and Optimally Rotated 19

2.1 A Design Dataset of Known Shape Deformations: Stretch, Shear, and Trapezoid 37

2.2 Thin-Plate Spline Visualizations Attributable to IVS Predicting the Three Shape Effects along Negative, Neutral, and Positive Gradients of Deformation 38

2.3 Thin-Plate Spline Visualizations Attributable to Predicted PC Scores Describing the Stretch Effect, Shear Effect, and Trapezoid Effect 39

2.4 Thin-Plate Spline Visualizations Attributable to CV Scores Describing the Stretch Effect, Shear Effect, and Trapezoid Effect 40

2.5 Thin-Plate Spline Visualizations Attributable to Burnaby PC Scores Describing the Stretch Effect, Shear Effect, and Trapezoid Effect 41

2.6 An X-Ray of a Typical Bluegill Digitized with 15 Homologous Landmarks Using tpsDig 44

2.7 Thin-Plate Spline Visualizations Attributable to Predicted PC Scores Describing Shared and Unique Features of Shape Diversification between Habitats in Three Species of Sunfish 47

2.8 Thin-Plate Spline Visualizations Attributable to CV Scores Describing Shared and Unique Features of Shape Diversification between Habitats in Three Species of Sunfish 49

FIGURE Page

2.9 Thin-Plate Spline Visualizations Attributable to Burnaby PC Scores Describing Shared and Unique Features of Shape Diversification between Habitats in Three Species of Sunfish…….51

2.10 Uniform Shape Deformation of $X_{\xi 2}$ ……54

3.1 The Relationship of the Relative Contribution of Body Shape, Water Flow, Water Density, and Viscosity to Hydrodynamic Resistance…..……...59

3.2 Thin-Plate Visualizations Attributable to Burnaby PC Scores Describing the Water Flow Shape Effect and the Allometric Shape Effect……67

3.3 Uniform Shape Deformation of $X^{Y}_{\zeta 1}$ ……...……68

3.4 Thin-Plate Spline Visualizations Attributable to Burnaby PC Scores Describing the Third Oxbow Shape Effect and the Fourth Oxbow Shape Effect…….73

3.5 Uniform Shape Deformation of $X^{Z4}_{\zeta 1}$ ……..…….74

3.6 Bluegill River-Oxbow Shape Effect and Potential Metabolic and Hydrodynamic Consequences Associated with the Effect……..75

4.1 A Two-Step Procedure to Determine the Best Value of an Analytically-Derived Estimate of SMR……..……80

6.1 The Relationship between Pseudo-Parameter ψ^{-1} and Tuning Parameter λ……..103

6.2 The Relationship between MTR and the Cubic Hermite Spline Coefficients……..105

6.3 An X-Ray of a Typical Bluegill Sunfish Digitized with 12 Homologous Landmarks Using tpsDig……...109

6.4 Mean-Centered Quadrilateral Described from Matrix A…...…….…....113

FIGURE Page

6.5 Mean-Centered, Rotated, and Compressed Quadrilateral Described from Matrix B…….…….114

6.6 Thin-Plate Spline Visualizations of Singular Warp $\Xi_{W_1}^{1}$ ……..119

6.7 Thin-Plate Spline Visualizations of Singular Warp $\Xi_{W_1}^{2}$ ……..…....120

6.8 Thin-Plate Spline Visualizations of Singular Warp $\Xi_{W_2}^{2}$ ……..…...…124

6.9 Thin-Plate Spline Visualizations of Singular Warp $\Xi_{W_3}^{1}$ ……..…126

7.1 Forces Acting on a Swimming Fish, Where Resistance Over Thrust Represents the Overall Swimming Efficiency……...….....132

7.2 Thin-Plate Spline Visualizations Attributable to Singular Scores from Partial Least-Squares Analysis, Where the Covariation between Shape and SMR, MTR, and SCOS Were Tested Simultaneously……..…...134

LIST OF TABLES

TABLE Page

2.1 Results of Equation 2.31 44

2.2 Euclidean Distances between Three Species of Sunfish and Two Habitats Across $X_{\zeta 2}$, $X_{\zeta 4}^{1}$, and $X_{\zeta 4}^{2}$ 54

3.1 Results of Equation 3.7 65

3.2 Results of Equation 3.14 70

6.1 Results of the MANCOVA 116

CHAPTER I
INTRODUCTION

> *For the harmony of the world is made manifest in Form and Number, and the heart and soul and all poetry of Natural Philosophy are embodied in the concept of mathematical beauty.*
>
> — D'Arcy W. Thompson (1860–1948)

Preface

The pioneering work of D'Arcy W. Thompson and advances in linear algebra gave rise to modern morphometrics (a.k.a., geometric morphometrics), which is multivariate shape analysis. Much of the quantitative work in this dissertation entails multivariate shape analysis of the freshwater sunfish, bluegill (*Lepomis macrochirus*). Using preserved and live specimens and quantitative theoretical models, I had as the principal aim of the research better understanding of how factors contributing to hydrodynamic drag (resistance) could affect inter- and intrademic body shape diversification in bluegill.

Water density, water flow, and viscosity are environmental (extrinsic) factors contributing to hydrodynamic resistance in fish (Newman, 1973). Of these three extrinsic factors, water flow is the likely factor driving a shallow- and deep-bodied divergent shape generalization in fish based on the empirical findings of Scarnecchia (1988). Water flow is positively associated with swimming intensity because the rate of flow is proportional to the forces of resistance as the fish swims directly against the axis of flow (Vogel, 1981; Fung, 1990); if the fish were to change its position, then it must swim faster than the rate of flow and much energy or physical work may be wasted in generating profitless movements (Wu, 1971; Webb, 1975).

This dissertation follows the style and format of Physiological and Biochemical Zoology.

In addition, fishes must be capable of maintaining stability as they deviate from the axis of flow by actively resisting the shearing forces that are generated (Wu, 1971; Webb, 1975). Body shape, swimming speed, and swimming behavior are well-known intrinsic factors contributing to hydrodynamic resistance in fish (Lighthill, 1969; Wu, 1971; Newman, 1973; Chwang and Wu, 1974–1976; Webb, 1975; Pettersson and Hedenström, 2000). Because morphology is governed by natural selection, body shape adaptations in fish aim at reducing hydrodynamic resistance in the presence of water flow, thereby increasing swimming efficiency under an increasing water flow-rate regime (Vogel, 1981; Scarnechhia, 1988).

For shape diversification to ensue in this system, a fitness trade-off should occur among morphs specialized for different water flow-rate habitats—that is, in the presence of water flow, body shape adaptations to low swimming costs (i.e., high swimming efficiency) may decrease fitness to low maintenance costs (i.e., low standard metabolism); and, in the absence of water flow, body shape adaptations to low maintenance costs may decrease fitness to low swimming costs.

Pettersson and Brönmark (1999) have determined that deep-bodied fishes have a significantly lower maintenance cost than shallow-bodied individuals. According to Chwang and Wu (1974–1976) and Webb (1993), spheroidal morphs (e.g., deep-bodied fish) revolve more easily in water than moving through it; whereas, ellipsoidal morphs (e.g., shallow-bodied fish) move through water more easily than revolving in it. Thus, maneuverability increases as an object's shape becomes more spheroidal (deep-bodied); whereas, stability increases as an object's shape becomes more ellipsoidal (shallow-bodied). Taken together, these results suggest that deep-bodied fishes are best suited for high maneuverability but have high swimming costs; in contrast, shallow-bodied individuals are best suited for high stability but have high maintenance costs. Therefore, selection on hydrodynamic traits (i.e., selection for high maneuverability morphs or high stability morphs) should vary in variable water flow-rate habitats (Priede, 1985); and, swimming efficiency should be the basis of fitness differences among morphs (Plaut, 2001).

Aerobic swimming efficiency (swimming cost) is a fitness component (Plaut, 2001). Standard metabolism (maintenance cost), however, is a surrogate component of fitness; because metabolism is related to growth, which has positive fitness consequences in fish (Medgyesy, 1990; Metcalfe et al., 1995; Schluter, 1995). Aerobic swimming efficiency and standard metabolic rate are derived robustly from the novel work presented in chapters IV and V and analyzed extensively in chapter VI.

Organization

This dissertation is organized as five chapters (not including chapters I and VII), of which two are empirically designed (i.e., chapters III and VI) and the remaining three are methodological studies (i.e., chapters II, IV, and V) that are pertinent to the empirical analyses of chapters III and VI. The first methodological study (chapter II) is designed to introduce the reader to some of the mathematics and terminology of multivariate morphometrics, which is the statistical application to multivariate shape analysis. The first empirical study (chapter III) is designed to address an important question, which when answered will open discussion for the second empirical study (chapter VI). Why water flow, over other extrinsic factors, may act as a divergent selective factor underlying the principal axes of body shape diversification in bluegill? Subsequently, chapters IV – VI are designed to address the core of the dissertation, that is, to characterize and establish an ecophysiological framework for understanding the morphological evolution of bluegill sunfish.

Contextualization

In order to understand the contents of chapters II, III, and VI, an informative and concise delineation of the mathematical frameworks of spectral (eigen-) decomposition (ED), singular-value decomposition (SVD; two-step ED), and generalized Procrustes analysis (GPA; morphometric superimposition method) are needed. ED and SVD are fundamental to multivariate morphometrics and serve as the mathematical basis of principal components analysis (PCA), canonical variates analysis (CVA), partial least-squares analysis (PLS), and two important procedures in GPA: (1) ED of a symmetric

matrix is used to account for the appropriate degrees of freedom necessary for statistical analyses of shape variables computed in GPA and (2) SVD of an asymmetric matrix is used in the rotational fitting algorithm in GPA.

In this chapter, I focus on the calculation of partial Procrustes superimposed (aligned) coordinates, which are used throughout chapters II, III and VI for statistical study and visualization of shape variation in two dimensions. My intensions are not to overstate the mathematical complexity of GPA, or any other method presented here, but to convey to the reader that there exists a systematic, concise, and sound approach to calculating partial Procrustes aligned coordinates—a task that, until now, has not been characterized effectively in the literature due to the lack of practical guidance in methods, especially in regard to ED and SVD. Thus, my objective is to acknowledge some, but not all, of the mathematics that formulate the theory of GPA in a manner that does not undermine their elegance but rather accentuates their necessity and proliferation.

There are a few issues regarding terminology in multivariate statistics that I would like to clarify before getting into the heart of the material. Most of the technical terms that I use throughout this dissertation come from Legendre and Legendre (1998).

A matrix or a block is a rectangular array of elements arranged in horizontal rows (M) and vertical columns (N). Almost all of the multivariate analyses in this dissertation consist of evaluating the relationship between two blocks of data: a descriptor (dependent) matrix Y and a predictor (independent) matrix X:

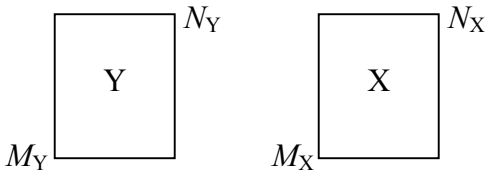

The columns of Y (N_Y) are referred to as descriptors, which are dependent variables. Descriptors are almost always continuous non-complex numbers that depend on X, that is, Y is a function of X, denoted $Y = f(X)$. The columns of X (N_X) are referred to as

predictors, which are independent variables. Predictors consist of mixed variables; they can be categorical (e.g., high, medium, low), discrete (e.g., binary), and continuous. The rows of Y (M_Y) and the rows of X (M_X) are shared conceptually and numerically, that is, $M_Y = M_X$. The rows of Y and X are referred to as objects or individuals. In particular, objects (M_X only) that consist of two or more categories within a predictor are called groups, which play an important role in PCA and especially CVA (chapter II).

A variance-covariance matrix is a special and very important (square) symmetric matrix that can be easily calculated by mean-centering any continuous non-complex data block, such as Y, and then performing the operation (matrix multiplication):

$$Y^TY = B_1 \tag{1.1}$$

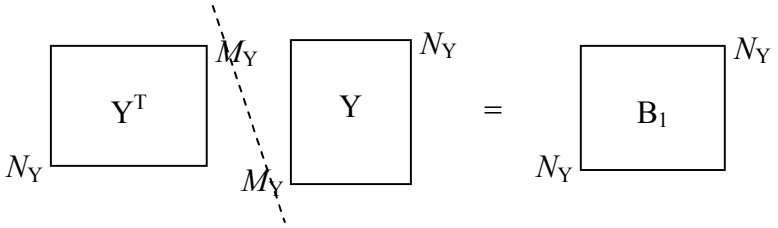

or

$$YY^T = B_2 \ , \tag{1.2}$$

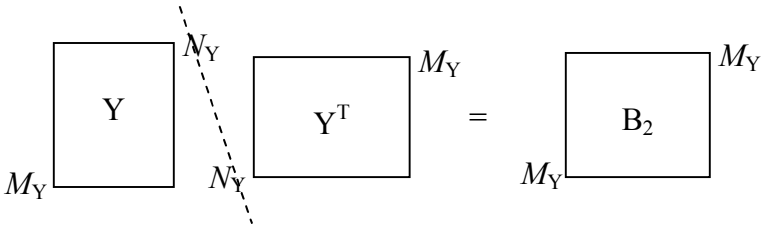

where B_1 is an N_Y x N_Y variance-covariance matrix describing variances and covariances of descriptors and B_2 is an M_Y x M_Y variance-covariance matrix describing variances and covariances of objects. Equations 1.1 and 1.2 are the most important operations in multivariate analyses. For instance, equations 1.1 and 1.2 are used together in PLS, and equation 1.1 is used in PCA and CVA.

Eigen- and singular-value decompositions

The most important structural property of a matrix is its symmetry. A square matrix is a special rectangular block, where the number of rows equals the number of columns (i.e., $M = N$). All symmetric matrices are square, but not all square matrices are symmetric. Also, all non-square ($M \neq N$) matrices are asymmetric. Matrix A is symmetric when it is equal to its transpose, that is, A^{T}. If $A \neq A^{T}$, then A is asymmetric. The distinction between square and non-square matrices is important because ED can only be performed on square matrices. In addition, the result of performing ED on a symmetric matrix is very different from the result of performing ED on a square asymmetric matrix. The difference, which is very important to note from a geometric perspective, is that ED of a symmetric matrix yields orthonormal (unit perpendicular) eigenvectors; whereas, ED of a square asymmetric matrix yields non-orthogonal (unit relative) eigenvectors. CVA, which is a popular ordination method closely related to PCA, involves ED of a square asymmetric matrix. CV axes are not orthogonal in the original data space from which they were derived (Zelditch et al., 2004). This complicates their interpretation and can lead to graphical and other visual distortions (chapter II). Canonical correlation analysis (CCoA), which is a popular partial ordination method closely related to PLS, also involves ED of square asymmetric matrices. CCo axes are very difficult to interpret for the same reasons as those from CVA. Therefore, it is vitally important to distinguish symmetric from square asymmetric matrices before performing ED.

Eigenvalues and eigenvectors are generally referred to as principal magnitudes and principal directions, respectively. The formal definition of eigenvalues and eigenvectors provides a concrete mathematical basis from which PCA, CVA, and many other multivariate methods are derived. The following definition of eigenvalue and eigenvector requires highlighting for future reference. If A is a square ($M = N$) matrix, then its characteristic equation is (Lancaster, 1969):

$$A\mathrm{u} = \lambda\mathrm{u} \ , \qquad (1.3)$$

where u is an eigenvector of order *M* x *1* and λ is an eigenvalue of order *1* x *1*. Rearranging equation 1.3 such that all terms appear on one side of the equation:

$$(A\mathrm{u} - \lambda\mathrm{u}) = 0 \tag{1.4}$$

then apply the distributive law to equation 1.4:

$$(A - \lambda\mathrm{I})\mathrm{u} = 0 \ , \tag{1.5}$$

where I is the identity (square) matrix (i.e., diagonal elements of 1s and off-diagonal elements of 0s) of the same order as *A*. Subtracting λ (a scalar) from *A* (a matrix) is not defined in matrix algebra. Thus, multiplying λ by I yields a diagonal matrix of λ. Then, subtracting a diagonal square matrix of λ from square matrix *A* (equation 1.5) is defined in matrix algebra.

The first step to calculating the total number (*M*-number) of eigenvalues (Λ) of *A* is to use the determinant (*det*). The *det* is an operator that acts only on a square matrix (= $A - \lambda\mathrm{I}$) and outputs a scalar multiple of Λ. Geometrically, the *det* is the area for a *2* x *2* matrix, volume for a *3* x *3* matrix, and hypervolume for a 4^+ x 4^+ matrix (Lancaster, 1969). Hence, the *det* is a scalar operator, which discounts u (Lancaster, 1969):

$$det(A - \lambda\mathrm{I}) = 0 \ , \tag{1.6}$$

where the *det* is defined by a characteristic polynomial function of order *M* with *M*-roots of λ, because it is a scalar multiple of Λ. Thus, the algebraic ("determinant") expansion of equation 1.6 is:

$$\rho_0\lambda^M - \rho_1\lambda^{(M-1)} - \rho_2\lambda^{(M-2)} - \ldots - \rho_M = 0 \ , \tag{1.7}$$

where ρ_M are the characteristic polynomial coefficients that can be calculated using the following equation (Lancaster, 1969):

$$\rho_N = tr(A_1[A_{(N\text{-}1)} - \rho_{(N\text{-}1)}\mathrm{I}])/N \qquad (N = 2, 3, 4 \ldots M) \ , \tag{1.8}$$

where $\rho_0 = 1$, $\rho_1 = tr(A_1)$, and A_1 is the original matrix A. The trace (tr) is the scalar sum of the diagonal elements of a square matrix. Mathematically, the tr is equal to the total variation of a symmetric matrix (i.e., the sum of the diagonal elements of A).

Once the ρ-coefficients in equation 1.7 are determined using equation 1.8, the next step is to determine the roots (λ; eigenvalues) of equation 1.7. So, if A is a *3* x *3* matrix, for example, then its 3rd order characteristic polynomial yields 3 total roots of λ (= Λ). Then, determining the eigenvalues of A is the second to last step in ED. The last step in ED is to calculate M-number of eigenvectors (U) of order M x M that correspond to their M-number of eigenvalues (Λ). The algebra to compute u_i corresponding to each λ_i is simple—rearrange equation 1.5 such that u_i is isolated on one side of the equation:

$$(A - \lambda_i I)^{-1}\delta = u_i \quad , \tag{1.9}$$

where δ is approximately equal to the null vector of order M x *1*. The null vector (Ω) is a vector consisting of elements equal to absolute zeros. It is meaningless to postmultiply the inverse of $(A - \lambda_i I)$ by Ω because the resultant is simply Ω. Therefore, δ is approximately equal to Ω (e.g., $1x10^{-16}$), which satisfies equation 1.9. Thus, the eigenvector (u_i) consists of elements that are very small values but can be scaled to appear more preferable to the eye. Usually, the scaling factor is the largest element of u_i. So, scaling all elements of u_i by the largest element will result in the newly scaled largest element equal to 1; all other elements of u_i have to be between 0 and ±1, because they are relative to the largest element (=1). Hence, elements of eigenvectors can be scaled relative to each other without affecting the directions of variance (Lancaster, 1969).

SVD is a generalization of ED in that it is a two-step ED. Unlike ED, SVD can be performed on any rectangular (square or non-square) matrix. If A is non-square (i.e., $M \neq N$), then A must be transformed into two square matrices before performing ED (i.e., a two-step ED). Let A be an M x N matrix, where $M \neq N$, then (Phatak and De Jong, 1997):

$$AA^{T} = V\Lambda_M V^{T} \tag{1.10}$$

and

$$A^{T}A = U\Lambda_{N}U^{T} \quad , \tag{1.11}$$

where V is an M x M matrix of orthonormal (i.e., $V^{T}V = I$) left singular vectors, U is an N x N matrix of orthonormal (i.e., $U^{T}U = I$) right singular vectors, Λ_{M} is an M x M diagonal matrix of squared singular values, Λ_{n} is an N x N diagonal matrix of squared singular values, and $\Lambda_{M} = \Lambda_{N}$.

Clearly, the resultant matrix of equations 1.10 and 1.11 (i.e., AA^{T} and $A^{T}A$) are not only square but also symmetric (see equations 1.1 and 1.2). Combining equations 1.10 and 1.11, SVD of A is (Phatak and De Jong, 1997):

$$A = V\Lambda_{n}^{\frac{1}{2}}U^{T} = V\Sigma U^{T} \tag{1.12}$$

If A is symmetric, that is, $A = A^{T}$, then V = U and $\Lambda = \Sigma^{2}$ because:

$$AA^{T} = (U\Sigma U^{T})(U\Sigma U^{T}) = U\Sigma^{2}U^{T} \quad , \tag{1.13}$$

where $(AA^{T})U = U\Lambda$, and:

$$A^{T}A = (U\Sigma U^{T})(U\Sigma U^{T}) = U\Sigma^{2}U^{T} \, , \tag{1.14}$$

where $(A^{T}A)U = U\Lambda$. Therefore, SVD becomes ED only for symmetric matrices, where V = U (i.e., orthonormal eigenvectors) and $\Lambda = \Sigma^{2}$ (i.e., eigenvalues). If A is asymmetric, that is, $A \neq A^{T}$ for square (i.e., $M = N$) or non-square (i.e., $M \neq N$) matrices, then U ≠ V (i.e., left and right singular vectors and $\Lambda = \Sigma$ (i.e., singular values).

It is important to note that if A is a square asymmetric matrix, then SVD of A is not equivalent to ED of A. SVD of any asymmetric matrix yields orthonormal left and right singular vectors and singular values; whereas, ED of a square asymmetric matrix yields non-orthogonal eigenvectors and relative eigenvalues. The two decompositions (i.e., ED and SVD) yield different results for square asymmetric matrices. SVD will always decompose a matrix into three constitutive products that equate to the matrix being decomposed, and the same is true for ED of symmetric matrices. However, ED will not decompose a square asymmetric matrix into its constitutive products because

they represent relative constituents. Therefore, the notation that is given to ED of a square asymmetric matrix *A* is:

$$A \Rightarrow \mathrm{QK} \quad , \tag{1.15}$$

where Q represents a shear (not a rotation) matrix of non-orthogonal eigenvectors (i.e., $Q^{T}Q \neq I$) and K represents a vector of relative eigenvalues because there are two symmetric matrices Φ and Θ such that $\Phi^{-1}\Theta = A$. This is the reason CVA is a relative-type method—a method to describe variation among groups relative to variation within groups. On the other hand, the product of two symmetric matrices can never yield a symmetric matrix, which is the reason PCA is not a relative-type method—it can only describe variation among objects or among descriptors (see equations 1.1 and 1.2).

Generalized procrustes analysis

Shape is defined as, "all the geometric information remaining in an object after differences in location, scale, and rotational effects are removed" (Zelditch et al., 2004). Unweighted partial warps and uniform components are the traditional shape variables used in linear statistical models (e.g., MANCOVA); although, PCA of Procrustes aligned coordinates are also used and are equivalent to the former shape variables. It is important to note that weighted partial warps (a.k.a, relative warps) are not equivalent to PCA of Procrustes aligned coordinates.

Procrustes aligned coordinates are generated by an algorithm called generalized Procrustes analysis (GPA), or partial Procrustes superimposition (equation 1.16), which is the removal of translational, rotational, and scaling effects from the original two-dimensional coordinates of homologous landmark data. The model and notation used in the following progression of two-dimensional GPA are (Rohlf, 1990; Bookstein, 1996; Dryden and Mardia, 1998):

$$\mathrm{M}_{ij}^{c}(i) = \underbrace{\mathrm{j}^{-1}(i)}_{\mathrm{M}_{ij}^{b}(i)}\underbrace{[\mathrm{M}_{ij}(i) - \mathrm{T}_{ij}(i)]}_{\mathrm{M}_{ij}^{a}(i)}\mathrm{H}_{ij}(i)\,, \tag{1.16}$$

where $M_{ij}^{a}(i) = [M_{ij}(i) - T_{ij}(i)]$, $M_{ij}^{b}(i) = j^{-1}[M_{ij}(i) - T_{ij}(i)]$, and $M_{ij}^{c}(i)$ is the result of rotating, scaling, and translating $M_{ij}(i)$ by $H_{ij}(i)$, $j^{-1}(i)$, and $T_{ij}(i)$, respectively. $M_{ij}(i)$ is a (p x 2) matrix of original (figure space) coordinates of p landmark data in a configuration before the removal of rotational, scaling, and translational effects. $M_{ij}^{a}(i)$ is a (p x *2*) matrix of pre-form space coordinates of p landmark data in a configuration after only translating $M_{ij}(i)$. $M_{ij}^{b}(i)$ is a (p x *2*) matrix of pre-shape space coordinates of p landmark data in a configuration after translating and scaling $M_{ij}(i)$. $M_{ij}^{c}(i)$ is (p x *2*) matrix of Procrustes aligned (shape space) coordinates of p landmark data in a configuration after translating, scaling, and rotating $M_{ij}(i)$. Each specimen is denoted by the symbol, *i*. The following below is a detailed example illustrating equation 1.16, or GPA (i.e., two-dimensional multivariate shape analysis).

The first step in Procrustes superimposition is to digitize images with designated homologous landmarks in order to capture from it a particular shape of interest. Each landmark is delineated in two-dimensional space with two numerical coordinates, denoted as x and y. I begin with a two-dimensional array of x-y coordinates of p landmarks, $M_{ij}(i)$ for specimen *i*:

$$M_{ij}(i) = \begin{bmatrix} x_1(i) & y_1(i) \\ x_2(i) & y_2(i) \\ x_3(i) & y_3(i) \\ . & . \\ . & . \\ . & . \\ x_p(i) & y_p(i) \end{bmatrix} \quad \text{(p x } 2\text{) matrix} \qquad (1.17)$$

Example of equation 1.17:

$$M_{ij}(\mathbf{1}) = \begin{bmatrix} -2.0 & 0.5 \\ 2.0 & 0.5 \\ 2.0 & -1.5 \\ -2.0 & -1.5 \end{bmatrix} \quad M_{ij}(\mathbf{2}) = \begin{bmatrix} -2.121 & 0.000 \\ 0.000 & 2.121 \\ 2.121 & 0.707 \\ -0.707 & -2.121 \end{bmatrix} \quad M_{ij}(\mathbf{3}) = \begin{bmatrix} -1.25 & 0.25 \\ 1.75 & 0.25 \\ 1.25 & -2.25 \\ -1.75 & -2.25 \end{bmatrix}$$

Above, there are three specimens (i = 1, 2, and 3), all of which are quadrilaterals (four-sided figures). The four chosen landmarks (coordinates) correspond to the four corners of the quadrilaterals. Therefore, p is equal to 4. Hence, there are a total of three *4* x *2* matrices. A pictorial representation below (figure 1.1) is an extrapolation of the three images (specimens) that correspond to their landmarks, where specimen 1 is colored in blue, specimen 2 in green, and specimen 3 in red.

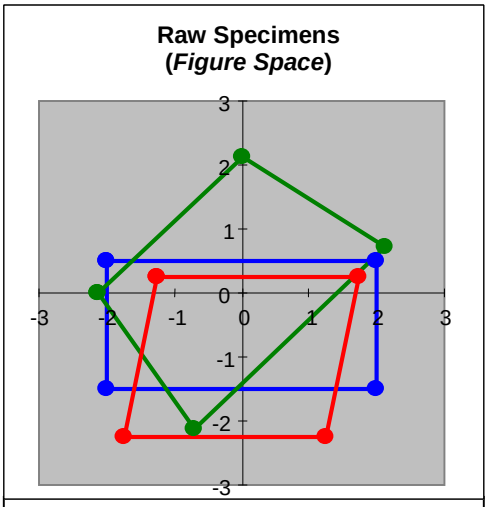

Figure 1.1. Three quadrilaterals in their original configuration.

The second step is to center all three specimens to the origin that has the coordinate structure of (0, 0). In order to accomplish such a task, it is necessary to calculate their centroid coordinates, $C_{1j}(i)$:

$$C_{1j}(i) = \begin{bmatrix} \dfrac{\sum_{k=1}^{p} M_{k1}(i)}{p} & \dfrac{\sum_{k=1}^{p} M_{k2}(i)}{p} \end{bmatrix} \quad (1 \text{ x } 2) \text{ vector} \qquad (1.18)$$

The first column of $C_{1j}(i)$ is simply the sum of all p x-components divided by the number of p landmarks and the second column follows the same operation as the first column but using the y-components instead. So basically, by postmultiplying (p x *1*) vector of ones 1_{p1} by equation 1.18 yields a (p x *2*) matrix $T_{ij}(i)$, which is the average of x and y coordinates:

Example of equation 1.18:

$$1_{p1}C_{1j}(\mathbf{1}) = T_{ij}(\mathbf{1}) = \begin{bmatrix} 0.0 & -0.5 \\ 0.0 & -0.5 \\ 0.0 & -0.5 \\ 0.0 & -0.5 \end{bmatrix} \qquad 1_{p1}C_{1j}(\mathbf{2}) = T_{ij}(\mathbf{2}) = \begin{bmatrix} -0.177 & 0.177 \\ -0.177 & 0.177 \\ -0.177 & 0.177 \\ -0.177 & 0.177 \end{bmatrix}$$

$$1_{p1}C_{1j}(\mathbf{3}) = T_{ij}(\mathbf{3}) = \begin{bmatrix} 0.0 & -1.0 \\ 0.0 & -1.0 \\ 0.0 & -1.0 \\ 0.0 & -1.0 \end{bmatrix}$$

To center specimen *i* to the origin, simply subtract $T_{ij}(i)$ from $M_{ij}(i)$. This calculation will result in a new array of x-y coordinates for specimen *i* (figure 1.2). This mathematical (geometrical) operation (equation 1.19) is commonly called translation, $M_{ij}^{a}(i)$ of specimen *i*, which centers each specimen to the origin at (0, 0):

$$M^{a}_{ij}(i) = \begin{bmatrix} M_{11}(i) - T_{11}(i) & M_{12}(i) - T_{12}(i) \\ M_{21}(i) - T_{21}(i) & M_{22}(i) - T_{22}(i) \\ M_{31}(i) - T_{31}(i) & M_{32}(i) - T_{32}(i) \\ . & . \\ . & . \\ . & . \\ M_{p1}(i) - T_{p1}(i) & M_{p2}(i) - T_{p2}(i) \end{bmatrix} \quad (p \text{ x } 2) \text{ matrix} \qquad (1.19)$$

Example of equation 1.19:

$$M^{a}_{ij}(\mathbf{1}) = \begin{bmatrix} -2.0 & 1.0 \\ 2.0 & 1.0 \\ 2.0 & -1.0 \\ -2.0 & -1.0 \end{bmatrix} \quad M^{a}_{ij}(\mathbf{2}) = \begin{bmatrix} -1.945 & -0.177 \\ 0.177 & 1.945 \\ 2.298 & 0.530 \\ -0.530 & -2.298 \end{bmatrix} \quad M^{a}_{ij}(\mathbf{3}) = \begin{bmatrix} -1.25 & 1.25 \\ 1.75 & 1.25 \\ 1.25 & -1.25 \\ -1.75 & -1.25 \end{bmatrix}$$

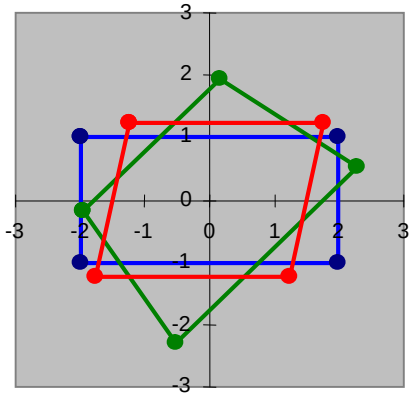

Figure 1.2. Three quadrilaterals translated to center on origin.

Because shape analysis is strictly concerned with shape variance and covariance, the size of specimen *i* should be excluded from the analysis. Therefore, size is normalized (or scaled) for each specimen in order to correct for it in the analysis (figure 1.3). Centroid size, j(*i*) is a scalar that accounts for the gross geometrical interpretation of size for

specimen *i*. Equation 1.20 is Pythagoras' theorem, which is the sum of the magnitude of p vectors of specimen *i* that has a two-dimensional coordinate structure of (M_{p1}, M_{p1}) and (C_{11}, C_{12}):

$$j(i) = \sqrt{\sum_{k=1}^{p}[M_{k1}(i) - C_{11}(i)]^2 + \sum_{k=1}^{p}[M_{k2}(i) - C_{12}(i)]^2} \quad \text{(scalar)} \qquad (1.20)$$

Example of equation 20:

$j(\mathbf{1}) = 4.472$ $\qquad$ $j(\mathbf{2}) = 4.330$ $\qquad$ $j(\mathbf{3}) = 3.937$

Therefore, to compute the scaled x-y coordinates from the translated coordinates, simply divide the x-y coordinates by j(*i*) (figure 1.3). Hence, the new array of scaled and translated $M^{b}_{ij}(i)$ coordinates for specimen *i* is:

$$M^{b}_{ij}(i) = \begin{bmatrix} \frac{M^{a}_{11}(i)}{j(i)} & \frac{M^{a}_{12}(i)}{j(i)} \\ \frac{M^{a}_{21}(i)}{j(i)} & \frac{M^{a}_{22}(i)}{j(i)} \\ \frac{M^{a}_{31}(i)}{j(i)} & \frac{M^{a}_{32}(i)}{j(i)} \\ . & . \\ . & . \\ . & . \\ \frac{M^{a}_{p1}(i)}{j(i)} & \frac{M^{a}_{p2}(i)}{j(i)} \end{bmatrix} \quad \text{(p x } \textit{2}\text{) matrix} \qquad (1.21)$$

Example of equation 1.21:

$$M_{ij}^{b}(1) = \begin{bmatrix} -0.447 & 0.224 \\ 0.447 & 0.224 \\ 0.447 & -0.224 \\ -0.447 & -0.224 \end{bmatrix} \quad M_{ij}^{b}(2) = \begin{bmatrix} -0.449 & -0.041 \\ 0.041 & 0.449 \\ 0.531 & 0.122 \\ -0.122 & -0.531 \end{bmatrix}$$

$$M_{ij}^{b}(3) = \begin{bmatrix} -0.318 & 0.318 \\ 0.445 & 0.318 \\ 0.318 & -0.318 \\ -0.445 & -0.318 \end{bmatrix}$$

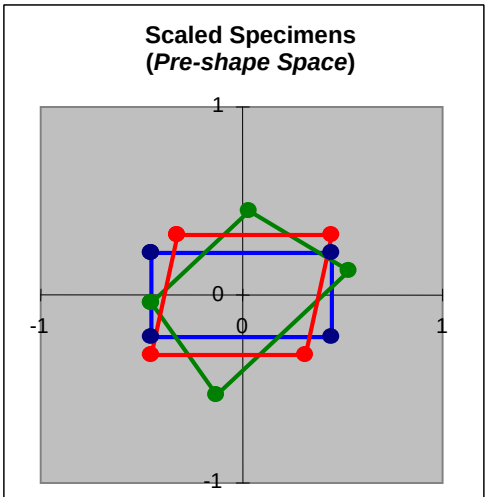

Figure 1.3. Three quadrilaterals translated and scaled to unit j(i).

The last and perhaps the most computationally intensive step involves rotating the three specimens to minimize the partial Procrustes distance (d; equation 1.22), which is the Euclidean distance between two landmark configurations when both specimens are translated, scaled, and rotated (Zelditch et al., 2004):

$$d(i_1, i_2) = \sqrt{\sum_{i,j}^{2,p} [E_{ij}(i_1, i_2)]^2} \quad , \qquad (1.22)$$

where E_{ij} is the (p x *2*) shape-difference matrix between two specimens, i_1 and i_2:

$$E_{ij}(i_1, i_2) = \begin{bmatrix} \Delta x_1(i_1, i_2) & \Delta y_1(i_1, i_2) \\ \Delta x_2(i_1, i_2) & \Delta y_2(i_1, i_2) \\ \Delta x_3(i_1, i_2) & \Delta y_3(i_1, i_2) \\ . & . \\ . & . \\ . & . \\ \Delta x_p(i_1, i_2) & \Delta y_p(i_1, i_2) \end{bmatrix} \quad (p \times 2) \text{ matrix} \qquad (1.23)$$

Because all three specimens are in pre-shape space (i.e., translated and scaled coordinates), the next step in GPA is to rotate all specimens to the first specimen—that is, $M_{ij}^{b}(2)$ and $M_{ij}^{b}(3)$ to $M_{ij}^{b}(1)$. The way that this is done is by postmultiplying $[M_{ij}^{b}(2)]^{T}$ by $M_{ij}^{b}(1)$ and $[M_{ij}^{b}(3)]^{T}$ by $M_{ij}^{b}(1)$, and then performing SVD (equations 1.10 – 1.12) on their results, which yields two *2* x *2* joint matrices. SVD is used to extract the necessary geometric information to rotate $M_{ij}^{b}(2)$ to $M_{ij}^{b}(1)$ and $M_{ij}^{b}(3)$ to $M_{ij}^{b}(1)$. A joint matrix (e.g., *A*) is the product of two distinct matrices and therefore is always asymmetric (i.e., $A \neq A^{T}$). SVD simply performs a two-step ED of *A* (see equations 1.10 – 1.12).

In the present case, the pre-shape coordinates of specimens 2 and 3 are rotated to the pre-shape coordinates of specimen 1. Hence, both *M* and *N* are equal to 2. Thus, the first rotation matrix, $Q_{ij}(i)$ needed to rotate specimens 2 and 3 to specimen 1 in order to minimize the distance between their corresponding landmarks is:

$$V(i)S_{ij}(i)U^{T}(i) = Q_{ij}(i) \qquad (2 \times 2) \text{ matrix} \qquad (1.24)$$

where matrix $S_{ij}(i)$ is an identity matrix of the form:

$$S_{ij}(i) = \begin{bmatrix} \pm 1 & 0 \\ 0 & \pm 1 \end{bmatrix}, \text{ where } (i = j) = \pm 1 \text{ and } (i \neq j) = 0\,, \qquad (1.25)$$

and the sign of equation 1.25 corresponds to the sign of the diagonal components of $\Sigma(i)$ (equation 1.12).

Example of equation 1.24:

$$Q_{ij}(\mathbf{1}) = \begin{bmatrix} 1 & 0 \\ 0 & 1 \end{bmatrix} \quad Q_{ij}(\mathbf{2}) = \begin{bmatrix} 0.707 & -0.707 \\ 0.707 & 0.707 \end{bmatrix} \quad Q_{ij}(\mathbf{3}) = \begin{bmatrix} 0.998 & 0.059 \\ -0.059 & 0.998 \end{bmatrix}$$

Then, rotate specimen *i* by postmultiplying $M_{ij}^{b}(i)$ by $Q_{ij}(i)$. Clearly, rotating the first specimen onto itself yields the identity matrix, I. After the first rotation, $Q_{ij}(i)$ is performed, a second one, $H_{ij}(i)$ should follow using the same mathematical steps mentioned above but with a slight change in notation (see equation 1.26). However in this following step, all specimens (including the first one) are rotated to the consensus, R_{ij} which is simply the average of each x and y component from 3 specimens (figure 1.4).

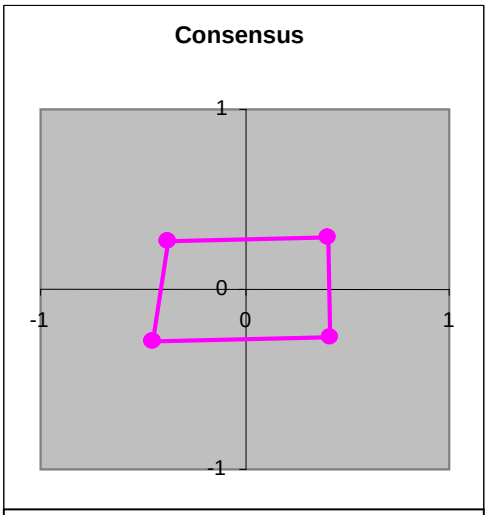

Figure 1.4. Reference configuration

Thus, the second rotation matrix, $H_{ij}(i)$ needed to rotate specimens 1, 2, and 3 to the consensus in order to minimize the distance between their corresponding landmarks is:

$$V(i)S_{ij}(i)U^{T}(i) = H_{ij}(i) \qquad (2 \text{ x } 2) \text{ matrix} \qquad (1.26)$$

Below is the final array of x-y coordinates, or Procrustes aligned coordinates for specimen *i* (see figure 1.5):

$$M_{ij}^{c}(1)=\begin{bmatrix}-0.431 & 0.253\\ 0.461 & 0.193\\ 0.431 & -0.253\\ -0.461 & -0.193\end{bmatrix}\quad M_{ij}^{c}(2)=\begin{bmatrix}-0.326 & 0.312\\ 0.365 & 0.264\\ 0.441 & -0.320\\ -0.481 & -0.256\end{bmatrix}$$

$$M_{ij}^{c}(3)=\begin{bmatrix}-0.316 & 0.319\\ 0.446 & 0.316\\ 0.316 & -0.319\\ -0.446 & -0.316\end{bmatrix}$$

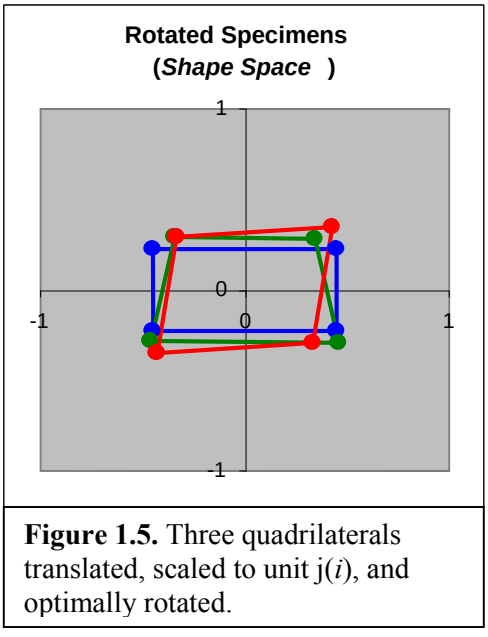

Figure 1.5. Three quadrilaterals translated, scaled to unit j(*i*), and optimally rotated.

Next, rearrange the coordinates of the three specimens in shape space so that they take the following form:

$M_{ij}^{c} \equiv$

specimen *i*	x1	y1	x2	y2	x3	y3	x4	y4
1	-0.431	0.253	0.461	0.193	0.431	-0.253	-0.461	-0.193
2	-0.326	0.312	0.365	0.264	0.441	-0.320	-0.481	-0.256
3	-0.316	0.319	0.446	0.316	0.316	-0.319	-0.446	-0.316

In this form, PCA of M_{ij}^{c} is performed in order to account for all nonzero axes of variance in M_{ij}^{c}. Usually, the number of statistically appropriate shape variables equals 2p - 4. However, PCA of M_{ij}^{c} yields 3 instead of the usual 4 (= 2*4 - 4) nonzero axes of variance because of the small number of specimens and the simplicity of the shapes:

$Y \equiv$

specimen *i*	shape variable 1	shape variable 2	shape variable 3
1	-0.989617181	-0.135932804	-0.035497903
2	-0.996325032	0.015327469	0.086142281
3	-0.991821139	0.120233679	-0.051114420

Block Y is in perfect form for linear statistical analyses. It should be noted that Y no longer represents coordinates like M_{ij}^{c}; rather, Y represents a geometrically orthogonal shape space containing all the information of *purely* shape extracted from the original coordinates of M_{ij}. This foundation should provide the necessary background for understanding the shape analyses presented in the following chapters.

CHAPTER II
DISTORTED REALITY: VISUALIZATION PROBLEMS AND SOLUTIONS IN MULTIVARIATE MORPHOMETRICS

> *For many parts of nature can neither be invented with sufficient subtlety, nor demonstrated with sufficient perspicuity, nor accommodated unto use with sufficient dexterity without the aid and intervention of mathematics*.
>
> — Francis Bacon (1561–1626)

Introduction

Shape variation between species, or between groups or along a gradient within species is can be readily evaluated using multivariate analysis of covariance (MANCOVA). However, visualizing the shape variance associated with an effect (independent variable) of interest can be complicated. Shape variation is, by nature, multidimensional and can only be analyzed using many variables simultaneously. The multivariable nature of shape variation necessitates a multivariate statistical analysis. Hence, visualizing shape variation requires a proper understanding of the relationship between multivariate shape and statistical analyses.

Multivariate analyses are common in ecology and evolutionary biology due to the nature of data in these fields. However, researchers do not always use ordination methods correctly. For instance, canonical variates analysis (CVA) is frequently used by ecologists and evolutionary biologists because it accounts for variance along axes by which groups are best discriminated, which from a taxonomic aspect can be very useful (Campbell and Atchley, 1981). Unfortunately, the benefits of CVA can sometimes over-shadow its drawbacks, in which case it may unknowingly do more damage than benefit and should not be used. The problem is that CV scores are scaled differently from the original scores from which they were derived (Zelditch et al., 2004). This scaling can be considered a distortion of the original data space because distances in CV space can be very different from distances in the original data space. Another problem with CV scores

that is less familiar and frequently overlooked is that they shear the original data space when they are used as independent variables in regression. In other words, the geometric orthogonality of multivariate shape space is lost when regression is performed using CV scores as independent variables. This procedure produces counterintuitive visual results.

Despite the visualization problems associated with CVA, the statistics for analyzing shape are relatively uncomplicated and serve as a basis for the visualization. There are several statistical and ordination methods in morphometrics that can be used to test hypotheses or to describe the diversity of shape variation from biological and/or ecological effects. Below I discuss two ordination methods that are common in multivariate morphometrics: CVA and principal components analysis (PCA). My objectives are to make clear the utility of each method, to make the concepts involved more accessible to those who have had difficulty understanding the mathematics of multivariate morphometrics, and to discuss visualization problems attributable to CV scores.

Ordination methods

CVA and PCA are used to simplify descriptions of shape variation from complex effects such as multidimensional interactions and nested terms (Zelditch et al., 2004). The purpose of PCA is to account for shape variation among individuals (Zelditch et al., 2004). The purpose of CVA is to account for shape variation among groups relative to variation within groups (Campbell and Atchley, 1981). In order to understand the differences and similarities between PCA and CVA, a mathematical description of the two methods is necessary. Let a *55* x *20* mean-centered data block X contain two groups A and B that act as one predictor (i.e., one independent variable):

$$X = \begin{array}{c} \overset{20}{\overbrace{}} \\ \left[\begin{array}{c} A \\ \hdashline B \end{array}\right] \\ 55 \end{array} \begin{array}{l} \\ 25 \\ 30 \end{array} , \qquad (2.1)$$

where group A is a *25* x *20* matrix and group B is a *30* x *20* matrix. The first step in PCA is to transform X into variance-covariance matrix Y:

$$X^T X = Y \quad , \tag{2.2}$$

where Y is a *20* x *20* symmetric matrix. Then, eigendecomposition (ED) is performed on equation 2.2 yielding an orthonormal set of eigenvectors (U; directions of variance) and corresponding set of eigenvalues (Λ; variances):

$$Y = U\Lambda U^T \quad , \tag{2.3}$$

where U is a *20* x *20* rotation matrix such that $U^TU = I$ (= identity) and Λ is a *20* x *20* diagonal matrix of eigenvalues. Ordinary PC scores (X_o) can be calculated from the following equation:

$$X_o = XU^T \quad , \tag{2.4}$$

where X_o is a *55* x *20* orthogonal set of PC scores. Depending on the magnitude of the eigenvalues, there might be only one PC axis of variation such that all eigenvalues are equal to zero except for the first one. In this case, only one PC axis (*55* x *1*) from the first eigenvector accounts for all the variation in X.

Equations 2.1 – 2.4 describe PCA of X among individuals. CVA can be described similarly but taking into account variation between groups A and B:

$$W = \begin{bmatrix} \overline{X}_A \\ \overline{X}_B \end{bmatrix} \quad , \tag{2.5}$$

where W is a *2* x *20* aggregated (stacked) group matrix, $\overline{X}_A$ is a *1* x *20* vector of object (individual) averages across 20 descriptors for group A, and $\overline{X}_B$ is a *1* x *20* vector of individual averages across 20 descriptors for group B. Variances and covariances between groups can then be calculated by transforming equation 2.5 into variance-covariance matrix H:

$$W^{T}W = H \ , \tag{2.6}$$

where H is *20* x *20* symmetric matrix. It should be noted that if the preferred analysis is to account for variation between groups, then simply perform PCA on the group means, or substitute equation 2.6 for equation 2.2 and then apply equations 2.3 and 2.4. This procedure specifically describes PCA of X between groups, not among individuals. The results of PCA of X between groups may not be equivalent to the results of PCA of X among individuals. In other words, the directions of variance in which group means are most different are not necessarily equivalent to the directions of variance in which individuals are most different (Zelditch et al., 2004). Subsequently, the within-group (error) variance-covariance matrix (E) can be calculated by subtracting equation 2.6 from equation 2.2:

$$E = (Y - H) \ , \tag{2.7}$$

where E is a *20* x *20* symmetric matrix. Because CVA accounts for variation among groups (H) relative to variation within groups (E), the following operation standardizes among-groups by within-groups scores:

$$T = E^{-1}H \ , \tag{2.8}$$

where T is a *20* x *20* asymmetric among-group relative to within-group square matrix. CV scores are then calculated by the same procedure described in equations 2.3 and 2.4:

$$T \Rightarrow QK \, , \tag{2.9}$$

where Q is a *20* x *20* shear matrix consisting of non-orthogonal eigenvectors (i.e., $Q^{T}Q \neq I$) and K is a *20* x *1* vector of relative eigenvalues. Then, CV scores (G) can be calculated from the following equation:

$$G = XQ^{T} \ , \tag{2.10}$$

where G is a *55* x *20* set of CV scores. Again, depending on the magnitude of the relative eigenvalues, there might be only one CV axis of variation such that all relative eigenvalues are equal to zero except for the first one. In this case, only one CV axis (*55* x *1*) from the first eigenvector accounts for all the between-group variation (H) in X relative to within-group variation in E.

Equations 2.5 – 2.10 describe CVA of X. There are similarities between PCA and CVA. For instance, equations 2.2, 2.3, and 2.4 are analogous to equations 2.6, 2.9, and 2.10, respectively. The main differences arise from equations 2.7 and 2.8, where the within-group variance-covariance matrix (E) is calculated, inverted, and then pre-multiplied by the between-group variance-covariance matrix (H). This operation is analogous to division in scalar form. It is equivalent to standardizing by E, which implies that CV scores are dimensionless—that is, eigenvalues (variances) are relative. Also, the eigenvectors (Q) from equation 2.9 are very different from the eigenvectors (U) from equation 2.3; CVA of X rotates and shears X to the principal axes of variation; whereas, PCA of X only rotates X to the principal axes of variation. CV axes are therefore mathematically inappropriate as independent variables because they shear the dependent variables (i.e., shape space) in regression.

The correct results of CVA (e.g., the relationship between the first CV axis and second CV axis) yield perfectly circular plots (Campbell and Atchley, 1981). However, if the distribution of E is heteroscedastic, then the results of CVA will yield elliptical (distorted) plots, which entirely contradict the use and practicality of CVA. Because shape variation almost always is heteroscedastic, CVA is not a particularly reliable method to use in morphometrics (Bookstein, 1996). There are investigators who are aware of this problem and still continue to use CVA despite its shortcomings because they believe that a small degree of heteroscedasticity should not cause severe distortion. This study, however, demonstrates—and, it is the first to do so—that in CV space even a small degree of heteroscadesticity can cause severe distortion.

For simple analytical designs, effects can be easily visualized (via thin-plate spline) using existing shareware programs (e.g. F.J. Rohlf's tpsRegr). However,

analytical designs in ecology and evolutionary biology are typically complex; that is, they include multiple interactions and nested terms. Therefore, I describe two procedures from which one can derive accurate visualizations for complex effects of focal variables on organismal shape. The first procedure involves PCA of the predicted shape variables to produce independent variable surrogates (IVS) from any statistical model effect. The second procedure involves both PCA and Burnaby's (1966) method to remove shared variation between effects. By using a designed dataset, I have demonstrated that visualizations attributable to IVS and PC scores are not distorted and that visualizations attributable to CV scores are distorted.

PCA is not a substitute for CVA. PCA, unlike CVA, is a rigid rotation of multivariate space, which preserves the geometric orthogonality of shape variables (Zelditch et al., 2004). IVS are independent variables computed from PCA of the predicted dependent variables. The procedure for generating IVS is conceptually intuitive because the original independent variable used in multivariate regression to generate an array of predicted variables correlates perfectly with the surrogate that was computed from PCA of the predicted variables. For a simple effect such as centroid size, it is trivial and redundant to produce a surrogate because the effect is already in a proper numerical form. However, if there were an interaction between centroid size and some other effect of interest, then PCA can be used to generate IVS that can be easily visualized in tpsRegr without producing visual distortion. In addition, if the interaction term were multidimensional, then each IVS axis is orthogonal because PCA always yields orthonormal axes within an effect (i.e., $U^TU = I$). Hence, the multidimensional interaction term can be decomposed into orthogonal IVS. Similarly, nested terms, which are usually composed of multiple dimensions, can also be decomposed into orthogonal IVS.

IVS are not substitutes for PC or CV scores. IVS are simply dummy variables from PC scores of the predicted array of dependent variables from a single independent variable. Hence, IVS can be applied in two ways: (1) to replace a categorical independent variable with an equivalent numerical one and (2) to transform

multidimensional interactions and nested terms onto orthogonal axes. IVS are simple to calculate and they provide acceptable visualizations because they represent independent variables that are perfectly correlated with their regressed form. Also, the statistics associated with IVS are identical to that of their original independent variable form. The only limitation of IVS is that they do not describe variation like PC and CV scores. Thus, they cannot be used to generate or visualize PC and CV axes. IVS are simply an alternative and quick-and-easy form of dummy variables. "With a cleverly designed set of dummy variables [i.e., IVS] one can use tpsRegr to perform analyses as multivariate analysis of variance (MANOVA), multivariate analysis of covariance (MANCOVA), and other designs that correspond to multivariate linear models" (Rohlf, 2003, tpsRegr).

Burnaby's (*1966*) *method*

CVA is the conventional method used for generating shared and unique axes of shape diversification among groups (see Langerhans and DeWitt, 2004, for a description of concepts) and it continues to be used to construct many plots of this form. These CV axes are treated as independent variables and their effects on shape are then visualized from the thin-plate spline in tpsRegr. Many investigators are unaware of the problems associated with CVA—that it can and usually does produce misleading results and therefore should not be used to construct plots of any kind, especially when they involve visualizations of shape. This study addresses an alternative method for generating shared and unique axes of shape diversification among groups—that is, PCA and Burnaby's (1966) method are used together as a conceptually equivalent mathematical alternative for CVA.

Briefly, Burnaby's (1966) method can be used to project an array of predicted shape variables orthogonal to an array of shape variables that represent variation which is irrelevant to the preferred analysis. This method is equivalent to the multivariate technique, which involves computing an array of residual shape variables by subtracting an array of predicted shape variables from the array of original shape variables. Burnaby's method, however, allows for more control than its multivariate analog described above. A mathematical description of Burnaby's method is presented along

with its useful application for generating shared and unique axes of shape diversification among groups.

IVS cannot be used to generate shared and unique axes of shape diversification among groups because IVS only represent dummy variables. The variation along an IVS axis does not account for the shape variation described from this axis. The variation along PC and CV axes, however, does account for the shape variation described from these axes. Therefore, visualizations attributable to IVS can be different from the visualizations attributable to PC and CV scores. Basically, IVS are used in prediction (i.e., for predicting shape variation); whereas, PC and CV scores are used in description (i.e., for describing shape variation); and prediction is very different from description (see Zelditch et al., 2004, pp. 229–259).

Objectives

The objectives of this study are: (1) to illustrate a straightforward and intuitive procedure for IVS, (2) to expose the inherent problems of CVA, and (3) to revisit Burnaby's (1966) method and its useful application for generating shared and unique axes of shape diversification among groups.

Independent variable surrogates

The procedure for calculating IVS involves multivariate regression analysis to ascertain an *M* x *N* array of predicted shape variables from an independent variable X. Let *M* equal the number of individuals (rows); and let *N* equal the number of shape variables (columns). For simplicity, I will describe the procedure using 5 individuals and 2 shape variables. Let X be a *5* x *1* mean-centered independent variable vector; and let Y be a *5* x *2* shape (dependent) variable matrix:

$$\mathrm{X} = \begin{bmatrix} a \\ b \\ c \\ d \\ e \end{bmatrix} \qquad \mathrm{Y} = \begin{bmatrix} f & k \\ g & l \\ h & m \\ i & n \\ j & o \end{bmatrix} \quad , \tag{2.11}$$

where elements *a*–*e* are in numerical discrete or continuous form and elements *f*–*o* are in numerical continuous form. Then, join X and Y from equation 2.11 to construct an aggregated matrix J:

$$\mathrm{J} = \begin{bmatrix} a & f & k \\ b & g & l \\ c & h & m \\ d & i & n \\ e & j & o \end{bmatrix} \tag{2.12}$$

Next, compute the variance-covariance matrix (S) of equation 2.12:

$$\mathrm{S} = \left(\frac{\mathrm{J}^{\mathrm{T}}\mathrm{J}}{M-1} \right) = \begin{bmatrix} p & q & r \\ q & s & t \\ r & t & u \end{bmatrix}, \tag{2.13}$$

where *M* is equal to 5, *p* is equal to the variance of X, *q* and *r* represent the covariance between X and the two columns of Y, and *s*, *t*, and *u* represent the variance-covariance between the two columns of Y. Linear regression coefficients (R) can then be calculated for the two dependent variables, Y on X:

$$\mathrm{R} = [p]^{-1} \cdot [q \quad r] = \begin{bmatrix} v \\ w \end{bmatrix}^{\mathrm{T}}, \tag{2.14}$$

where *v* represents the regression coefficient for the first column of Y on X and *w* represents the regression coefficient for the second column of Y on X. Thus, the predicted Y ($\mathrm{Y_p}$; predicted shape variables) can be calculated by postmultiplying X by R:

$$\mathrm{Y_p}=\begin{bmatrix} a \\ b \\ c \\ d \\ e \end{bmatrix} \cdot \begin{bmatrix} v \\ w \end{bmatrix}^{\mathrm{T}} = \begin{bmatrix} av & aw \\ bv & bw \\ cv & cw \\ dv & dw \\ ev & ew \end{bmatrix} \tag{2.15}$$

Once a *5* x *2* matrix of predicted shape variables (equation 2.15) is obtained, PCA is then performed on $\mathrm{Y_p}$. The first step in PCA is decomposing the predicted variance-covariance matrix $\mathrm{H} = \mathrm{Y_p^T Y_p}$ into eigenvectors and eigenvalues. The result is a *2* x *2* matrix of orthonormal eigenvectors (U) and a corresponding diagonal set of eigenvalues (Λ) of the same order:

$$\mathrm{H} = \mathrm{Y_p^T Y_p} = \mathrm{U_p \Lambda_p U_p^T} = \begin{bmatrix} \alpha & \beta \\ -\beta & \alpha \end{bmatrix} \cdot \begin{bmatrix} \tau_1 & 0 \\ 0 & \tau_2 \end{bmatrix} \cdot \begin{bmatrix} \alpha & -\beta \\ \beta & \alpha \end{bmatrix}, \tag{2.16}$$

where $\mathrm{U_p^T U_p} = \mathrm{I}$. H is commonly referred to as a hypothesis matrix in MANOVA and a predicted variance-covariance matrix in multivariate regression—the former lexis being more statistical than the latter. Equation 2.16 shows mathematically that ED of a symmetric (variance-covariance) matrix always yields a rotation matrix U, which is orthonormal by property: $\alpha = \cos(\theta)$ and $\beta = \sin(\theta)$, where θ is the angle of rotation in radians. Thus, PCA is a rigid rotation of multivariate space. Depending on the number (*D*) of dimensions of variability of the independent variable, there could be an *N* x *D* array of eigenvectors whose eigenvalues are non-zero. For the case described above, the maximum *D* can be 2 and its minimum can be 1. Let $\tau_1 > 0$ and $\tau_2 = 0$ such that $D = 1$, then the second step in PCA is postmultiplying $\mathrm{Y_p}$ by the *2* x *1* array of U. The resultant will be a *5* x *1* vector of IVS ($= \mathrm{X_S}$), which are PC scores because the *2* x *2* array of eigenvectors represents linear combinations of the *5* x *2* array of predicted shape variables ($\mathrm{Y_p}$) from the original independent variable (X):

$$X_S = Y_p U_p^T = \begin{bmatrix} av & aw \\ bv & bw \\ cv & cw \\ dv & dw \\ ev & ew \end{bmatrix} \cdot \begin{bmatrix} \alpha \\ -\beta \end{bmatrix} = \begin{bmatrix} av\alpha - aw\beta \\ bv\alpha - bw\beta \\ cv\alpha - cw\beta \\ dv\alpha - dw\beta \\ ev\alpha - ew\beta \end{bmatrix} \quad (2.17)$$

X_S is correlated perfectly with X and therefore statistically equivalent to X, because the variation accounted for in equation 2.17 comes only from the elements of X—that is, elements $v\alpha$ and $w\beta$ are uniform throughout the vector so that they do not contribute to variation in X. Equations 2.15 – 2.17 describe IVS as surrogates for X—nothing more and nothing less. This is an elegant and quick-and-easy method for calculating dummy variables for many independent variables without the hassle of generating them by hand, especially when multidimensional interactions and nested terms are involved.

Because IVS are always numeric variables, they can be easily visualized by entering them in tpsRegr as independent variables. The program will perform a multivariate multiple regression analysis (i.e., regressing multiple shape variables on multiple IVS), which will extrapolate visualizations for each IVS axis. The visualizations attributable to IVS are due to predicting (not describing) the dependent variable using a hypothetical linear model of ordinary least-squares. These visualizations are predicted dependent variables along one linear axis (slope or gradient), and they do not describe gradients of variation across the dependent variables like PC and CV scores. This is a very important point because the visualizations attributable to IVS only represent visualizations based on the traditional linear regression model and consequently on the statistics (e.g., p-statistics). Thus, IVS are essential for providing the prediction and supporting the statistics. PC and CV scores are essential for providing the description (e.g., accounting for variation) and supporting the visualization (e.g., graphing). Then, correlating IVS to PC or CV scores represents correlative (not causative) explanation for the effect. If the visualizations attributable to IVS appear very similar to the visualizations attributable to PC or CV scores, then this is an indication of a strong correlative explanation for the effect.

Another operation can be evaluated from equation 2.17 that yields different results. Instead of postmultiplying Y_p by U_p^T, one can also postmultiply Y by U_p^T:

$$X_p = YU_p^T = \begin{bmatrix} f & k \\ g & l \\ h & m \\ i & n \\ j & o \end{bmatrix} \cdot \begin{bmatrix} \alpha \\ \beta \end{bmatrix} = \begin{bmatrix} f\alpha + k\beta \\ g\alpha + l\beta \\ h\alpha + m\beta \\ i\alpha + n\beta \\ j\alpha + o\beta \end{bmatrix}, \quad (2.18)$$

where X_p is a *5* x *1* vector of predicted PC scores of Y on X, not IVS. Equations 2.17 and 2.18 are mathematically very similar but yield very different results. Returning to equation 2.6, PCA of X using H instead of Y is analogous to equation 2.18 in that the results are predicted PC scores between groups, because groups A and B represent a categorical independent variable.

So far I have described two "flavors" of PCA: (1) ordinary PCA (equations 2.1 – 2.4) and (2) prediction PCA (equations 2.11 – 2.18). IVS are a special type of predicted PC scores—that is, postmultiplying the predicted dependent variables (Y_p) by the predicted eigenvectors (U_p^T), which is a rotation of Y_p back to X ($=X_S$). The predicted PC scores of Y on X, on the other hand, are the result of postmultiplying the original dependent variables (Y) by the predicted eigenvectors (U_p^T), which is a rotation of Y on X ($=X_p$).

Burnaby's (1966) method – revisited

Burnaby's (1966) method has many useful applications in morphometrics, one of which is to remove allometric (size) variation from shape, another of which is to orthogonalize eigenvectors among predicted variance-covariance matrices for different independent variables. The latter becomes important when generating accurate shared and unique axes of shape diversification among groups. It is important to note that eigenvectors from a variance-covariance (symmetric) matrix are always orthonormal but

not necessarily orthonormal among predicted variance-covariance matrices from different independent variables.

I will define the parameters of the method using different notations than presented by Burnaby (1966) to avoid conflict with notation presented in the current manuscript. Let P be any *M* x *Q* matrix that represents variation which is irrelevant to the preferred analysis (e.g., predicted shape variables for an undesired effect); let Γ be any *M* x *N* matrix to which P is projected orthogonal; and let ζ be the resultant *M* x *N* matrix that represents variation in Γ excluding all variation from P (i.e., ζ orthogonal to P):

$$(I - P(P^TP)^{-1}P^T)\Gamma = \zeta \ , \tag{2.19}$$

where I is a diagonal matrix of 1s of order *M* x *M*, which is commonly referred to as the identity matrix. Equation 2.19 is Burnaby's (1966) method for rendering matrices orthogonal with respect to other matrices (i.e., removing shared variation between effects).

In order to apply equation 2.19 effectively, to generate shared and unique axes of shape diversification among groups, a multivariate multiple regression analysis is required. Extending equations 2.11 – 2.16, let X be a *5* x *2* matrix, where the first column of X is independent variable 1 and the second column of X is independent variable 2. Then, two predictions (Y_{p1} and Y_{p2}) are the result of a multivariate multiple regression analysis:

$$H_1 = Y_{p1}^T Y_{p1} = U_{p1} \Lambda_{p1} U_{p1}^T \tag{2.20}$$

and

$$H_2 = Y_{p2}^T Y_{p2} = U_{p2} \Lambda_{p2} U_{p2}^T \ , \tag{2.21}$$

where U_{p1} and U_{p2} contain orthonormal sets of eigenvectors, but U_{p1} and U_{p2} may not be orthonormal with respect to each other; multiple regression only controls (not orthogonalizes) the effects of the independent variables on the dependent variable. In other words, controlling the effects of one independent variable on another optimally

partitions (not removes) shared variation from the dependent variable. Thus, orthogonality between effects (equations 2.20 and 2.21) must be artificially enforced:

$$H_{\zeta 1} = H_1 - H_2 = U_{\zeta 1} \Lambda_{\zeta 1} U_{\zeta 1}^T \tag{2.22}$$

and

$$H_{\zeta 2} = H_2 - H_1 = U_{\zeta 2} \Lambda_{\zeta 2} U_{\zeta 2}^T \quad , \tag{2.23}$$

where $U_{\zeta 1}$ corresponding to $\Lambda_{\zeta 1} \neq 0$ are orthogonal to $U_{\zeta 2}$ corresponding to $\Lambda_{\zeta 2} \neq 0$. Equation 2.19 cannot be applied directly to variance-covariance matrices because they will lose symmetry and no longer represent variance and covariance. Therefore, equations 2.22 and 2.23 are the result of squaring equation 2.19:

$$[I - Y_{p2}(Y_{p2}^T Y_{p2})^{-1} Y_{p2}^T] Y_{p1} = Y_{\zeta 1} \quad , \tag{2.24}$$

$$Y_{\zeta 1}^T Y_{\zeta 1} = H_1 - H_2 = H_{\zeta 1} \quad , \tag{2.25}$$

and

$$[I - Y_{p1}(Y_{p1}^T Y_{p1})^{-1} Y_{p1}^T] Y_{p2} = Y_{\zeta 2} \quad , \tag{2.26}$$

$$Y_{\zeta 2}^T Y_{\zeta 2} = H_2 - H_1 = H_{\zeta 2} \quad , \tag{2.27}$$

where $Y_{\zeta 1}$ represents variation in Y_{p1} excluding variation in Y_{p2} and $Y_{\zeta 2}$ represents variation in Y_{p2} excluding variation in Y_{p1}. Hence, equations 2.22 and 2.23 are the result of squaring $Y_{\zeta 1}$ (equation 2.25) and $Y_{\zeta 2}$ (equation 2.27), respectively. Finally, calculate Burnaby PC scores for independent variables 1 and 2:

$$X_{\zeta 1} = Y U_{\zeta 1}^T \tag{2.28}$$

and

$$X_{\zeta 2} = YU_{\zeta 2}^{T} \quad , \tag{2.29}$$

where $X_{\zeta 1}$ represents Burnaby PC scores describing variation from the effect of independent variable 1 excluding variation from the effect of independent variable 2, and $X_{\zeta 2}$ represents Burnaby PC scores describing variation from the effect of independent variable 2 excluding variation from the effect of independent variable 1. Hence, the shared variation between effects (i.e., Y_{p1} and Y_{p2}) has been removed. Evaluating the angle (θ) between eigenvectors of $U_{\zeta 1}$ corresponding to $\Lambda_{\zeta 1} \neq 0$ and eigenvectors of $U_{\zeta 2}$ corresponding to $\Lambda_{\zeta 2} \neq 0$ is used to check for orthogonality between effects (Finney and Thomas, 1994):

$$\theta = \cos^{-1} \left\| U_{\zeta 1} \cdot U_{\zeta 2} \right\| \quad , \tag{2.30}$$

where θ - 90^{o} is the degree of shared variance between Y_{p1} and Y_{p2}. The maximum degree of shared shape variance between any two eigenvectors is 90^{o}; whereas, the minimum degree of shared shape variance between any two eigenvectors is 0^{o}. Equation 2.30 is the arccosine of the cross-product between the meaningful eigenvectors of $U_{\zeta 1}$ and $U_{\zeta 2}$. Because eigenvectors are normalized to unit magnitude, there is no need to divide equation 2.30 by the product of the magnitudes of the eigenvectors of $U_{\zeta 1}$ and $U_{\zeta 2}$, which is the complete formula for calculating θ between any two vectors.

Like IVS, Burnaby PC scores are also a special type of predicted PC scores—that is, they are formulated equivalently using equation 2.18 except that the eigenvectors between effects are orthogonalized using equation 2.19. Thus, Burnaby PC scores account for *pure* variation, that is, the variation remaining after removing all variation shared between effects (e.g., Y_{p1} and Y_{p2}). These scores, like all PC scores, continue to

preserve geometric orthogonality of shape space because $U_{\zeta 1}^{T} U_{\zeta 1} = I$ and $U_{\zeta 2}^{T} U_{\zeta 2} = I$. Eigenvectors from CVA, on the other hand, cannot be orthogonalized because predicted variance-covariance matrices are standardized by error, that is, $E^{-1}H$ yields non-orthogonal (relative) eigenvectors ($Q^{T}Q \neq I$). Therefore, PCA is more flexible for solving visualization problems than CVA, because H always remains symmetric when addition or subtraction (equations 2.22, 2.23, 2.25, and 2.27) is used.

In summary, four PC scores have been characterized: ordinary PC scores (X_o), predicted PC scores (X_p), and two special types of predicted PC scores: IVS (X_S) and Burnaby PC scores (X_ζ). IVS are the only "PC scores" that do not describe variation because they are actually dummy variables.

Designed dataset

A design dataset of known shape deformations was generated in Microsoft Excel (figure 2.1). The design consisted of 3 predictors (i.e., stretch, shear, and trapezoid effects) and 3 groups within each predictor (i.e., negative, neutral, and positive gradients of deformation). Each effect was calculated from a reference (consensus) configuration with four landmarks of 2-dimensional variation (x-y coordinates). Each coordinate was formulated by 3 sets of conditions, each of which was assigned one of the 3 groups followed by a logical test that resulted in a stochastic variable ranging from 0 to ±1 (Excel *rand* function) for negative and positive groups and constant zero for the neutral group. The result from each set of conditions was then summed to the corresponding coordinates of the consensus configuration. This produced random (and yet small heteroscedastic) variation within groups. The *27* x *8* matrix of coordinates was transformed into a *27* x *4* matrix of shape variables using tpsRelw. The reason for this transformation is that shape variables, unlike the original shape coordinates, represent appropriate distance measures and have the same number of coordinates as degrees of freedom. Thus, shape variables can be used in any conventional (linear) statistical

analysis. MANCOVA was used as the statistical platform, where the dependent variables are the shape variables and the independent variables are the three predictors (i.e., stretch, shear, and trapezoid effects) categorized by 3 groups (i.e., negative, neutral, and positive gradients of deformation).

Because the categorical independent variables directly produced the effects, IVS were generated (equations 2.11 – 2.17) and then entered as dummy variables in tpsRegr in order to visualize them (figure 2.2). The visualizations attributable to IVS have to be accurate because these variables were designed to directly generate the effects (along with some random variation); this may not be true with real datasets. Subsequently, the visualizations for each effect attributable to IVS were compared to the visualizations for each effect attributable to predicted PC scores (figure 2.3; equations 2.11 – 2.18), CV scores (figure 2.4; equations 2.5 – 2.10), and Burnaby PC scores (figure 2.5; equations 2.19 – 2.29).

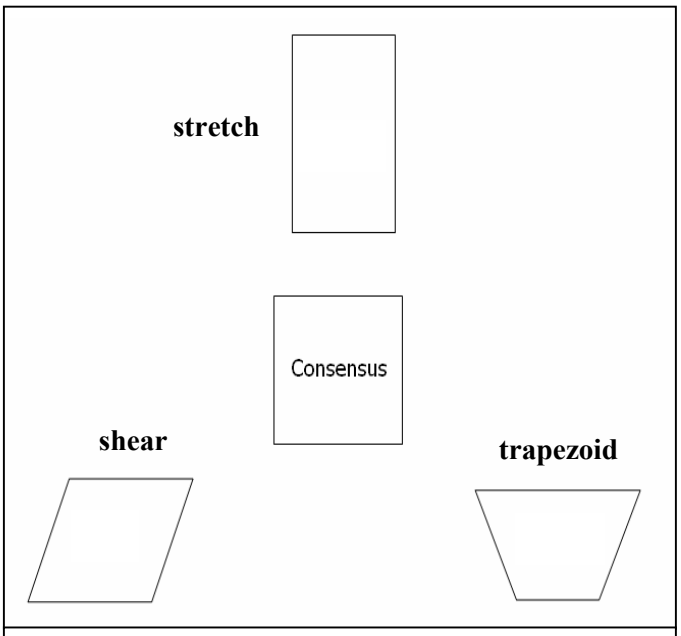

Figure 2.1. A design dataset of known shape deformations: stretch, shear, and trapezoid.

Results

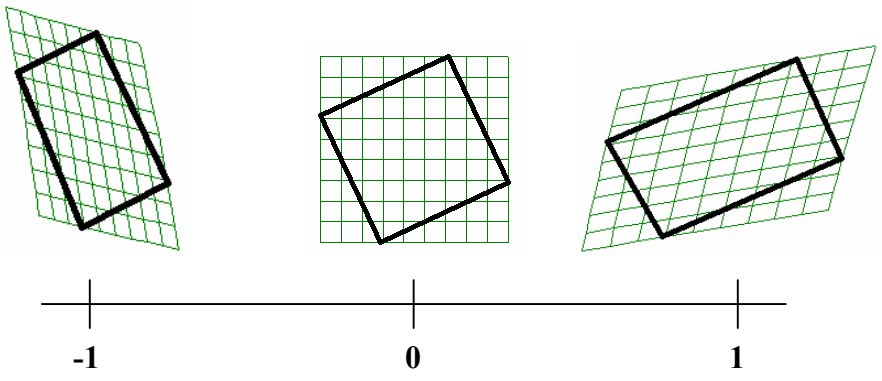

X_{S1} predicting the *stretch* effect

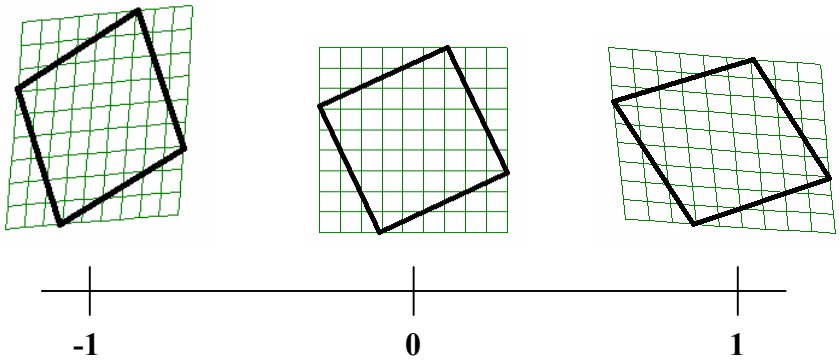

X_{S2} predicting the *shear* effect

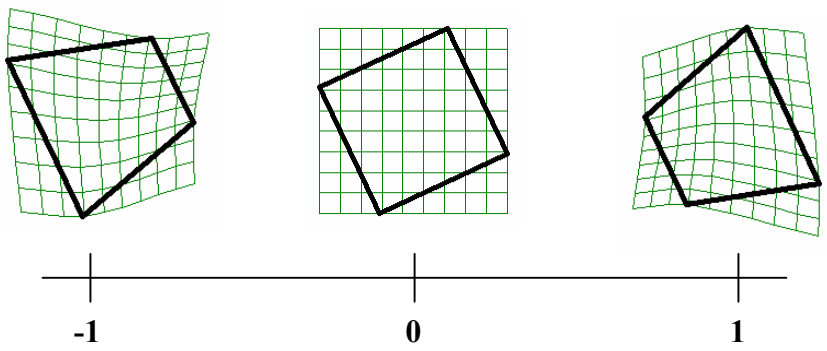

X_{S3} predicting the *trapezoid* effect

Figure 2.2. Thin-plate spline visualizations attributable to IVS predicting the three shape effects along negative (-1), neutral (0), and positive (1) gradients of deformation (tpsRegr).

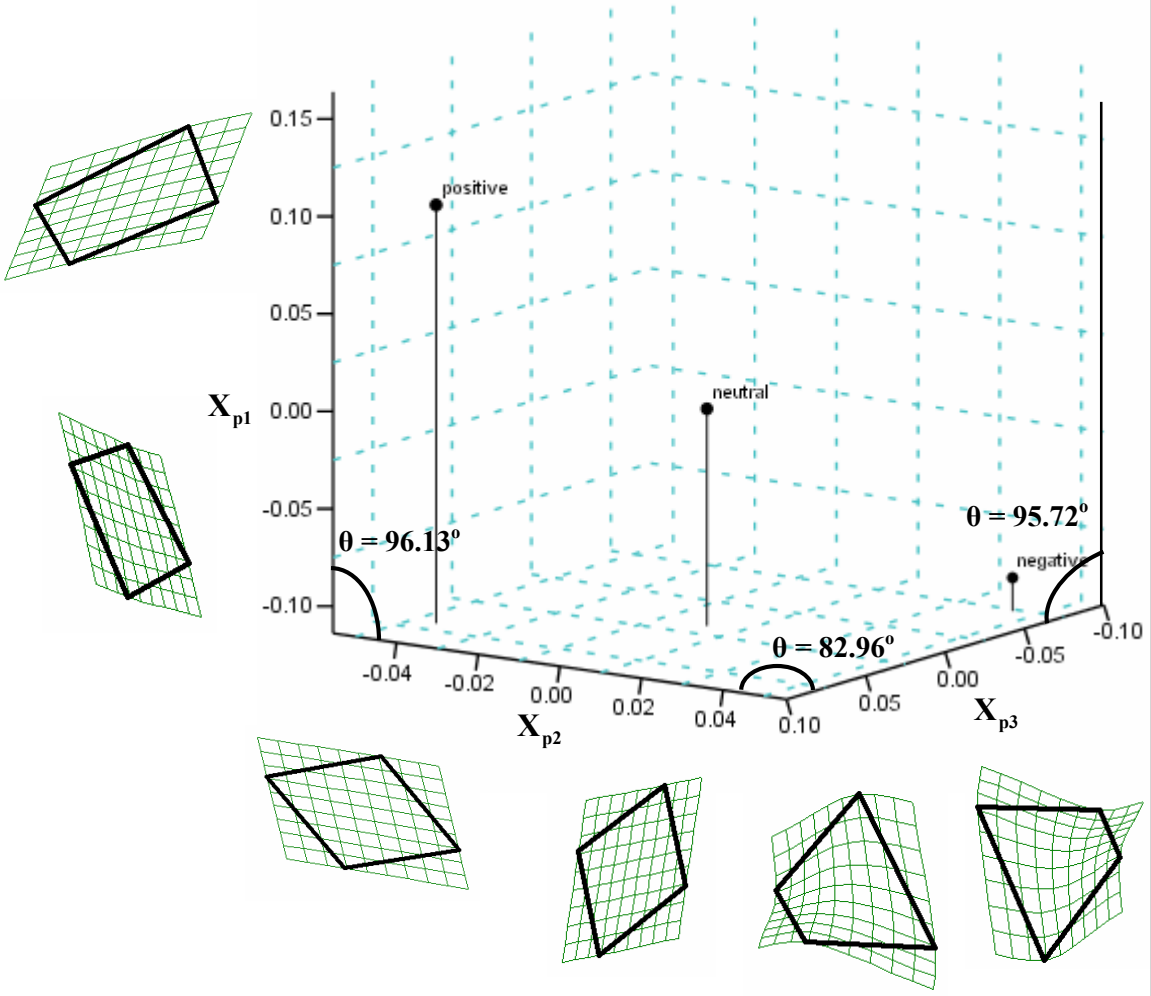

Figure 2.3. Thin-plate spline visualizations attributable to predicted PC scores describing the stretch effect (X_{p1}), the shear effect (X_{p2}), and the trapezoid effect (X_{p3}). X_{p1} accounted for 50.28% of total shape variance; X_{p2} accounted for 9.98% of total shape variance; and X_{p3} accounted for 24.11% of total shape variance. The degree of shared shape variance between X_{p1} and X_{p2} is -6.13° (=90° - 96.13°), between X_{p1} and X_{p3} is -5.72° (=90° - 95.72°), and between X_{p2} and X_{p3} is 7.04° (=90° - 82.96°). The correlation coefficient between X_{p1} and X_{S1} is 0.97, between X_{p2} and X_{S2} is -0.87, and between X_{p3} and X_{S3} is 0.86. The three data points describing the shape effects along negative, neutral, and positive gradients of deformation are averages (centroid values) of predicted PC scores. All visualizations have been magnified by 3x (tpsRegr).

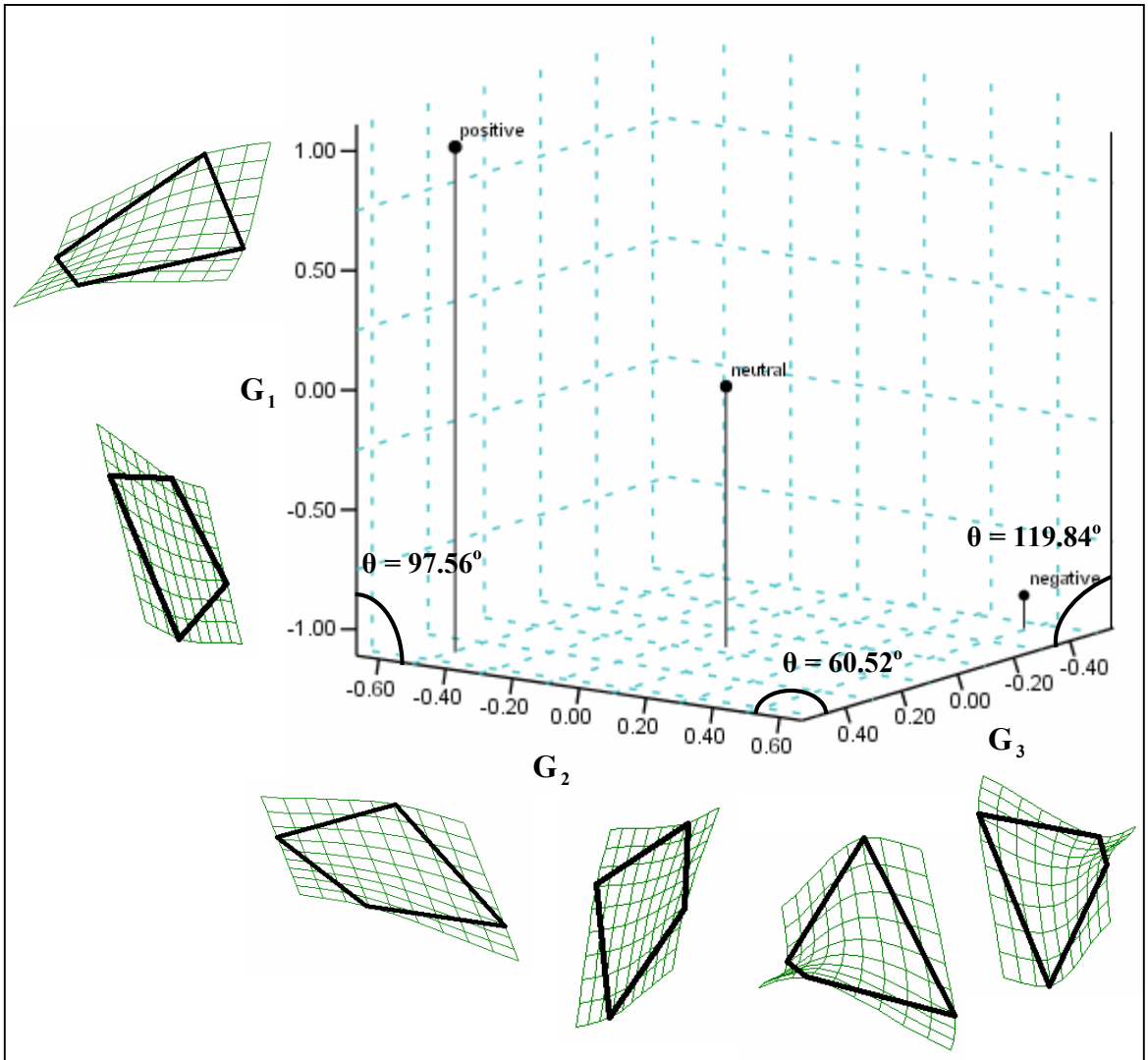

Figure 2.4. Thin-plate spline visualizations attributable to CV scores describing the stretch effect (G_1), the shear effect (G_2), and the trapezoid effect (G_3). G_1 accounted for 60.08% of total shape variance; G_2 accounted for 14.88% of total shape variance; and G_3 accounted for 11.35% of total shape variance. The degree of shared shape variance between G_1 and G_2 is -7.56° (=90° - 97.56°), between G_1 and G_3 is -29.84° (=90° - 119.84°), and between G_2 and G_3 is 29.48° (=90° - 82.96°). The correlation coefficient between G_1 and X_{S1} is 0.96, between G_2 and X_{S2} is -0.86, and between G_3 and X_{S3} is 0.73.The three data points describing the shape effects along negative, neutral, and positive gradients of deformation are centroid values of CV scores. All visualizations have been magnified by 3x (tpsRegr).

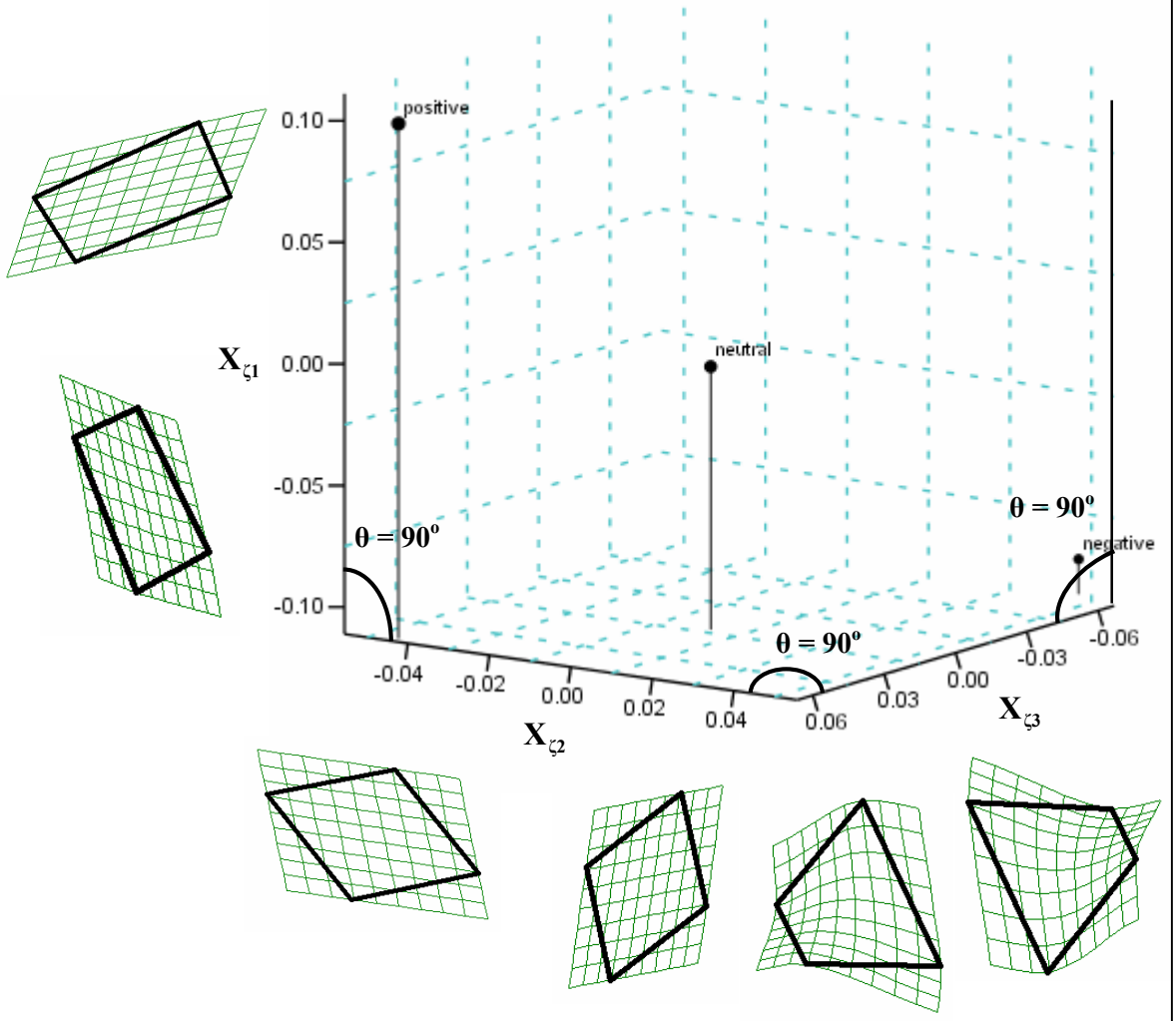

Figure 2.5. Thin-plate spline visualizations attributable to Burnaby PC scores describing the stretch effect ($X_{\zeta 1}$), the shear effect ($X_{\zeta 2}$), and the trapezoid effect ($X_{\zeta 3}$). $X_{\zeta 1}$ accounted for 50.03% of total shape variance; $X_{\zeta 2}$ accounted for 9.79% of total shape variance; and $X_{\zeta 3}$ accounted for 23.85% of total shape variance. The degree of shared shape variance between $X_{\zeta 1}$ and $X_{\zeta 2}$ is 0^o ($=90^o - 90^o$), between $X_{\zeta 1}$ and $X_{\zeta 3}$ is 0^o ($=90^o - 90^o$), and between $X_{\zeta 2}$ and $X_{\zeta 3}$ is 0^o ($=90^o - 90^o$). The correlation coefficient between $X_{\zeta 1}$ and X_{S1} is 0.97, between $X_{\zeta 2}$ and X_{S2} is -0.89, and between $X_{\zeta 3}$ and X_{S3} is 0.86. The three data points describing the shape effects along negative, neutral, and positive gradients of deformation are centroid values of Burnaby PC scores. All visualizations have been magnified by 3x (tpsRegr).

Clearly, PC scores (figures 2.3 and 2.5) yield accurate visulizations for all three effects and CV scores (figure 2.4) do not. The visual distortion produced by CVA is attributable to shear (not to be confused with the shear shape effect); CVA shears shape space so that variation among groups (H) is standardized by variation within groups (E), and therefore the orthogonality of the shape variables is lost because going from shape space to CV scores is a shear (i.e., $Q^TQ \neq I$), not a rotation like PC scores (i.e., $U^TU = I$).

Because the shapes were designed to be nearly orthogonal, there should not be a high degree of shared shape variance (θ - 90^o; equation 30) between effects. In figure 2.3, the degrees of shared shape variance between effects are within $\pm 10^o$, which is normal for this dataset because the predicted PC scores for each effect are describing the *natural* variation shared among groups. These scores do not produce visual distortion because their eigenvectors are just products of a rigid rotation of multivariate space.

In figure 2.4, the degrees of shared shape variance between effects were artificially inflated (due to matrix inversion; see equation 2.8) generating sheared visualizations and describing inaccurate shape variation among groups. CV scores describe the variation among groups relative to the variation within groups in order to optimally discriminate among groups. The variation within groups was designed to be slightly heteroscedastic, which according to some investigators should not pose a problem for CVA. However, it is apparent from this study that even a small degree of heteroscedasticity causes severe distortion. Therefore, CVA is not a reliable method.

In figure 2.5, the degrees of shared shape variance between effects were artificially reduced to 0^o generating orthogonal descriptions and visualizations of shape variation among groups. Burnaby PC scores describe the *pure* variation among groups. Predicted PC scores account for more shape variation (i.e., 50.28% + 9.98% + 24.11% = **84.37%**) than Burnaby PC scores (i.e., 50.03% + 9.79% + 23.85% = **83.67%**) because part of the variation is shared between effects. Burnaby PC scores, however, correct for the shared shape variance between effects making them much easier to interpret, which is the principal goal of any multivariate analysis.

Shared and unique features of diversification

This section is primarily concerned with the issue of producing visualizations that are not distorted and generating accurate plots of shared and unique axes of shape diversification among groups. Using morphometric data relevant to this dissertation, I describe an alternative method, that is, using the Burnaby PCA approach (equations 2.19 – 2.29), for generating shared and unique axes of shape diversification between still and flowing water habitats in three species of sunfishes.

Forty-three bluegill (BG; *L. macrochirus*), forty orange-spotted sunfish (OS; *L. humilis*), and fifty-five longear sunfish (LE; *L. megalotis*) were sampled by Winemiller et al. (2000) between the years of 1994 and 1996. Sunfishes were collected from the Brazos River (BR; flowing water habitat) and one Brazos River oxbow lake, Moehlman's Slough (MO; still water habitat). The fish were preserved in ethanol and were transported to the Texas Cooperative Wildlife Collections (TCWC), Texas A&M University, College Station for cataloging. The preserved and intact sunfishes were taken by permission from the TCWC and were x-rayed for morphometric analysis. Using freeware programs designed by F.J. Rohlf (e.g., tpsDig, tpsRegr, and tpsUtil), x-rays of sunfishes were analyzed by performing conventional methods of geometric morphometrics. Using tpsDig (ver 1.40), 15 type I homologous landmarks were obtained by digitizing an x-ray image from each of the 138 individual specimens representing the three species (figure 2.6). Then, using tpsRelw (ver. 1.42), one analysis of generalized Procrustes superimposition of landmark data followed by ordinary PCA was performed on the138 fish to obtain shape variables appropriate for statistical analysis:

$$\mathrm{Y} \equiv \begin{array}{c} \\ \\ \\ \\ \\ \\ 138 \end{array} \left[\begin{array}{l} \text{22 BG – BR} \\ \text{15 OS – BR} \\ \text{36 LE – BR} \\ \text{21 BG – MO} \\ \text{25 OS – MO} \\ \text{19 LE – MO} \end{array}\right] \begin{array}{c} 26 \\ \\ \\ \\ \\ \\ \\ \end{array}$$

Using statistical software JMP (ver. 5.0.1), MANCOVA was used to regress the 26 dependent (shape) variables on 7 known independent variables:

$$Y = f(\{sp\}, \{hab\}, \{cs\}, \{sp \times hab\}, \{sp \times cs\}, \{hab \times cs\}, \{sp \times hab \times cs\}, E) \ , \quad (2.31)$$

where sp ≡ species (BG, OS, and LE), hab ≡ habitats (river and oxbow; the shared shape effect within habitats), cs ≡ centroid size (continuous variable), sp x hab is the species-habitat interaction (2 unique shape effects between habitats), the remaining three interactions represent size (allometric) specific effects, and E (error) is unknown source of variance (i.e., variation remaining after accounting for the total predicted shape variation from the 7 known independent variables). Equation 2.31 is the analytical model that was evaluated under MANCOVA (i.e., a multivariate multiple regression analysis) in order to predict shape and to test the shape effects associated with the independent variables. Table 2.1 shows the results of the MANCOVA (p-statistic < 0.05 implies significance).

Table 2.1. Results of equation 2.31 (MANCOVA).

Effects	p-statistic
sp	0.0001
hab	0.0008
cs	0.0230
sp x hab	0.0046
sp x cs	0.4379
hab x cs	0.9413
sp x hab x cs	0.8597

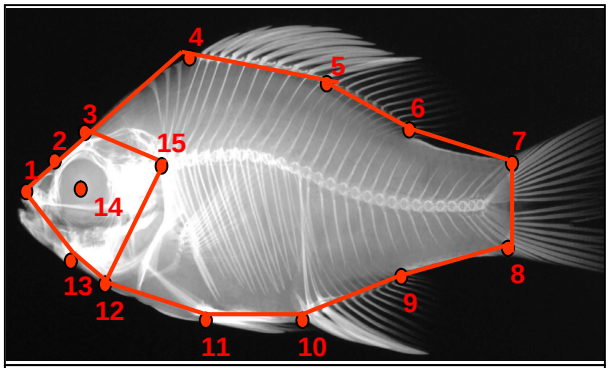

Figure 2.6. An x-ray of a typical bluegill digitized with 15 homologous landmarks using tpsDig.

Thus, predictions of shape on four statistically significant independent variables were extracted from equation 2.31:

$$Y_{p1} \equiv \text{species shape effect} \ , \quad (2.32)$$

$$Y_{p2} \equiv \text{habitat shape effect} \ , \quad (2.33)$$

$$Y_{p3} \equiv \text{centroid size shape effect} \ , \tag{2.34}$$

and

$$Y_{p4} \equiv \text{species x habitat shape effect} \ , \tag{2.35}$$

where Y_{p1} is the *138* x *26* predicted shape-by-species matrix, Y_{p2} is the *138* x *26* predicted shape-by-habitat matrix (i.e., the shared shape effect within habitats), Y_{p3} is the *138* x *26* predicted shape-by-centroid size matrix, and Y_{p4} is the *138* x *26* predicted shape-by-species-x-habitat matrix (i.e., the unique shape effects between habitats). Because shape variables are mean-centered, predicted variance-covariance matrices and their EDs were calculated directly from each Y_p:

$$H_1 = Y_{p1}^T Y_{p1} = U_{p1} \Lambda_{p1} U_{p1}^T \ , \tag{2.36}$$

$$H_2 = Y_{p2}^T Y_{p2} = U_{p2} \Lambda_{p2} U_{p2}^T \ , \tag{2.37}$$

$$H_3 = Y_{p3}^T Y_{p3} = U_{p3} \Lambda_{p3} U_{p3}^T \ , \tag{2.38}$$

and

$$H_4 = Y_{p4}^T Y_{p4} = U_{p4} \Lambda_{p4} U_{p4}^T \ , \tag{2.39}$$

where H_1 is the *26* x *26* predicted shape-by-species variance-covariance matrix, H_2 is the *26* x *26* predicted shape-by-habitat variance-covariance matrix, H_3 is the *26* x *26* predicted shape-by-centroid size variance-covariance matrix, and H_4 is the *26* x *26* predicted shape-by-species-habitat variance-covariance matrix. The eigenvector describing the shared shape effect within habitats is U_{p2} and the 2 eigenvectors describing the unique shape effects between habitats is U_{p4}.

At this stage, three analyses or approaches to generating shared and unique axes of shape diversification between habitats may proceed, which are the prediction PCA approach (equations 2.11 – 2.18), the conventional CVA approach (equations 2.5 – 2.10), and the Burnaby PCA approach (equations 2.19 – 2.29). I begin with the prediction PCA approach:

$$X_{p2} = YU_2^T \quad , \tag{2.40}$$

where X_{p2} is the *138* x *1* vector of predicted PC scores describing the shared axis of shape diversification between habitats, and:

$$X_{p4} = YU_4^T \quad , \tag{2.41}$$

where X_{p4} is the *138* x *2* matrix of predicted PC scores describing the 2 orthogonal unique axes (i.e., X_{p4}^{1} and X_{p4}^{2}) of shape diversification between habitats (figure 2.7).

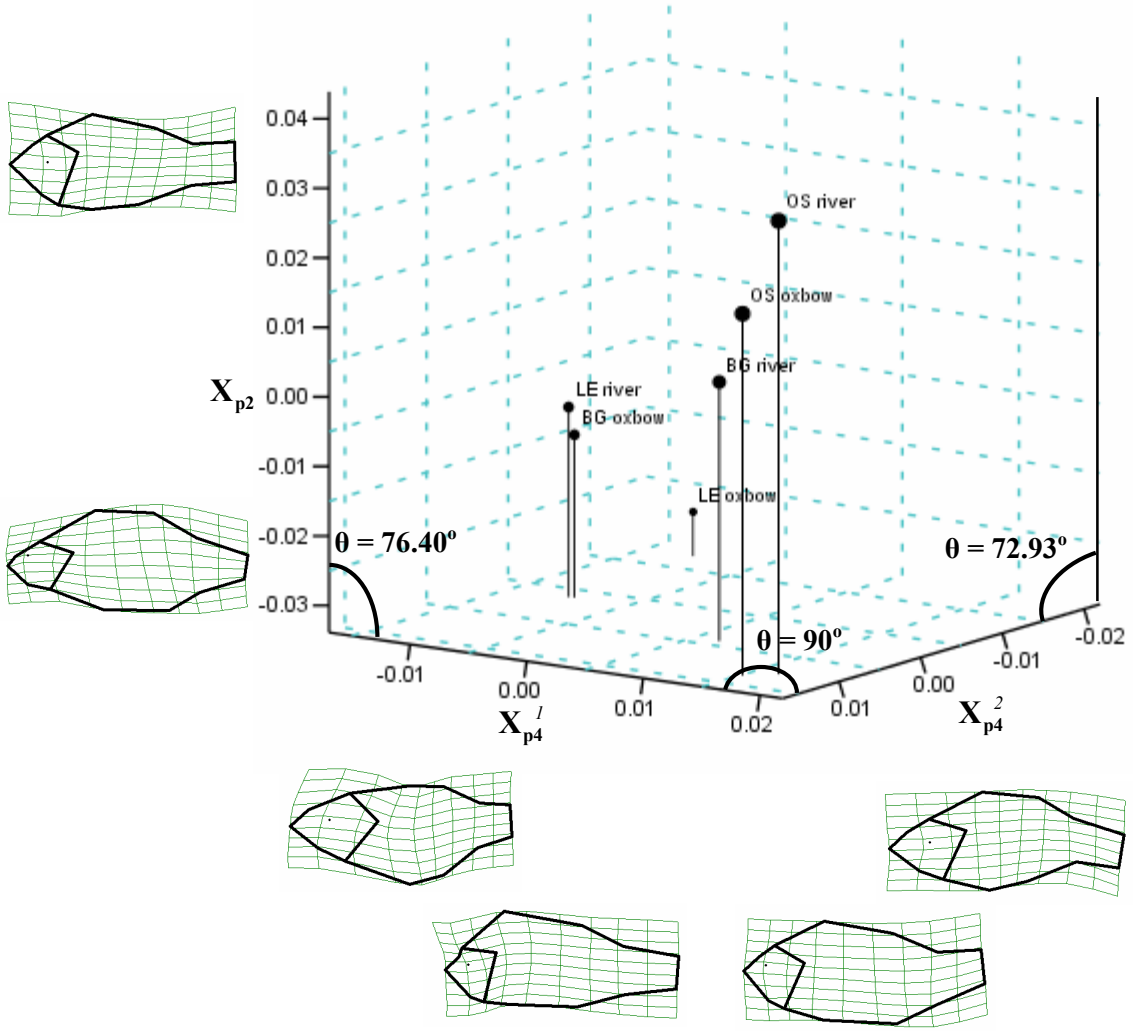

Figure 2.7. Thin-plate spline visualizations attributable to predicted PC scores describing shared (X_{p2}) and unique features (X_{p4}^{1} and X_{p4}^{2}) of shape diversification between habitats in three species of sunfish. X_{p2} accounted for 0.75% of total shape variance in Y; X_{p4}^{1} accounted for 1.16% of total shape variance in Y; and X_{p4}^{2} accounted for 0.32% of total shape variance in Y. The degree of shared shape variance between X_{p2} and X_{p4}^{1} is 13.60° (=90° - 76.40°), between X_{p2} and X_{p4}^{2} is 17.07° (=90° - 72.93°), and between X_{p4}^{1} and X_{p4}^{2} is 0° (=90° - 90°). The correlation coefficient between X_{p2} and X_{S2} is 0.26, between X_{p4}^{1} and X_{S4}^{1} is -0.40, and between X_{p4}^{2} and X_{S4}^{2} is 0.08. The six data points describing the shape effects are centroid values of predicted PC scores. All visualizations have been magnified by 3x (tpsRegr).

Figure 2.7 is an incorrect representation of shared and unique features of shape diversification between habitats because variation is shared between effects (i.e., $\theta \neq 90^{o}$), except between X_{p4}^{1} and X_{p4}^{2} (because $U_{p4}^{T}U_{p4} = I$). This is the reason X_{p2} does not describe a shared shape effect within habitats (i.e., both river and oxbow in positive X_{p2} axis and both river and oxbow in negative X_{p2} axis). Figure 2.7 only represents the *natural* variation shared between effects. The visualizations, however, are not distorted.

The conventional CVA approach is perhaps the worst analysis for generating shared and unique axes of shape diversification among groups. It is for this reason I describe the approach in order to expose its inherent problems. The only relevant difference between PCA and CVA is that the E matrix in equation 2.31 is inverted and then multiplied by equations 2.37 and 2.39 prior to ED:

$$E^{-1}H_2 \Rightarrow Q_2K_2 \quad , \tag{2.42}$$

$$G_2 = YQ_2^{T} \quad , \tag{2.43}$$

where G_2 is the *138* x *1* vector of CV scores describing the shared axis of shape diversification between habitats relative to E, and:

$$E^{-1}H_4 \Rightarrow Q_4K_4 \quad , \tag{2.44}$$

$$G_4 = YQ_4^{T} \quad , \tag{2.45}$$

where G_4 is the *138* x *2* matrix of CV scores describing the 2 unique axes (i.e., G_4^{1} and G_4^{2}) of shape diversification between habitats relative to E (figure 2.8).

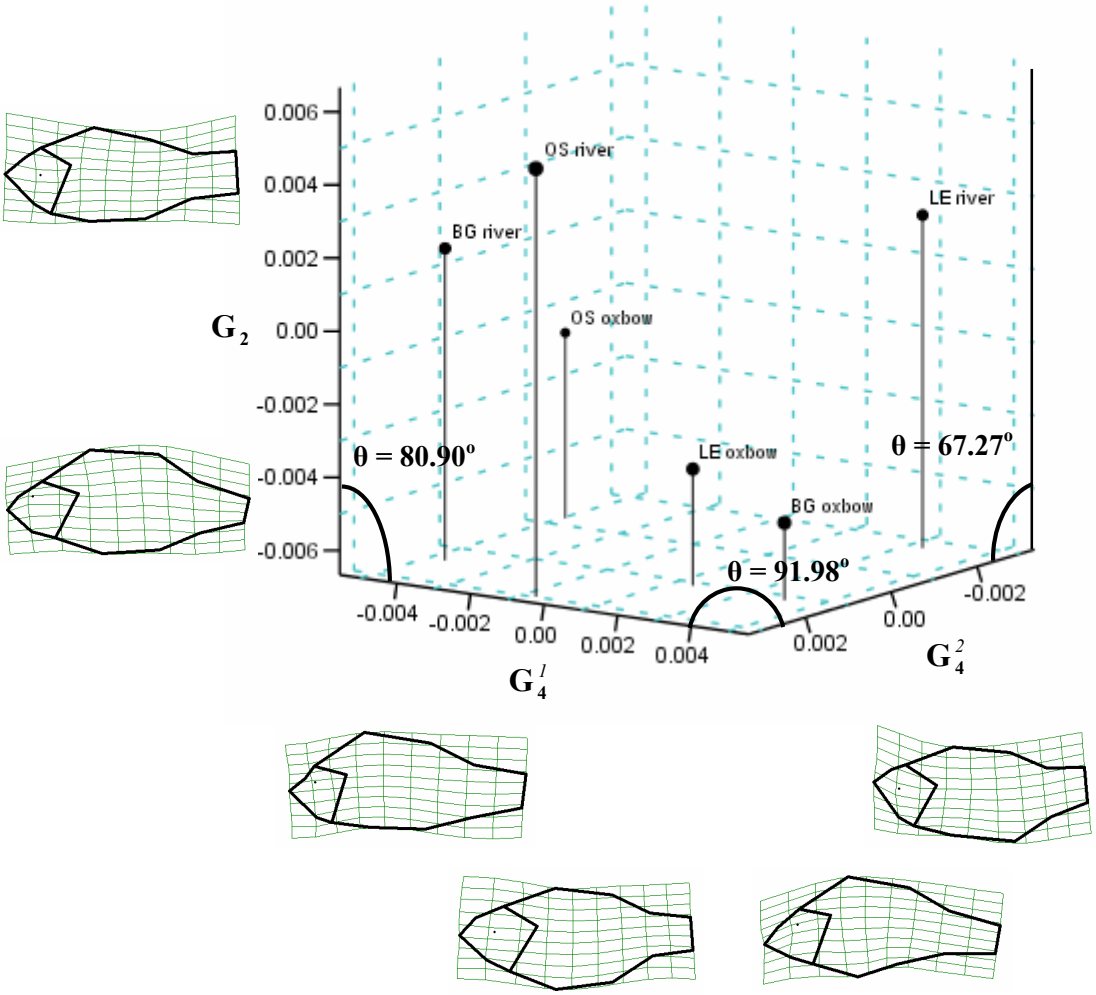

Figure 2.8. Thin-plate spline visualizations attributable to CV scores describing shared (G_2) and unqiue features (G_4^1 and G_4^2) of shape diversification between habitats in three species of sunfish. G_2 accounted for 1.31% of total shape variance in Y; G_4^1 accounted for 1.21% of total shape variance in Y; and G_4^2 accounted for 0.64% of total shape variance in Y. The degree of shared shape variance between G_2 and G_4^1 is 9.10° (=90° - 80.90°), between G_2 and G_4^2 is 22.73° (=90° - 67.27°), and between G_4^1 and G_4^2 is -1.98° (=90° - 91.98°). The correlation coefficient between G_2 and X_{S2} is 0.63, between G_4^1 and X_{S4}^1 is -0.50, and between G_4^2 and X_{S4}^2 is 0.33. The three data points describing the shape effects along habitats and species are centroid values of CV scores. All visualizations have been magnified by 3x (tpsRegr).

Figure 2.8 is an incorrect representation of shared and unique features of shape diversification because shape variation is shared between effects; the degrees of shared shape variance have been artificially inflated due to inversion of E. However, the conventional CVA approach does effectively discriminate between habitats, that is, G_2 represents a shared shape effect within habitats (i.e., river in positive G_2 axis and oxbow in negative G_2 axis). This is the only aspect of CVA that has appeal. But, the visualizations attributable to CV scores are not reliable because they are distorted; shape regressed on CV scores produces shear and thus geometric orthogonality of shape space is lost.

The Burnaby PCA approach is perhaps the best analysis for generating shared and unique axes of shape diversification among groups. The mathematics of the Burnaby PCA approach is easy to implement because it does not deviate much from the ordinary PCA approach. The only difference between the two approaches is that equation 2.19 was applied to equations 2.37 and 2.39 in order to orthogonalize (i.e., remove shared variation) between effects:

$$\mathbf{H}_{\zeta 2} = \mathbf{H}_2 - (\mathbf{H}_1 + \mathbf{H}_3 + \mathbf{H}_4) = \mathbf{U}_{\zeta 2}\boldsymbol{\Lambda}_{\zeta 2}\mathbf{U}_{\zeta 2}^{\mathrm{T}} \quad , \tag{2.46}$$

$$\mathbf{X}_{\zeta 2} = \mathbf{Y}\mathbf{U}_{\zeta 2}^{\mathrm{T}} \quad , \tag{2.47}$$

where $\mathbf{X}_{\zeta 2}$ is a *138* x *1* vector of Burnaby PC scores describing the shared axis of shape diversification between habitats excluding shape variation from all other effects, and:

$$\mathbf{H}_{\zeta 4} = \mathbf{H}_4 - (\mathbf{H}_1 + \mathbf{H}_2 + \mathbf{H}_3) = \mathbf{U}_{\zeta 4}\boldsymbol{\Lambda}_{\zeta 4}\mathbf{U}_{\zeta 4}^{\mathrm{T}} \quad , \tag{2.48}$$

$$\mathbf{X}_{\zeta 4} = \mathbf{Y}\mathbf{U}_{\zeta 4}^{\mathrm{T}} \quad , \tag{2.49}$$

where $\mathbf{X}_{\zeta 4}$ is the *138* x *2* matrix of Burnaby PC scores describing the unique axes of shape diversification between habitats excluding shape variation from all other effects (figure 2.9).

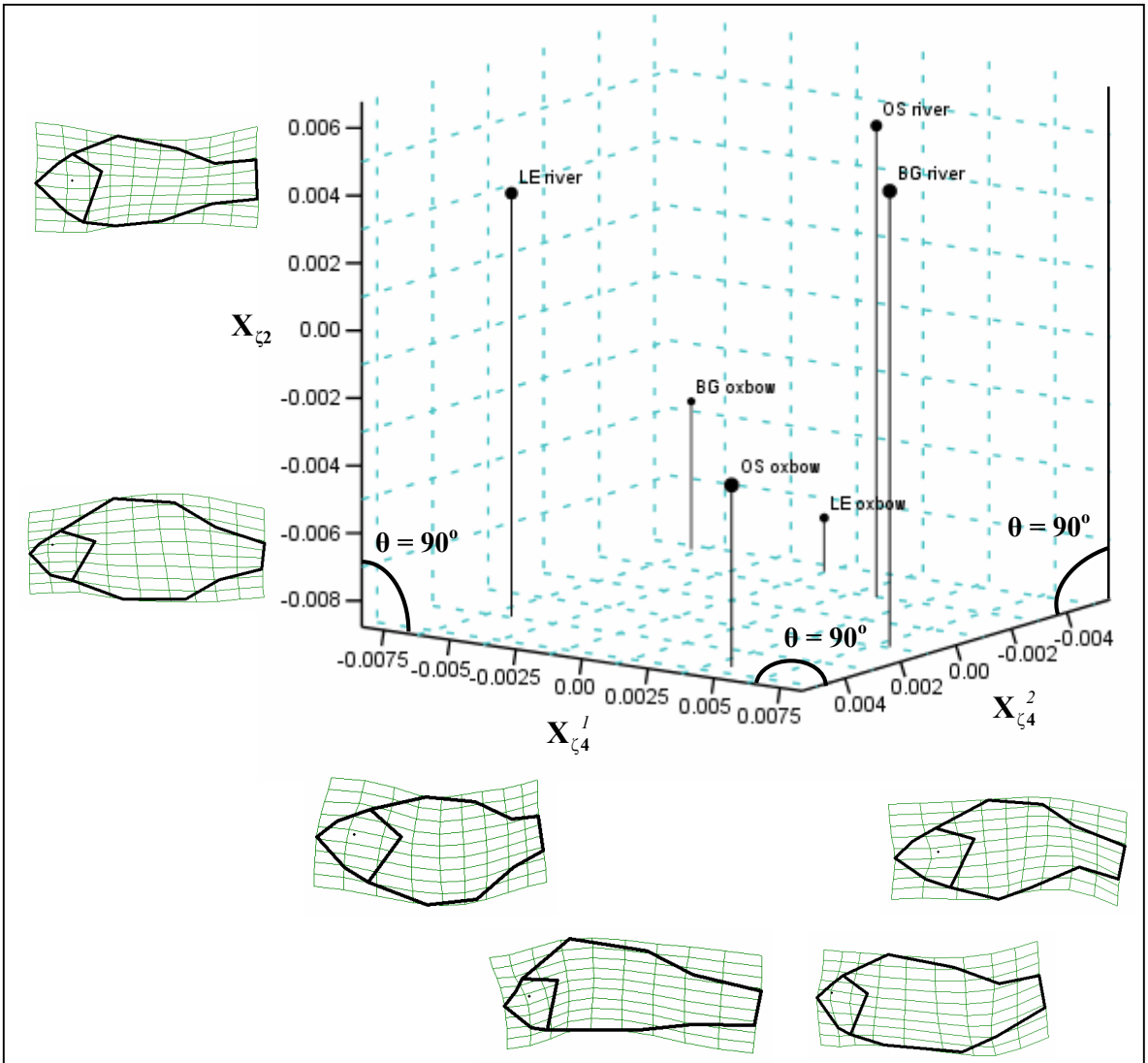

Figure 2.9. Thin-plate spline visualizations attributable to Burnaby PC scores describing shared ($X_{\zeta 2}$) and unique features ($X_{\zeta 4}^{1}$ and $X_{\zeta 4}^{2}$) of shape diversification between habitats in three species of sunfish. $X_{\zeta 2}$ accounted for 0.39% of total shape variance in Y; $X_{\zeta 4}^{1}$ accounted for 0.94% of total shape variance in Y; and $X_{\zeta 4}^{2}$ accounted for 0.26% of total shape variance in Y. The degree of shared shape variance between $X_{\zeta 2}$ and $X_{\zeta 4}^{1}$ is 0° (=90° - 90°), between $X_{\zeta 2}$ and $X_{\zeta 4}^{2}$ is 0° (=90° - 90°), and between $X_{\zeta 4}^{1}$ and $X_{\zeta 4}^{2}$ is 0° (=90° - 90°). The correlation coefficient between $X_{\zeta 2}$ and X_{S2} is -0.55, between $X_{\zeta 4}^{1}$ and X_{S4}^{1} is -0.32, and between $X_{\zeta 4}^{2}$ and X_{S4}^{2} is 0.27. The three data points describing the shape effects along habitats and species are centroid values of Burnaby PC scores. All visualizations have been magnified by 3x (tpsRegr).

Figure 2.9 is a correct representation of shared and unique features of shape diversification between habitats because shared variation was artificially removed between effects. Thus, shape variation is separated between axes. This is the reason $X_{\zeta 2}$ describes a shared shape effect within habitats (i.e., river in positive $X_{\zeta 2}$ axis and oxbow in negative $X_{\zeta 2}$ axis). Specifically $X_{\zeta 2}$ is a characterization of shape divergence between habitats and a characterization of shape convergence within habitats. The visualizations attributable to Burnaby PC scores are not distorted because they (like all PC scores) are derived from orthonormal eigenvectors that only rotate multivariate data thus preserving the geometric orthogonality of shape space.

The shared shape effect ($X_{\zeta 2}$) within the river (positive axis) can be described generally as shallow-bodied for all three species; and, the shared shape effect within the oxbow lake (negative axis) can be described generally as deep-bodied for all three species. I describe the $X_{\zeta 2}$ shape axis as a shallow- and deep-bodied divergent shape generalization, which can be visualized more effectively by decomposing the $X_{\zeta 2}$ shape axis into its uniform shape deformation components, that is, compression/dilation (contraction /elongation) and shear. Zelditch et al. (2004) provides an excellent geometric interpretation of uniform and non-uniform components of a shape deformation (see pp. 134). In this study, uniform deformations are important to visualize because according to Landweber (1961), Webb (1975), and Blake (1983) the ratio of maximum body length (horizontal distance) over maximum body depth (vertical distance) is used to describe body slenderness. This ratio is referred to as the 2-dimensional (2-D) fineness ratio (Landweber, 1961), which becomes an important factor in fluid dynamics (discussed in the next chapter). The uniform components of shape deformation are a multivariate characterization of the 2-D fineness ratio, because compression/dilation refers to the case in which one direction has contracted (the horizontal ≡ body length) while the other has elongated (the vertical ≡ body depth). Uniform shape deformation scores are more descriptive and statistically robust than fineness ratios and therefore much better to use and visualize when assessing body

slenderness. In this dissertation, I define shallow- and deep-bodied as the level of body slenderness, which consequently is assessed from the visualizations of uniform shape deformations. Using tpsRegr, the uniform shape deformations of $X_{\zeta 2}$ can be visualized (figure 2.10). It should be noted that the $X_{\zeta 4}^{1}$ shape axis also describes a shallow- and deep-bodied divergent shape generalization in bluegills between river and oxbow habitats, but not for the other two species—longear sunfishes tend to be relatively deep-bodied (negative $X_{\zeta 4}^{1}$ axis), and orange-spotted sunfishes tend to be relatively shallow-bodied (positive $X_{\zeta 4}^{1}$ axis).

In conclusion, CVA is not a reliable method, because it produces visual distortion and counterintuitive results. Ordinary PCA is a raw ordination describing variation in one block, where a multivariate regression analysis in not required to derive the block. Prediction PCA is an ordination describing variation in one predicted block, where a multivariate regression analysis is required to derive the block. Two special types of prediction PCA were addressed: (1) IVS, which are scores perfectly correlated with their predictors (dummy or surrogate variables); (2) Burnaby PCA, which is used to orthogonalize eigenvectors (i.e., remove shared variation) between effects. IVS are the only PC scores that do not account for variation—they are used simply for prediction.

I am focusing only on bluegill for the remainder of this dissertation because, according to figure 2.9, this species of sunfish yields the largest overall Euclidean distance of shared and unique shape divergence between river and oxbow habitats (table 2.2).

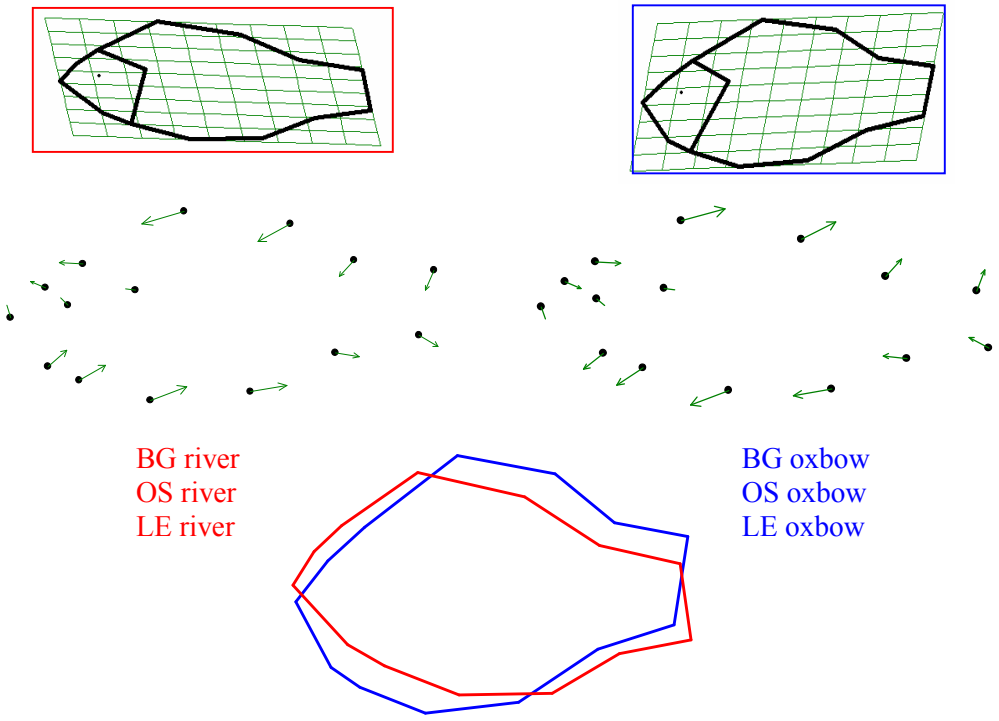

Figure 2.10. Uniform shape deformation of $X_{\zeta 2}$. *Left*—shallow-bodied visualization; vector projections pointing inward (compression). *Right*—deep-bodied visualization; vector projections pointing outward (dilation). *Bottom*—overlay of uniform shape deformation of $X_{\zeta 2}$ (red ≡ shallow-bodied; blue ≡ deep-bodied).

Table 2.2. Euclidean distances between three species of sunfish and two habitats across $X_{\zeta 2}$, $X_{\zeta 4}^{1}$, and $X_{\zeta 4}^{2}$ (see figure 2.9).

	BG river	BG oxbow	OS river	OS oxbow	LE river	LE oxbow
BG river	0	**0.017114**	0.006035	0.009133	0.012418	0.013719
BG oxbow	**0.017114**	0	0.013103	0.014362	0.011188	0.00959
OS river	0.006035	0.013103	0	**0.01156**	0.009744	0.012468
OS oxbow	0.009133	0.014362	**0.01156**	0	0.012319	0.009841
LE river	0.012418	0.011188	0.009744	0.012319	0	**0.015437**
LE oxbow	0.013719	0.00959	0.012468	0.009841	**0.015437**	0

CHAPTER III
FORCES OF NATURE: BODY SHAPE, WATER FLOW, AND THE CONCEPT OF THE FINENESS RATIO IN FLUID DYNAMICS

Nature is pleased with simplicity, and affects not the pomp of superfluous causes.

— Isaac Newton (1642–1727)

Introduction

In chapter II, I evaluated the shared axis of shape diversification between flowing (Brazos River) and still-water (Moehlman's Slough) habitats and visualized the shared shape effect within habitats for three species of sunfish: the shared shape effect within the river can be described generally as shallow-bodied for all three species and the shared shape effect within the oxbow lake can be described generally as deep-bodied for all three species (figure 2.9). In chapter I, I proposed the hypothesis that water flow is the likely factor driving the shallow- and deep-bodied generalization of shape diversification in fish (a hypothesis based on the empirical findings of Scarnecchia, 1988) because of a potential fitness trade-off between aerobic swimming efficiency (low swimming costs → shallow-bodied) and standard metabolism (low maintenance costs → deep-bodied). Body shape adaptations in fish aim at reducing hydrodynamic drag (resistance), thereby reducing metabolic work (Wu, 1971; Webb, 1975; Vogel, 1981; Scarnechhia, 1988). To obtain large thrust and high swimming efficiency, a fish should be slender and have a long and deep caudal peduncle to execute a large amplitude movement (Bainbridge, 1958, 1963; Newman, 1973; Newman and Wu, 1973; Yates, 1983; Fung, 1990).

There are three environmental (extrinsic) factors that contribute to hydrodynamic resistance: water density, water flow, and viscosity (Newman, 1973). Increasing water density, water flow, or viscosity makes it difficult for fish to move through the water, thereby increasing its metabolic demand for swimming. Therefore, there are direct hydrodynamic costs corresponding to the shallow- and deep-bodied divergent shape

generalization in fish due to selective pressures associated with water density, water flow, and viscosity. All three extrinsic factors affect the force acting on a fish's body (Newman, 1973). Clearly, the force also depends on other important factors such as the geometry of the fish's body and swimming behavior (Lighthill, 1969; Chwang and Wu, 1974–1976; Webb, 1975; Fung, 1990; Pettersson and Hedenström, 2000). I refer to these two features as intrinsic factors contributing to hydrodynamic resistance because they are components of the fish, not of the environment. A dimensional analysis of fluid dynamics is used to determine how extrinsic and intrinsic factors contribute to hydrodynamic resistance in fish. Below, I describe only the tangential (resistive) forces fish experience from the surrounding water using the "reactive force" theory of swimming developed by Lighthill (1975).

The force (F) exerted by the water on a fish's body is characterized by the equation (Fung, 1990):

$$F = f(\alpha, R)q \quad , \tag{3.1}$$

where q is the dynamic pressure (force) and f represents a function of both the fish's attitude relative to the flow (typical angle; α) and the Reynolds number (R). The dynamic force (q) is characterized by the equation:

$$q = \frac{1}{2}\rho\lambda^2\left[\left(1-\frac{w_1}{w_2}\right)w_2\right]^2 = \frac{1}{2}\rho\lambda^2 U^2 \quad , \tag{3.2}$$

where ρ is the density of water, λ is the inverse fineness distance (my own characterization modified from the fineness ratio—see Landweber, 1961; Webb, 1975; Blake, 1983; Walker, 2004), w_1 is the forward (swimming) speed of the fish, and w_2 is the wave speed (i.e., the speed of water flow passing backward along the fish's spine). Taken together, w_1 and w_2 compose the relative velocity U, because resistance means force acting on a body in the direction of the motion relative to the fluid (Fung, 1990). Parameter w_2 depends on the joint (additive) effects of w_1 and the rate of external water

flow (denoted w_2^f) moving in the direction relative to w_1 (Fung, 1990). Thus, if $w_1 \neq 0$, then $w_2 >> w_1$ (with w_2^f) or $w_2 > w_1$ (without w_2^f); and if $w_1 = 0$, then $w_2 \neq 0$ (with w_2^f) or $w_2 = 0$ (without w_2^f). Hence, F (equation 3.1) is equal to 0 only when w_1 and w_2 are both equal to 0. The Reynolds number (R) is characterized by the equation:

$$R = \frac{U L \rho}{\mu} , \tag{3.3}$$

where L is the maximum body length and μ is the viscosity of water. The inverse fineness distance (λ) is characterized by the equation:

$$\lambda = \frac{DB}{L} , \tag{3.4}$$

where D is the maximum body depth and B is the maximum body breadth. Fung (1990) describes equation 3.2 for a flat plate, where λ = L. However, a flat plate is an inaccurate geometric description of fish, because they are better described as ellipsoids, where D and B relative to L describes distance of body roundness, which is directly proportional to F (Landweber, 1961; Webb, 1975; Blake, 1983). Thus, the force of resistance (F_d) is characterized by the equation:

$$F_d = \left(\frac{1}{2}\rho U^2 \lambda^2\right)\left(\frac{\eta}{R^{\gamma}}\right) = qC_d , \tag{3.5}$$

where η is a dimensionless constant greater than 0 (depends on α) and γ is a dimensionless constant greater than 0 and less than 1 (depends on λ). The dimensionless term in equation 3.5, $\eta R^{-\gamma}$, is the coefficient of resistance (C_d), which is a function of R. The coefficient of resistance (C_d) is also a function of the Strouhal number and the Mach number (see Fung, 1990, pp. 63), but both vanish in a steady flow of an incompressible fluid (Fung, 1990). Therefore, C_d depends only on R, η, and γ, where η and γ can be determined experimentally (Fung, 1990). Active respirometry is a popular

method to determine C_d. From active respirometry, metabolic power ($=F_d U$) can be calculated by subtracting the standard metabolic rate from the total metabolic rate measured at different Us and then applying the standard energy conversion factors. Next, the coefficient of power (C_p; a dimensionless variable) can be calculated by dividing the values of $F_d U$ by the values of qU. Finally, one relates dependent variable C_p to independent variable R. This nonlinear relationship between C_p and R yields the inverse power function, $\eta R^{-\gamma}$ ($=C_p=C_d$). Although this analysis seems easy, determining the relative velocity (U) can be difficult. Thus, some investigators use the hydrodynamics-based power function (discussed in great detail in the next chapter) and substitute w_2^f, which is a component of w_2, for w_1. Then, the conventional notation used to describe w_1 is U (chapters IV and V).

Equation 3.5 takes into account two out of three known sources of resistance; they are pressure (form) resistance, $F_d = f(q, \gamma)$, and induced resistance, $F_d = f(q, \eta)$. The third source of resistance is skin friction, which is the shear stress associated with viscosity and shear strain in the boundary layer attached to the surface of the body (Fung, 1990). Skin friction, unfortunately, is the hardest to measure because investigators have not been able to adequately predict C_d as a function of R for a flat plate in a uniform flow when turbulence is involved (Fung, 1990). Thus, I ignore skin friction as a source of hydrodynamic resistance.

From equations 3.1 – 3.5, it is easy to determine the main extrinsic and intrinsic factors contributing to hydrodynamic resistance. The extrinsic factors are ρ, w_2^f, and μ. The intrinsic factors are α, w_1, and λ. Thus, hydromechanical conditioning of swimming efficiency is due to six factors contributing to hydrodynamic resistance: α, w_1, λ, ρ, w_2^f, and μ.

Body shape (λ) is one of the most important intrinsic factors contributing to hydrodynamic resistance (Breder, 1926; Brett, 1963; Chwang and Wu, 1974–1976; Lighthill, 1969; Newman and Wu, 1973; Yates, 1983; Scarnecchia, 1988). Water flow

(w_2^f) is the main extrinsic factor contributing to hydrodynamic resistance in bluegills. Presumably, water density (ρ) contributes little to hydrodynamic resistance in bluegills from lakes, because bluegills predominately reside in the epilimnion (i.e., in the aquatic plant zone) to feed on aquatic insects (Moyle and Cech, 2004); and, dense water sinks far below the epilimnion. For slender aquatic animals with cylinder-like bodies, where D ≅ B, such as the nematode and water snake, the main force of interaction between the animal and the surrounding fluid is considered to be the resistance caused by the viscosity (μ) of the fluid (Fung, 1990). Because bluegills are relatively deep-bodied fishes, where D >> B, μ is not a major contributor of hydrodynamic resistance in this species. Figure 3.1 shows the relationship of the relative contributions of λ, w_2^f (= w_2 when $w_1 = 0$), ρ, and μ to hydrodynamic resistance (F_d), when η = 15.4 and γ = 0.4 (values taken from Fung, 1990, pp. 145).

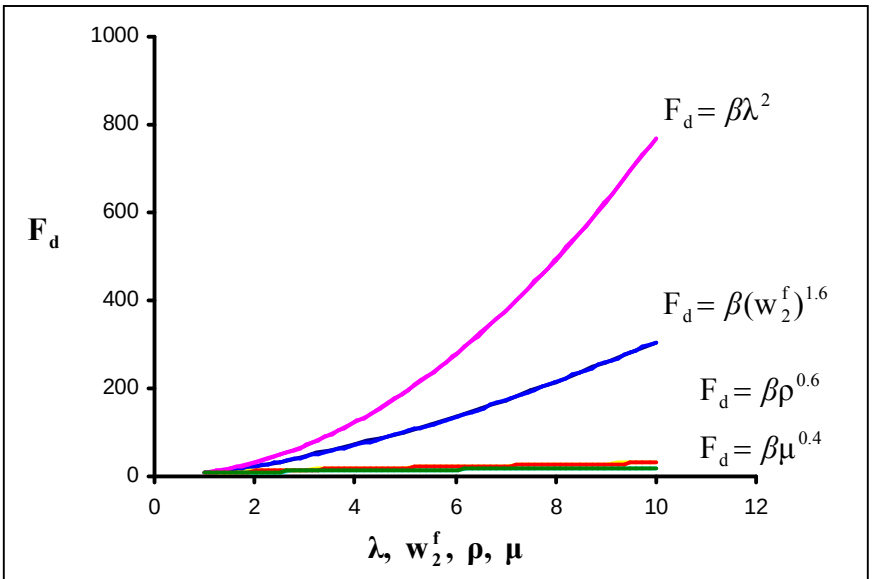

Figure 3.1. The relationship of the relative (= equal weights; *β*) contribution of body shape (*pink* – λ), water flow (*blue* – w_2^f), water density (*red* – ρ), and viscosity (*green* – μ) to hydrodynamic resistance (F_d). Body shape and water flow are the main factors contributing to hydrodynamic resistance in fish; water density and viscosity are relatively negligible.

Force of resistance and body shape

Although swimming behavior has profound effects on swimming efficiency (for it contributes to induced resistance via α), it will not be assessed in this dissertation because it involves a direct measurement of F_d, which can be very difficult (Fung, 1990). Also, I am not concerned with the evolution of swimming behavior in fish; rather, I am concerned with the evolution of body shape. The swimming speed of a fish (w_1) is a voluntary intrinsic factor contributing to hydrodynamic resistance because fish can choose not to swim fast unless, of course, forced to by catching prey, escaping predators, or by the need to stem a current. According to Pettersson and Hendenström (2000), low-F_d morphs (lower λ) can use a broader range of w_1; whereas in high-F_d morphs (higher λ) swimming costs increased significantly when deviating from the optimum w_1. These results suggest that fish use different ranges of w_1 depending on their body shape (λ). Therefore, the range of w_1 is constrained in fishes so that F_d remains as low as possible. Although swimming speed (w_1) is an interesting parameter from an ecological perspective, it clearly contributes little to hydrodynamic resistance, which makes it uninteresting with respect to body shape adaptations. Parameter λ, on the other hand, is an involuntary intrinsic factor contributing to hydrodynamic resistance because fish cannot control their body shape—that is, body shape is governed by evolution, which makes it very interesting to analyze with respect to swimming performance and, consequently, fitness.

Parameter λ treats body shape simplistically and therefore is mathematically very practical. Multivariate body shape (from the thin-plate spline visualizations), on the other hand, is a much more complete description than λ but less mathematically practical. Thus, for mathematical purposes, I will use λ to represent body shape; and for visual and statistical purposes, I will use thin-plate spline (multivariate morphometrics) to represent and statistically evaluate the relationship between body shape and swimming performance. Both representations of body shape are useful and should be

used together in formulating hypotheses and analyses, especially in regard to hydrodynamics.

The inverse fineness distance (λ) is squared in equation 3.5, thus representing the inverse fineness area of body shape. It should be noted that λ^2 does not describe the surface area of an ellipsoid; rather, it describes area of body roundness relative to length, which gives information about the deepening (as oppose to streamlining) of a fish. The parameter λ is a novel characterization based on the fineness ratio (ς), which is a dimensionless factor of body slenderness used to determine the influence of shape on the resistance of a moving body in water (Landweber, 1961; Webb, 1975; Blake, 1983; Walker, 2004; Ohlberger et al., 2006):

$$\varsigma = \frac{L}{\sqrt{DB}} \tag{3.6}$$

To preserve hydrodynamic reliability—based on the findings of Landweber (1961), Webb (1975), and Blake (1983)—and unit continuity in equations 3.1 and 3.5, equation 3.6 was inverted and then dimensionalized. Because equation 3.4 is an inverse measure of equation 3.6, F_d increases when λ increases, with all other parameters held constant. This implies that round and short fish are constrained to executing only small amplitude movements through water, which makes them less efficient swimmers and subjected to very high resistance forces. This analysis is in accordance with the findings of Wu (1971), Webb (1975), Blake (1983), Scarnecchia (1988), Pettersson and Hedenström (2000), Svanbäck and Eklöv (2004), and Ohlberger et al. (2006). Round and short fish, no matter how much less efficient they are at swimming, are in fact more efficient at maneuvering or revolving in water (Chwang and Wu, 1974–1976; Webb, 1975; Svanbäck and Eklöv, 2004). This is a trade-off in hydromechanics. So, when would it be better for fish to be efficient swimmers? And, when would it better for fish to be efficient at maneuvering? Svanbäck and Eklöv (2004) determined that a functional trade-off exists between foraging performance and body shape. They showed that shallow-bodied fish are more efficient at feeding in open water due to a higher stability (i.e.,

higher swimming efficiency), while deep-bodied fish are more efficient at foraging in the vegetation due to a higher maneuverability (Ohlberger et al., 2006).

Force of resistance and water flow

F_d increases when w_2^f increases, with all other parameters held constant (and $w_1 = 0$), because relative velocity (U) is squared in q and is raised to a power less than 1 in R in equation 3.5. Water flow (w_2^f) is referred to as a direct eco-morphological factor because body shape (λ) also contributes to hydrodynamic resistance. Fish have no control over w_2^f; and, natural selection governs λ. Thus, body shape adaptations aim at reducing hydrodynamic resistance in the presence of w_2^f, thereby increasing swimming efficiency. In figure 2.9, it is clear that sunfish from the river are significantly more shallow-bodied than sunfish from the oxbow lake; and, from first principles there exists, under a water flow-rate regime, hydrodynamic costs associated with this divergent shape axis (Blake, 1983; Vogel, 1981; Scarnecchia, 1988; Svanbäck and Eklöv, 2004; Ohlberger et al., 2006). Hypothetically, there might be ecological factors other than w_2^f that drive the shallow- and deep-bodied divergent shape generalization in sunfish, but these factors would be considered indirect and therefore much harder to support from first principles. Hence, the general framework from which I derive any hypothesis herein is supported from first principles, that is, from fluid dynamics (equations 3.1 – 3.5). For this reason, I conclude that w_2^f is mainly responsible for contributing to the shallow- and deep-bodied divergent shape generalization in sunfish (figure 2.9). What about bluegills from oxbow lakes? If water flow drives a shallow- and deep-bodied divergent shape generalization, then this shape generalization should not exist in bluegills among oxbow lakes. Therefore, the main question is, is there a shallow- and deep-bodied divergent shape generalization in bluegills among oxbows lakes, where $w_2^f = 0$? Using principal components analysis (PCA), I describe body shape variation in the Brazos River and six Brazos River oxbow lakes.

Specimens

Bluegills used in this study were collected by Winemiller et al. (2000) between the years of 1994 and 1996 and were sampled from the Brazos River and Brazos River oxbow lakes. The bluegills sampled were preserved in ethanol and transported to the Texas Cooperative Wildlife Collections (TCWC), Texas A&M University, College Station for cataloging. The preserved and intact bluegills were then taken by permission from the TCWC in 2004 and were x-rayed for morphometric analysis. Using freeware programs designed by F.J. Rohlf (tpsDig, tpsRegr, tpsSplin, and tpsUtil), x-rays of bluegills were analyzed by performing conventional methods of geometric morphometrics (see chapter I for details). Only bluegills from the Brazos River and six Brazos River oxbow lakes (i.e., Korthauer Bottom, Mexican Bend, Moehlman's Slough, PAC II Lake, Perry Lake, and Stone Lake) were used in this study.

Fifteen 2-dimensional homologous landmarks (coordinates) were chosen to represent body shape for each bluegill (see figure 2.6). Generalized Procustes analysis of the 15 homologous coordinates resulted in 26 statistically appropriate shape variables. A total of 145 bluegills were used: 22 from Brazos River (BR), 27 from PAC II Lake (PA), 23 from Stone Lake (ST), 22 from Korthauer Bottom (KH), 21 from Moehlman's Slough (MO), 20 from Perry Lake (PR), and 10 from Mexican Bend (MX):

$$Y \equiv \begin{matrix} \\ 22\ BR \\ 27\ PA \\ 23\ ST \\ 22\ KH \\ 21\ MO \\ 20\ PR \\ 10\ MX \\ \\ 145 \end{matrix} \begin{matrix} \\ \\ \\ \\ \\ \\ \\ \\ 26 \end{matrix}$$

Size (allometric) variation was removed from shape because bluegills of different size showed different body shapes. Burnaby's 1966 method (equation 2.19) was used to remove allometric effects from shape. Allometric variation is typically associated with a shallow- and deep-bodied divergent shape generalization among individuals, where smaller bluegills are much more shallow-bodied than larger bluegills. This is not a

surprising feature for small fish, in general, because F_d increases considerably due to a small decrease in L. In other words, F_d is directly proportional to λ^2; and λ^2 is inversely proportional to L; also, F_d is inversely proportional to R; and R is directly proportional to L. Therefore, from an ontogenetic perspective, D and B in λ (equation 3.4) must decrease considerably in order to compensate for a small value of L. So, based on hydrodynamic principles, smaller fish should be more shallow-bodied than larger fish.

Using data block Y, I address the distinction of the shallow- and deep-bodied divergent shape generalization between the river-oxbows (water flow; w_2^f) shape effect and the allometric (centroid size; cs) shape effect.

Diversification between river and oxbow lake

Water flow (w_2^f) is a 2-group (e.g., binary) categorical variable, where the Brazos River represents flowing water (i.e., $w_2 >> w_1$) and the six oxbows represent still water (i.e., $w_2 > w_1$). In order to remove w_2^f from an analysis, bluegills from the Brazos River must be excluded from the six oxbows because w_2^f is an internal variable defined by bluegill shape from the Brazos River.

Although a shallow- and deep-bodied divergent shape generalization between river and oxbow lake habitats has been shown in three species of sunfish (see figure 2.9), Burnaby PCA strongly reinforces this shape generalization in bluegills, where:

$$Y = f(\{w_2^f\}, \{cs\}, \{w_2^f \times cs\}, error) \qquad (3.7)$$

Equation 3.7 defines the analytical model of a multivariate multiple regression analysis, where multivariate shape (Y) was regressed on three known independent variables. Let $w_2^f = 1$, cs = 2, and $w_2^f \times cs = 3$, then three predictions of shape, Y_{p1}, Y_{p2}, and Y_{p3} can be extracted from equation 3.7. However, the $w_2^f \times cs$ shape effect was not significant and therefore not used in the analysis (but, it was still necessary to control for

its shape effect via equation 3.7). Table 3.1 shows the results of the MANCOVA (p-statistic < 0.05 implies significance).

Table 3.1. Results of equation 3.7 (MANCOVA).

Effects	p-statistic
1	0.0001
2	0.0001
3	0.1958

Two significant predictions of shape, Y_{p1} and Y_{p2}, followed by their resultant predicted variance-covariance matrices, H_1^Y and H_2^Y, were used in the Burnaby PCA approach:

$$H_1^Y = Y_{p1}^T Y_{p1} = U_{p1} \Lambda_{p1} U_{p1}^T \quad , \tag{3.8}$$

and

$$H_2^Y = Y_{p2}^T Y_{p2} = U_{p2} \Lambda_{p2} U_{p2}^T \quad , \tag{3.9}$$

where H_1^Y is the *26* x *26* predicted shape-by-w_2^f variance-covariance matrix and H_2^Y is the *26* x *26* predicted shape-by-cs variance-covariance matrix. The eigenvector describing the w_2^f shape effect is U_{p1}^T (*26* x *1*) and the eigenvector describing the cs shape effect is U_{p2}^T (*26* x *1*). The Burnaby PCA approach (equations 2.19 – 2.29) is used to remove the shared shape variances between effects so that the angle (θ) between each eigenvector is 90^o:

$$H_{\zeta 1}^Y = H_1^Y - (H_2^Y + H_3^Y) = U_{\zeta 1} \Lambda_{\zeta 1} U_{\zeta 1}^T \quad , \tag{3.10}$$

and

$$H_{\zeta 2}^Y = H_2^Y - (H_1^Y + H_3^Y) = U_{\zeta 2} \Lambda_{\zeta 2} U_{\zeta 2}^T \quad , \tag{3.11}$$

where $H^{Y}_{\zeta 1}$ is the *26* x *26* predicted shape-by- w^{f}_{2} variance-covariance matrix excluding shared variances from H^{Y}_{2} and $H^{Y}_{\zeta 2}$ is the *26* x *26* predicted shape-by-cs variance-covariance matrix excluding shared variances from H^{Y}_{1}. Then, Burnaby PC axes were calculated by pre-multiplying the original shape data Y to the eigenvectors of equations 3.10 and 3.11:

$$X^{Y}_{\zeta 1} = YU^{T}_{\zeta 1} \quad , \tag{3.12}$$

and

$$X^{Y}_{\zeta 2} = YU^{T}_{\zeta 2} \quad , \tag{3.13}$$

where $X^{Y}_{\zeta 1}$ is the *145* x *1* vector of Burnaby PC scores describing the w^{f}_{2} shape effect and $X^{Y}_{\zeta 2}$ is the *145* x *1* vector of Burnaby PC scores describing the cs shape effect. Both vectors were entered in tpsRegr as independent variables in order to visualize their effects on shape (figure 3.2).

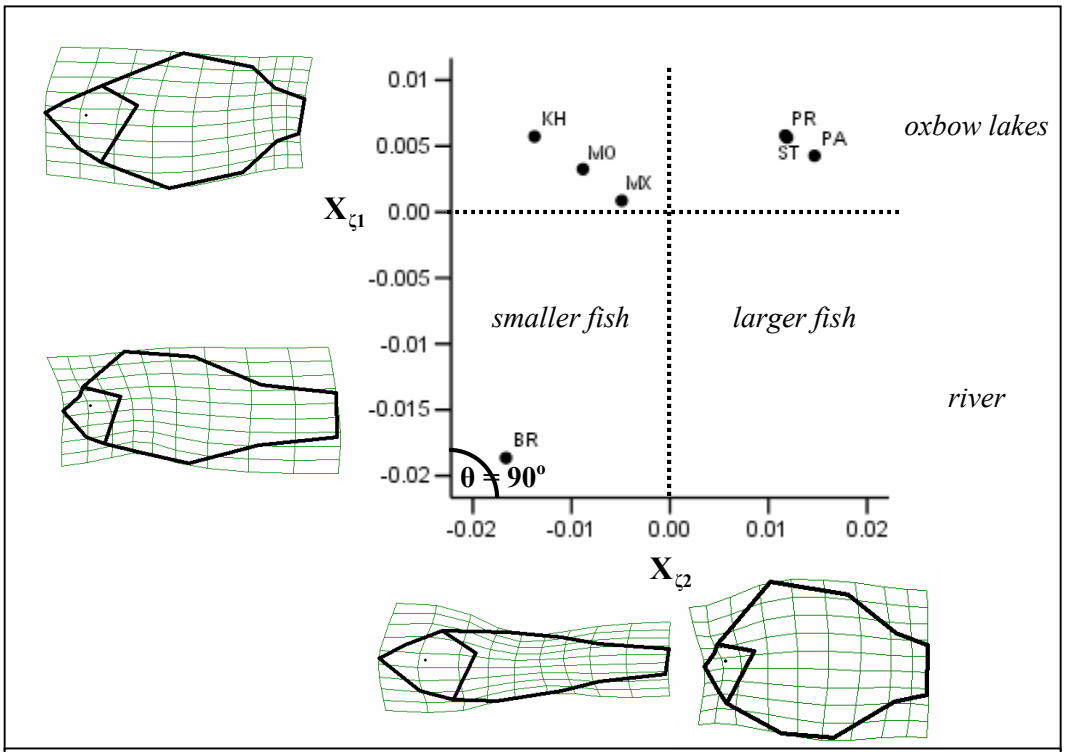

Figure 3.2. Thin-plate spline visualizations attributable to Burnaby PC scores describing the water flow (w_2^f) shape effect ($X_{\zeta 1}^Y$) and the allometric (CS) shape effect ($X_{\zeta 2}^Y$). $X_{\zeta 1}^Y$ accounted for 4.61% of total shape variance in Y; and $X_{\zeta 2}^Y$ accounted for 19.07% of total shape variance in Y. The degree of shared shape variance between $X_{\zeta 1}^Y$ and $X_{\zeta 2}^Y$ is 0° (=90° - 90°). The seven data points describing the shape effects along habitats are average (centroid) values of Burnaby PC scores. All visualizations have been magnified by 3x (tpsRegr).

Clearly, w_2^f contributes significantly to a shallow- and deep-bodied divergent shape axis of $X_{\zeta 1}^Y$, because bluegills from the river are more shallow-bodied than bluegills from the oxbow lakes (figure 3.3).

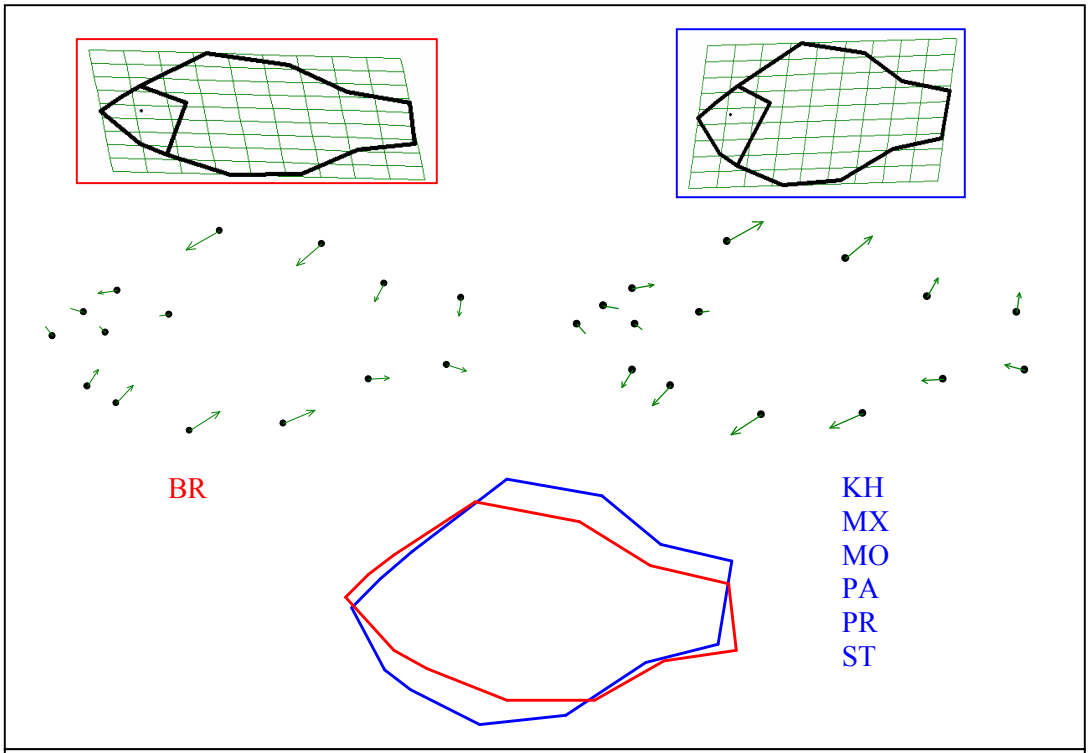

Figure 3.3. Uniform shape deformation of $X_{\zeta 1}^{Y}$. *Left*—shallow-bodied visualization; vector projections pointing inward (compression). *Right*—deep-bodied visualization; vector projections pointing outward (dilation). *Bottom*—overlay of uniform shape deformation of $X_{\zeta 2}$ (red ≡ shallow-bodied; blue ≡ deep-bodied).

According to fluid dynamic theory, river fish (BR datum point; figure 3.2) ought to have long and deep caudal peduncles allowing them to execute large powerful amplitude movements, thus making them efficient swimmers in the presence of water flow (Bainbridge, 1958, 1963; Newman, 1973; Newman and Wu, 1973; Yates, 1983; Fung, 1990). This shape deformation is characterized by the non-uniform components. The oxbow lake fish, on the other hand, have short caudal peduncles allowing them only to execute small amplitude movements, making them less efficient swimmers. Oxbow lake fish have deeper bodies perhaps making them more maneuverable than river fish and thus more efficient at using resources in the vegetation (Svanbäck and Eklöv, 2004).

The allometric shape effect ($X^{Y}_{\zeta 2}$) in bluegills can also be described as a shallow- and deep-bodied divergent shape generalization between small and large fish but is fairly different than $X^{Y}_{\zeta 1}$ with respect to the shape of head. According to fluid dynamic theory, the shape and motion of the front portion of the fish really do not matter very much in regard to thrust and swimming efficiency (Newman, 1973; Newman and Wu, 1973; Fung, 1990).

Diversification among oxbow lakes

Evaluating the shape differences in bluegills among oxbows, not individuals, is necessary in order to analyze the shape differences between oxbows. Water flow (w^{f}_{2}) was removed from this analysis. Hence, bluegill shape from the Brazos River was excluded from Y and a new generalized Procrustes analysis was performed:

$$Z \equiv \begin{array}{|l} \text{22 KH} \\ \text{10 MX} \\ \text{21 MO} \\ \text{27 PA} \\ \text{20 PR} \\ \text{23 ST} \\ \\ \end{array} \begin{array}{l} 26 \\ \\ \\ \\ \\ \\ 123 \end{array}$$

A multivariate multiple regression analysis is required to perform Burnaby PCA, where:

$$Z = f(\{\text{oxbows}\}, \{\text{cs}\}, \{\text{oxbows x cs}\}, \text{error}) \qquad (3.14)$$

Equation 3.14 defines the analytical model of a multivariate multiple regression analysis, where shape (Z) was regressed on three known independent variables. Let oxbows =1, cs = 2, and oxbows x cs = 3, then three predictions of shape, Z_{p1}, Z_{p2}, and Z_{p3} can be extracted from equation 3.14. All three shape effects were highly significant and therefore used in the analysis. Table 3.2 shows the results of the MANCOVA.

Table 3.2. Results of equation 3.14 (MANCOVA).

Effects	p-statistic
1	0.0001
2	0.0001
3	0.0001

Three significant predictions of shape, Z_{p1}, Z_{p2}, and Z_{p3}, followed by their resultant predicted variance-covariance matrices, H_1^Z, H_2^Z, and H_3^Z, were used in the Burnaby PCA approach:

$$H_1^Z = Z_{p1}^T Z_{p1} = V_1 \Lambda_1 V_1^T \quad , \tag{3.15}$$

$$H_2^Z = Z_{p2}^T Z_{p2} = V_2 \Lambda_2 V_2^T \quad , \tag{3.16}$$

and

$$H_3^Z = Z_{p3}^T Z_{p3} = V_3 \Lambda_3 V_3^T \quad , \tag{3.17}$$

where H_1^Z is the *26* x *26* predicted shape-by-oxbows variance-covariance matrix, H_2^Z is the *26* x *26* predicted shape-by-cs variance-covariance matrix, and H_3^Z is the *26* x *26* predicted shape-by-oxbows-x-cs variance-covariance matrix. The 5 eigenvectors describing the oxbows shape effect is V_{p1}^T (*26* x *5*), the eigenvector describing the cs shape effect is V_{p2}^T (*26* x *1*), and the 4 eigenvectors describing the oxbows x cs shape effect is V_{p3}^T (*26* x *4*). The Burnaby PCA approach is used to remove the shared shape variances between effects so that the θ between each eigenvector is 90^o:

$$H_{\zeta 1}^Z = H_1^Z - (H_2^Z + H_3^Z) = V_{\zeta 1} \Lambda_{\zeta 1} V_{\zeta 1}^T \quad , \tag{3.18}$$

$$H_{\zeta 2}^Z = H_2^Z - (H_1^Z + H_3^Z) = V_{\zeta 2} \Lambda_{\zeta 2} V_{\zeta 2}^T \quad , \tag{3.19}$$

and

$$H_{\zeta 3}^{Z} = H_{3}^{Z} - (H_{1}^{Z} + H_{2}^{Z}) = V_{\zeta 3} \Lambda_{\zeta 3} V_{\zeta 3}^{T} \quad , \tag{3.20}$$

where $H_{\zeta 1}^{Z}$ is the *26* x *26* predicted shape-by-oxbows variance-covariance matrix excluding shared variances from H_{2}^{Z} and H_{3}^{Z}, $H_{\zeta 2}^{Z}$ is the *26* x *26* predicted shape-by-cs variance-covariance matrix excluding shared variances from H_{1}^{Z} and H_{3}^{Z}, and $H_{\zeta 3}^{Z}$ is the *26* x *26* predicted shape-by- w_2 -x-cs variance-covariance matrix excluding shared variances from H_{1}^{Z} and H_{2}^{Z}. Then, Burnaby PC axes were calculated by pre-multiplying the original shape data Z to the eigenvectors of equations 3.18 – 3.20:

$$X_{\zeta 1}^{Z} = ZV_{\zeta 1}^{T} \quad , \tag{3.21}$$

$$X_{\zeta 2}^{Z} = ZV_{\zeta 2}^{T} \quad , \tag{3.22}$$

and

$$X_{\zeta 3}^{Z} = ZV_{\zeta 3}^{T} \quad , \tag{3.23}$$

where $X_{\zeta 1}^{Z}$ is the *123* x *5* matrix of Burnaby PC scores describing the oxbows shape effect, $X_{\zeta 2}^{Z}$ is the *123* x *1* vector of Burnaby PC scores describing the cs shape effect, and $X_{\zeta 3}^{Z}$ is the *123* x *4* matrix of Burnaby PC scores describing the oxbows x cs shape effect. All ten vectors (i.e., the *123* x *10* block) were entered in tpsRegr as independent variables in order to visualize their effects on shape (figure 3.4). The visualizations attributable to $X_{\zeta 2}^{Z}$ (equation 22) and $X_{\zeta 3}^{Z}$ (equation 3.23) are not shown in figure 3.4 because they are irrelevant to the analysis; but, they were still necessary for controlling the allometric effects on shape. The visualizations attributable to the third and fourth Burnaby PC axes of $X_{\zeta 1}^{Z}$ (i.e., $X_{\zeta 1}^{Z3}$ and $X_{\zeta 1}^{Z4}$) are shown in figure 3.4 because together they account for the highest shared shape variance with the shallow- and deep-bodied divergent shape axis of $X_{\zeta 1}^{Y}$. Also, Burnaby PC axes $X_{\zeta 1}^{Z3}$ and $X_{\zeta 1}^{Z4}$ are derived from

orthonormal eigenvectors because $V_{\zeta 1}^{T} V_{\zeta 1} = I$. So naturally, the degree of shared shape variance between $X_{\zeta 1}^{Z3}$ and $X_{\zeta 1}^{Z4}$ is 0^{o}.

To evaluate the degree of shared shape variance (= $\theta - 90^{o}$) between $X_{\zeta 1}^{Y}$ and $X_{\zeta 1}^{Z}$, equation 2.30 was used to determine the angle between the eigenvector of equation 3.10 and each of the five eigenvectors of equation 3.18 (Finney and Thomas, 1994):

$$\theta = \cos^{-1} \left\| U_{\zeta 1} \cdot V_{\zeta 1} \right\| , \tag{3.24}$$

where θ is equal to 100.32^{o}, 101.35^{o}, 108.44^{o}, 68.05^{o}, and 95.27^{o} corresponding to the angle between the first eigenvector of $U_{\zeta 1}$ and the first, second, third, fourth, and fifth eigenvectors of $V_{\zeta 1}$, respectively. The two eigenvectors of $V_{\zeta 1}$ that yields the highest degree of shared shape variance (=$\theta - 90^{o}$) are the third ($18.44^{o} = 108.44^{o} - 90^{o}$) and the fourth ($-21.95^{o} = 65.05^{o} - 90^{o}$) eigenvectors. Therefore, the visualizations attributable to the third and forth Burnaby PC axes of $X_{\zeta 1}^{Z}$ (i.e., $X_{\zeta 1}^{Z3}$ and $X_{\zeta 1}^{Z4}$) are *relatively* similar to the visualizations attributable to $X_{\zeta 1}^{Y}$. The fourth Burnaby PC axis ($X_{\zeta 1}^{Z4}$) shares more shape variance than $X_{\zeta 1}^{Z3}$. Therefore, the uniform shape deformation of $X_{\zeta 1}^{Z4}$ should be evaluated.

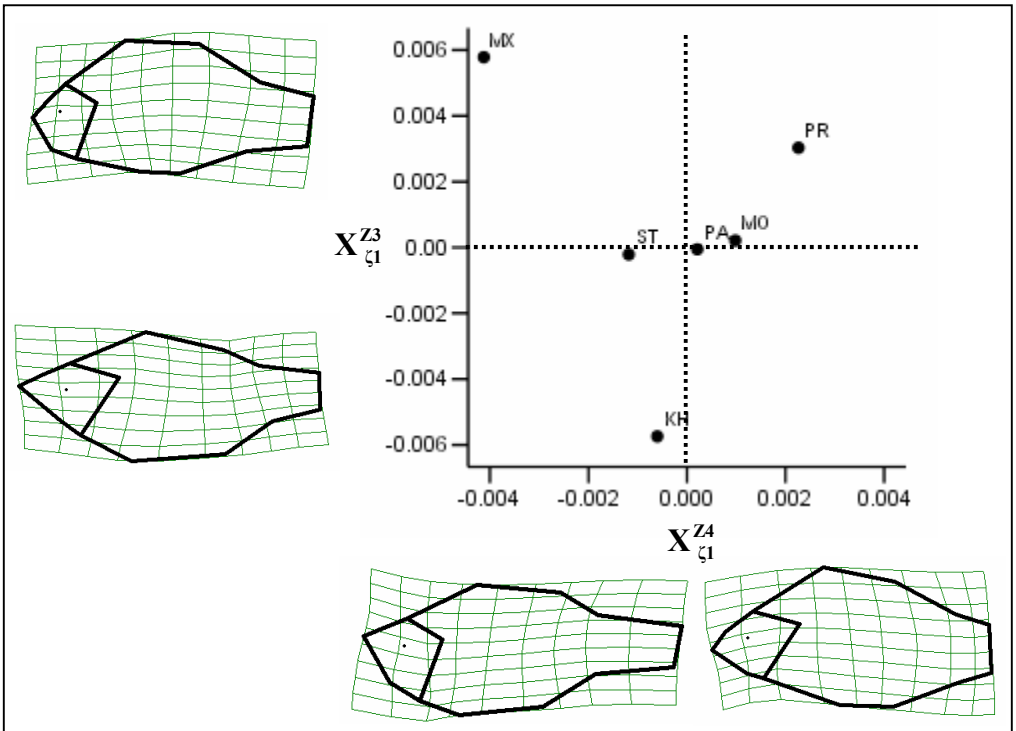

Figure 3.4. Thin-plate spline visualizations attributable to Burnaby PC scores describing the third oxbow shape effect ($X^{Z3}_{\zeta 1}$) and the forth oxbow shape effect ($X^{Z4}_{\zeta 1}$). $X^{Z3}_{\zeta 1}$ accounted for 8.96% of total shape variance in Z_{p1} and 0.63% of total shape variance in Z; and $X^{Z4}_{\zeta 1}$ accounted for 3.38% of total shape variance in Z_{p1} and 0.24% of total shape variance in Z. The degree of shared shape variance between $X^{Z3}_{\zeta 1}$ and $X^{Z4}_{\zeta 1}$ is 0^{o} ($=90^{o} - 90^{o}$). The six data points describing the shape effects along oxbows are centroid values of Burnaby PC scores. All visualizations have been magnified by 3x (tpsRegr).

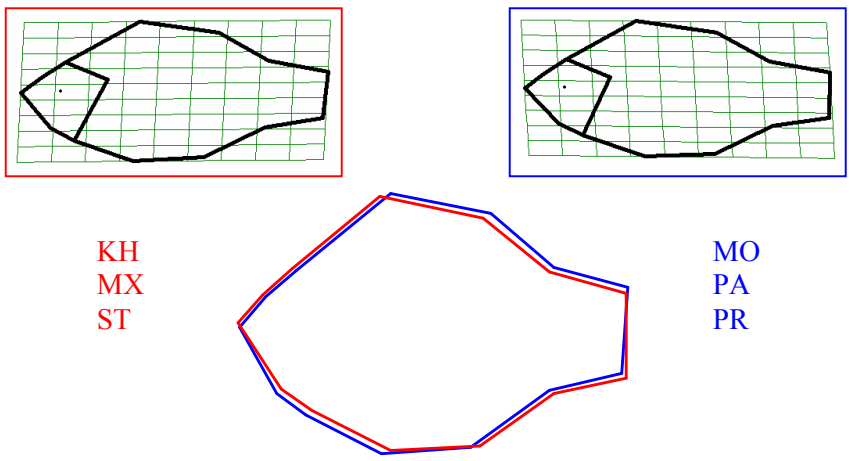

Figure 3.5. Uniform shape deformation of $X^{Z4}_{\zeta 1}$. *Left*—uniform shape deformation of a slight shearing effect. *Right*—uniform shape deformation of a slight shearing effect. *Bottom*—overlay of uniform shape deformation of $X^{Z4}_{\zeta 1}$.

Diversification of body shape in bluegills

Three descriptive analyses (all using the Burnaby PCA approach; see chapter II) of body shape diversification have been done: (1) shared features of shape diversification in three species of sunfish between river and oxbow lake habitats (figure 2.9); (2) body shape divergence in bluegill between river and six oxbow lakes (figure 3.2); and (3) body shape divergence in bluegill among six oxbow lakes (figure 3.4). The first two descriptive analyses show a clear shallow- and deep-bodied divergent shape generalization but the third one does not (see figure 3.5). There are similarities between the shape axes of $X^{Y}_{\zeta 1}$ (figure 3.2) and $X^{Z4}_{\zeta 1}$ (figure 3.4). For instance, the shape of the caudal peduncle between these two axes of shape divergence is very similar; and, it was mentioned that long and deep caudal peduncles allow fish to execute large powerful amplitude movements thus making them efficient swimmers (Bainbridge, 1958, 1963; Newman, 1973; Newman and Wu, 1973; Yates, 1983; Fung, 1990). So although the $X^{Z4}_{\zeta 1}$ axis does not describe a shallow- and deep-bodied divergent shape generalization

(i.e., a uniform shape effect), it does describe a non-uniform shape effect that parallels the non-uniform shape effect of $X_{\zeta 1}^{Y}$.

So far, I have discussed water flow (w_2^f) as the main extrinsic factor driving a shallow- and deep-bodied divergent shape generalization in bluegills. I have yet to discuss the mechanism by which diversification ensues—that is, divergent natural selection (or fitness trade-offs); a fitness gain for a particular body shape in one environment is a fitness loss for that body shape in the alternative environment. There is a potential fitness trade-off between aerobic swimming efficiency (≡ stability) and metabolic maintenance (≡ standard metabolic rate) with respect to the $X_{\zeta 1}^{Y}$ divergent shape axis (between $w_2^f = 0$ and $w_2^f \neq 0$) because swimming efficiency is a fitness component (Priede, 1985; Plaut, 2001) and standard metabolic rate is a surrogate component of fitness (Pettersson and Hedenström, 2000).

Figure 3.6 illustrates the river-oxbow (shallow- and deep-bodied) shape effect and the potential physiological and hydromechanical consequences associated with the effect. Subsequently, the last empirical analysis (chapter VI) is to evaluate standard metabolic rates and aerobic swimming efficiencies in bluegills from river (flowing water; $w_2^f \neq 0$) and oxbow lake (still-water; $w_2^f = 0$) habitats in order to investigate a potential trade-off between the metabolic response due to the environment and the hydrodynamic response due to swimming.

River Bluegill – *flowing water*
shallow-bodied
high maintenance cost (metabolic response due to the environment)
low maneuverability/high stability (hydrodynamic response due to swimming)

Oxbow Lake Bluegill – *still water*
deep-bodied
low maintenance cost (metabolic response due to the environment)
high maneuverability/low stability (hydrodynamic response due to swimming)

Figure 3.6. Bluegill river-oxbow shape effect and potential metabolic and hydrodynamic consequences associated with the effect.

CHAPTER IV
ON THE HYDRODYNAMICS-BASED POWER FUNCTION

How can it be that mathematics, a product of human thought independent of experience, is so admirably adapted to the objects of reality?

— Albert Einstein (1879–1955)

Introduction

To evaluate the aerobic swimming efficiency in fishes, it is imperative to evaluate hydrodynamic drag (resistance). However, direct measurement of hydrodynamic resistance (F_d; see equation 3.5) is very difficult because it requires complex measurements of several hydromechanical factors (Fung, 1990). Therefore, engineers and physiologists often take an alternative approach, that is, measuring the fish's total oxygen consumption rate with respect to swimming speed; because the expenditure of energy during swimming, or the metabolic transport rate (MTR), is reflected in the rate of change in oxygen consumption over the change in swimming speed.

Two models are used to derive standard metabolic rate (SMR) and MTR in fishes: the traditional exponential function (TEF; equation 4.1) and the hydrodynamics-based power function (HPF; equation 4.2). Interpretation, use, and analytical derivation of the parameters of the HPF vary in the literature leading to arbitrary or traditional choice of methods to estimate SMR and inaccurate estimates of MTR. To understand these effects, I address the distinction of the parameters between the two models and then describe the analytical derivation of the parameters of the HPF. Once the issues and parameters are presented, I propose a two-step solution that will ensure appropriate use of the HPF to evaluate SMR and MTR in fishes.

The first model is the TEF (Brett, 1964; Webb, 1975; Beamish, 1978):

$$\left(\frac{M}{a_e}\right) = f(U) = e^{b_e U} + \varepsilon \tag{4.1}$$

and the second model is the HPF (Wu, 1977; Videler, 1993):

$$(M - a_p) = f(U) = \mu U^{b_p} + \varepsilon \ , \tag{4.2}$$

where dependent variable M is the total metabolic (oxygen consumption) rate measured during sustained swimming, independent variable U is the measured sustained swimming speed, constant $a_{(e,p)}$ is the SMR evaluated at U = 0, constant $b_{(e,p)}$ is the MTR, constant μ is the standard cost of swimming (SCOS) evaluated at U =1, and variable ε is measurement error. The increment cost of swimming (ICOS) is a compound variable, which in equation 1 is depicted as $ICOS_e$ (= M over a_e) and in equation 2 is depicted as $ICOS_p$ (= M minus a_p). The $ICOS_p$ is referred to as the net cost of swimming (Korsmeyer et al., 2002), but I recommend using the former lexis because of its generality. The MTR contains information on aerobic swimming efficiency, which is an inverse measure of the exponential change in ICOS with respect to U (Webb, 1993; Wardle et al., 1996; Ohlberger et al., 2006). The SCOS contains information on aerobic swimming capacity, which is a measure of metabolic power (Fung, 1990). Subscripts e and p denote the TEF and the HPF, respectively. See Appendix A for a comprehensive listing of the parameters of the TEF and the HPF.

The parameters of equations 4.1 and 4.2 are commonly misinterpreted in the literature, especially for a_e and a_p. For instance, there can only be one best estimate of SMR per fish even though there are two different analytical derivations of SMR—one from the TEF (a_e) and the other from the HPF (a_p)—which yield different values (Gordon et al., 1989). Thus, a_e is not equal to a_p, which can be shown by evaluating the absolute minimum value of equations 4.1 and 4.2 at the endpoint U = 0. The SMR,

which is the M-intercept, is defined at (not equal to) the absolute minimum value of equations 4.1 and 4.2. The first derivative of M with respect to U is calculated and then evaluated at the endpoint U = 0 in order to determine the absolute minimum value of equations 4.1 and 4.2 (Finny and Thomas, 1994). The results are as follows: the absolute minimum value of equation 4.1 is $a_e b_e > 0$, taken on at the endpoint U = 0; the absolute minimum value of equation 4.2 is 0, taken on at the endpoint U = 0. Therefore, a_e is not equal to a_p because the absolute minimum value of equation 4.1 (i.e., $a_e b_e > 0$) is not defined at the absolute minimum value of equation 4.2 (i.e., 0). In other words, a_e is not equal to a_p because they are derived from two different models that have distinct mathematical properties. The only condition in which the value of a_e converges to the value of a_p is when b_e approaches 0 (i.e., $a_e b_e$ approaches 0). However, this condition implies that the values of M converge to the value of $a_e = a_p$ for all values of U, which is nonsense because SMR (a constant evaluated at U = 0) cannot vary as a function of U.

Videler and Nolet (1990) have also indicated that a_e is not equal to a_p but used a different method to arrive at a similar conclusion, that is, a_p is greater than a_e because iterative least-squares regression (albeit, a parameter estimation method) with the HPF sets more weight on the higher U values (Korsmeyer et al., 2002). So, which value of SMR (a_e or a_p) should be used? The answer depends on which function best predicts $M = f(U)$, which typically would be considered the function yielding the lowest sum of squared residuals. Usually, but not always, the TEF best predicts $M = f(U)$ in fishes (Webb, 1975). However, even if the TEF best predicts $M = f(U)$, a_e should not be substituted for a_p to derive b_p and μ because a_e is not equal to a_p. Hence, using a_e in substitution for a_p results in inaccurate estimates of b_p and μ. Also, using estimates of SMR from static respirometry in substitution for a_p generally results in inaccurate values of b_p and μ; estimates of SMR from static respirometry deviate (sometimes greatly) from analytical estimates of SMR due to the nature of ε inherent with $M = f(U)$. For instance, analytical estimates of SMR can be affected by a variety of factors such as increased Ms at low Us due to excitement of the fish and decreased Ms at high Us due to anaerobic metabolism supplementing aerobic metabolism (Brett, 1964). Therefore, substituting a

value not equal to a_p for a_p misrepresents the data and therefore results in inaccurate values of b_p and μ. This is an important point because it is tempting to substitute estimates of SMR from static respirometry or a_e for a_p in order to derive easily and inaccurately b_p and μ as some investigators (e.g., Korsmeyer et al., 2002) have done. It should be noted that either of the two estimates of SMR is acceptable depending on which of the two models best predicts $M = f(U)$. The only constraint, however, is that a_e and a_p are used alongside their conjugate ICOS function. For instance, the conjugate of a_e is $ICOS_e$ (equation 4.1); whereas, the conjugate of a_p is $ICOS_p$ (equation 4.2). Thus, the best approach to estimating SMR, b_p and μ is a two-step process, where step 1 is to choose the best estimator of SMR (figure 4.1a) and step 2 involves deriving b_p and μ without substituting estimates of SMR from static respirometry or a_e for a_p (figure 4.1b).

The distinction between a_e and a_p, b_e and b_p, b_p and μ, and $ICOS_e$ and $ICOS_p$ is addressed to ensure that the parameters of the HPF are interpreted and used properly—this comprises the conceptual framework for using the HPF. The analytical derivation of the constants of the HPF (i.e., a_p, b_p, and μ) is also addressed to ensure that they are derived correctly and robustly—this comprises the mathematical framework for using the HPF. Together, the conceptual and mathematical frameworks for using the HPF will ensure appropriate interpretation, use, and analytical derivation of a_p, b_p, and μ.

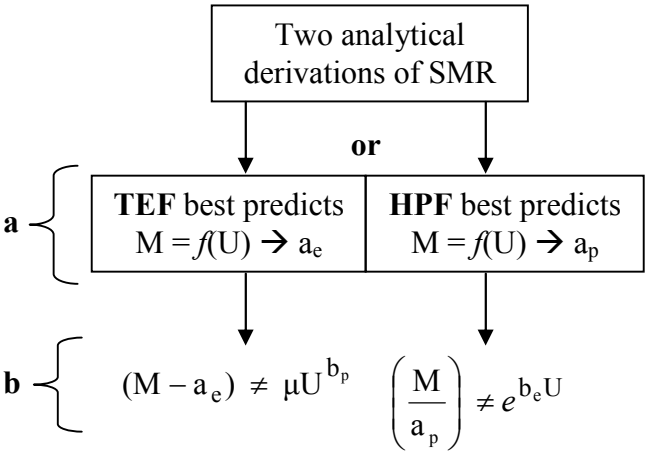

Figure 4.1. A two-step procedure to determine the best value of an analytically-derived estimate of SMR. (**a**)—step 1; only one best value of an analytically-derived estimate of SMR (a_e or a_p) can be evaluated from $M = f(U)$. (**b**)—step 2; the conjugates of a_e and a_p are not $ICOS_p$ and $ICOS_e$, respectively.

Conceptual framework

Distinction between a_e and a_p – The SMR derived from the TEF (a_e) is not equal to the SMR derived from the HPF (a_p). Therefore, the function that yields the lowest sum of squared residuals for $M = f(U)$ is the model that should be used to derive an analytical estimate of SMR, which best approximates the actual SMR (figure 4.1a). Thus, only one best value of an analytically-derived estimate of SMR (a_e or a_p) can be evaluated from $M = f(U)$. One of the main recommendations of this paper is that investigators use neither a_e or a_p without testing the other. Both models must be fitted to $M = f(U)$ in order to confirm which of the two models best explains the data. Only then can a_e or a_p be verified as the best value of an analytically-derived estimate of SMR.

Distinction between b_e and b_p – The MTR derived from the TEF (b_e) can only be used for comparisons of aerobic swimming efficiency among individuals of similar SMRs because b_e is dependent on a_e (Korsmeyer and Dewar, 2001; Korsmeyer et al.,

2002); whereas, the MTR derived from the HPF (b_p) can be used for comparisons of aerobic swimming efficiency among individuals of different SMRs because b_p takes into account differences in a_p (Korsmeyer et al., 2002). In this way, b_p is less limited and more versatile than b_e. The MTR (b_p) will always represent a valid estimate of aerobic swimming efficiency even if the TEF best predicts $M = f(U)$. It should be noted that both models are used to derive MTR, but b_e and b_p represent different mathematical components of aerobic swimming efficiency—b_e is dependent on a_e; whereas, b_p is independent of a_p. Therefore, the HPF is the most appropriate model to evaluate aerobic swimming efficiency in fishes (Korsmeyer et al., 2002).

Distinction between b_p and μ – The MTR (b_p) contains information on the aerobic swimming efficiency (Webb, 1993; Wardle et al., 1996; Ohlbereger et al., 2006); whereas, the SCOS (μ) contains information on the aerobic swimming capacity, and efficiency and capacity are distinct concepts even though they can be mathematically correlated. Unfortunately, the distinction between b_p and μ has not been highlighted in the literature. Some investigators (Wardle et al., 1996) have claimed that both b_p and μ contain information on aerobic swimming efficiency. This is incorrect because b_p and μ do not share the same units of measurement. The MTR (b_p) represents the slope of the logarithm-transformed (*ln*) linear form of the $ICOS_p$, whereas the SCOS (μ) represents the intercept of the *ln* linear form of the $ICOS_p$. The units of μ equal the units of metabolic rate, or more specifically the units of $ICOS_p$, which is a measure of metabolic power (Fung, 1990) or metabolic capacity. Hence, the MTR (b_p) represents the exponential change in metabolic capacity with respect to U; whereas, the SCOS (μ) represents the standard metabolic capacity for all Us.

Distinction between $ICOS_e$ and $ICOS_p$ – The $ICOS_e$ is not a measure of metabolic capacity and does not follow standard hydrodynamic laws because it is dimensionless (i.e., the measurement units cancel due to appearance in both numerator and denominator). Hence, the MTR derived from the TEF (b_e) is relative to a_e. In other words, fish that have a similar $ICOS_e$ but have a different a_e will have a different b_e (Korsmeyer and Dewar, 2001; Korsmeyer et al., 2002). The $ICOS_p$, on the other hand, is

a measure of metabolic capacity and does follow standard hydrodynamic laws. Thus, fish that have a similar $ICOS_p$ but have a different a_p will have a similar b_p (Korsmeyer et al., 2002).

Mathematical framework

Analytical derivation of b_p and μ – The MTR (b_p) and the SCOS (μ) cannot be predicted accurately if a_e is substituted for a_p even if the TEF best predicts $M = f(U)$ because the conjugate of a_e is not $ICOS_p$ (figure 4.1b). Therefore, substituting a_e for a_p to derive b_p and μ is mathematically inappropriate. Yet, it is not even necessary to determine the SMR in order to determine b_p and μ. Following is an analytical derivation of b_p and μ from the HPF, which shows that a_p is not necessary when the preferred analysis is predicated on determination of b_p and μ. It is important to note that although maximum likelihood parameter estimation (MLPE) can be used to derive a_p, b_p, and μ simultaneously (Wardle et al., 1996), it fails to evaluate b_p and μ when the best estimate of a_p is greater than at least one of the values of M because any negative value of $ICOS_p$ is not mathematically permitted in a power function. This problem occurs when outliers are present in $M = f(U)$. Therefore, the objective of the following formulations is to derive b_p and μ without having to calculate a_p (equations 4.3 – 4.6) and to correct for negative values of differential $ICOS_p$ (equations 4.7 – 4.9) that are likely to occur due to outliers in $M = f(U)$.

Rearrange equation 4.2 such that variable M is a function of variable U and constants a_p, b_p and μ:

$$M = f(U) = a_p + \mu U^{b_p} , \tag{4.3}$$

then calculate the derivative of M with respect to U, which sets $a_p = 0$ because the SMR is not dependent on U. Thus, differentiation of equation 4.3 with respect to U yields the following expression:

$$\frac{d\mathrm{M}}{d\mathrm{U}} = \mu\, \mathrm{b_p}\, \mathrm{U}^{(\mathrm{b_p}\,-1)} \tag{4.4}$$

and its *ln* linear form:

$$ln\left(\frac{d\mathrm{M}}{d\mathrm{U}}\right) = [ln(\mu) + ln(\mathrm{b_p})] \;+\; (\mathrm{b_p} - 1)\, ln(\mathrm{U}) \;, \tag{4.5}$$

which can be expressed as:

$$ln\left(\frac{d\mathrm{M}}{d\mathrm{U}}\right) = \alpha_0 \;+\; \alpha_1\, ln(\mathrm{U}) \quad , \tag{4.6}$$

where $\mathrm{b_p} = \alpha_1 + 1$ and $\mu = e^{[\alpha_0 - ln(\mathrm{b_p})]}$. Equation 4.6 follows standard hydrodynamic laws, where the logarithm of the differential of M (dM) over the differential of U (dU), or the logarithm of the differential of energy cost of transport (ΔECOT) is linearly related to the logarithm of U. The values of ΔECOT have to be positive but due to measurement error (ε) the values could be negative, which is not permitted in a power function. Therefore, equation 4.4 should be squared to ensure that negative values become positive. Below is the result of squaring equation 4.4:

$$\left(\frac{d\mathrm{M}}{d\mathrm{U}}\right)^2 = \mu^2\, \mathrm{b_p^2}\, \mathrm{U}^{(2\mathrm{b_p}\,-2)} \tag{4.7}$$

and its *ln* linear form:

$$ln\left(\frac{d\mathrm{M}}{d\mathrm{U}}\right)^2 = [2ln(\mu) + 2ln(\mathrm{b_p})] \;+\; (2\mathrm{b_p} - 2)\, ln(\mathrm{U}) \;, \tag{4.8}$$

which can be expressed as:

$$ln\left(\frac{d\mathrm{M}}{d\mathrm{U}}\right)^{2} = \beta_0 + \beta_1\, ln(\mathrm{U}) \quad , \tag{4.9}$$

where $b_p = \frac{1}{2}\beta_1 + 1$ and $\mu = e^{[\frac{1}{2}\beta_0 - ln(b_p)]}$. Equation 4.9 also follows standard hydrodynamic laws. The derivative of M with respect to U (equations 4.4 and 4.7) augments measurement error (ε), which can lead to the production of outliers that may affect estimation accuracy of the parameters of the HPF. Although one must make every effort to reduce experimental design-induced variation in respirometric results (see Steffenson, 1989, for an excellent review of techniques), one always has to cope with variability in such data. Robust parametric and non-parametric regression methods (see Hussain and Sprent, 2000, for a description of methods) and MLPE can be used to mathematically cope with slight to moderate ε (standard deviations < 0.1). Large ε (standard deviations ≥ 0.1), on the other hand, can significantly affect the accuracy of the parameters of the HPF even when MLPE or robust regression methods are employed (A. Papadopoulos, T.J. DeWitt, and W.H. Neill, unpublished).

Analytical derivation of a_p – The analytical derivation of the SMR has become common practice in the field of fish respirometry because of its simplicity over direct experimental approaches. The analytical derivation of the SMR from the HPF (a_p) has not been reported in the literature, and its derivation may prove to be valuable in statistical analyses, where b_p and μ are used conjointly. It is necessary to derive a_p along with b_p and μ in order to predict $M = f(U)$. The idea here is to determine which of the two models (TEF or HPF) best predicts $M = f(U)$ in order to evaluate which derived value of SMR (a_e or a_p) best approximates the actual SMR. For this reason the analytical derivation of a_p is important and necessary. Polynomial regression can be used to derive a_p accurately; if by letting $X_i = U^{b_p}$ and $Y_i = M$, then:

$$a_p = \frac{\left(\sum_{i=1}^{n} X_i^2\right)\left(\sum_{i=1}^{n} Y_i\right) - \left(\sum_{i=1}^{n} X_i\right)\left(\sum_{i=1}^{n} X_i Y_i\right)}{\left(\sum_{i=1}^{n} i - \sum_{i=0}^{n-1} i\right)\left(\sum_{i=1}^{n} X_i^2\right) - \left(\sum_{i=1}^{n} X_i\right)^2} \tag{4.10}$$

and its matrix form:

$$\begin{bmatrix} a_p \\ \mu \end{bmatrix} = \begin{bmatrix} \sum_{i=1}^{n} i - \sum_{i=0}^{n-1} i & \sum_{i=1}^{n} X_i \\ \sum_{i=1}^{n} X_i & \sum_{i=1}^{n} X_i^2 \end{bmatrix}^{-1} \begin{bmatrix} \sum_{i=1}^{n} Y_i \\ \sum_{i=1}^{n} X_i Y_i \end{bmatrix}, \tag{4.11}$$

where n is the total number of measurements of $M = f(U)$. Equation 4.10 or 4.11 is limited in that the accuracy of the value of a_p is constrained to a polynomial regression analysis. If outliers are suspected in $M = f(U)$, then robust parametric or non-parametric linear regression methods can be used with equation 4.6 or 4.9 to reduce the sum of squared residuals. This will ensure a robust estimate of b_p, which in turn increases the accuracy of estimation for a_p. Ideally, however, a_p should be evaluated using the same parameter estimation method used to evaluate b_p and μ in order to maintain symmetry. For example, if one chooses to evaluate b_p and μ using the complete Theil's method (a robust non-parametric linear regression method), then this method should also be used to evaluate a_p. Also, when outliers are present in $M = f(U)$, using equation 4.10 or 4.11 (i.e., polynomial regression analysis) to derive a_p is unacceptable because polynomials tend to fluctuate highly between outliers. One way to correct this problem is to transform the model into linear form, where robust linear regression methods can be used to correct for

outliers. Therefore, I have developed a calculus-based method using integration for deriving, in linear form, a_p. The SMR (a_p) can be analytically-derived from the HPF (equation 3) via integration:

$$\int_{U_1}^{U_n} M\, dU = \int_{U_1}^{U_n} a_p\, dU + \int_{U_1}^{U_n} \mu U^{b_p}\, dU \quad , \tag{4.12}$$

where U_1 is the initial or 1st value of U, and U_n is the last or n^{th} value of U. Rearrange equation 4.12:

$$\int_{U_1}^{U_n} M\, dU - \int_{U_1}^{U_n} \mu U^{b_p}\, dU = \int_{U_1}^{U_n} a_p\, dU \tag{4.13}$$

and then equate the first term on the left side of equation 4.13 to a polynomial function of 3rd order. A 3rd order polynomial function is optimal for this system because, according to Videler and Nolet (1990), the highest value of b_p known for fishes is 3.0. Then, integrate each of the three terms in equation 4.13 with respect to U, which yields the linear function:

$$\left[\sum_{i=1}^{3} \frac{\lambda_i U^{i+1}}{i+1}\right]_{U_1}^{U_n} - \left[\frac{\mu U^{b_p+1}}{b_p+1}\right]_{U_1}^{U_n} = \left[a_p U\right]_{U_1}^{U_n} + C \quad , \tag{3.14}$$

where λ_i are the i^{th} polynomial regression coefficients and the slope of equation 3.14 is the robust value of a_p; regressing the left side of equation 3.14 on U yields the linear estimate of the slope equal to a_p and an intercept value equal to constant *C*. Therefore, an accurate and precise value of a_p can always be attained when using equations 4.13 or 4.14.

In conclusion, the appropriate analytical estimate of SMR to report should be derived from the model that best predicts respirometric data (figure 4.1a). The SMR derived from the TEF (a_e) is not equal to the SMR derived from the HPF (a_p), which implies that the conjugates of a_e and a_p are not $ICOS_p$ and $ICOS_e$, respectively (figure 4.1b). Hence, substituting a_e for a_p to derive b_p and μ is mathematically inappropriate and should be avoided. The MTR derived from the HPF (b_p) should be used for comparisons of aerobic swimming efficiency among species with different SMRs because b_p is not dependent on a_p (Korsmeyer et al., 2002). Since SMR is independent of b_p and μ, I have provided a means to calculate b_p and μ without first estimating SMR (equations 4.3 – 4.9). Also, I have provided a method to correct for negative values of $ICOS_p$, which may occur due to outliers in $M = f(U)$, in order to evaluate b_p and μ (equations 4.7 – 4.9). The SCOS (μ), which is derived from equations 4.3 – 4.9, can be used for comparisons of aerobic swimming capacity among individuals. The SMR derived from the HPF (a_p) can be determined accurately from equations 4.10 or 4.11 as long as there are no outliers in $M = f(U)$. If outliers are suspected, then a_p derived from equations 4.13 or 4.14 is more accurate and precise than a_p derived from equations 4.10 or 4.11.

CHAPTER V
ON A UNIFIED MODEL OF ACTIVE RESPIROMETRY

> *I have resolved to quit only abstract geometry, that is to say, the consideration of questions which serve only to exercise the mind, and this, in order to study another kind of geometry, which has for its objects the explanation of the phenomena of nature.*
>
> — René Descartes (1596–1650)

Introduction

In chapter IV, I compared and contrasted the parameters of the traditional exponential function (TEF) with the parameters of the hydrodynamics-based power function (HPF). Both models attempt to describe the relationship between total metabolic rate (M) and swimming speed (U). Also, both models are used to derive different values of standard metabolic rate (SMR) for the same fish. This is a contradiction—how can it be that these two models yield different values of SMR when both share M? I partially answered this question in chapter IV—that is, the model that best explains respirometric data is the function that yields the best estimate of SMR. I have yet to explain, however, how this phenomenon relates to fish. In other words, the fact that there are differences in SMRs among fish of the same species is an issue of high interest; but, the fact that there are differences in the models that describe the relationship between M and U among fish of the same species is an unprecedented phenomenon. Is it possible that the difference in SMR between the two models is based on a conditional parameter that characterizes yet another model of active respirometry? Is it possible that there exists a unified model of active respirometry? In this short chapter, I devise a unified model of active respirometry based on three classes of transcendental functions describing $M = f(U)$; they are the exponential (equation 4.1), power (equation 4.2), and polynomial (equation 4.3) functions.

The concept of even and odd functions

Many of the functions in science are inverses of one another. Perhaps, the most famous inverse-pair is the exponential (*e*) and logarithmic functions (e.g., the TEF; equation 4.1). Less commonly known, however, are the hyperbolic functions and their inverses—functions that arise in the study of heat, friction (Finney and Thomas, 1994), and, as I will show, respirometry.

Every function defined on an interval centered at the origin can be expressed in a unique way, that is, as the sum of one even function (Φ_f) and one odd function (Θ_f) (Finney and Thomas, 1994). I refer to this characterization of functions as the even-odd decomposition, which is:

$$\mathrm{M} = f(\mathrm{U}) = \Phi_f(\mathrm{U}) + \Theta_f(\mathrm{U}) = \left(\frac{f(\mathrm{U}) + f(-\mathrm{U})}{2}\right) + \left(\frac{f(\mathrm{U}) - f(-\mathrm{U})}{2}\right) \qquad (5.1)$$

Using standard arithmetic, it is easy to determine that equation 1 is in fact equal to M = *f*(U). Then, the even-odd decomposition of the TEF (equation 4.1) is:

$$\mathrm{M} = f(\mathrm{U}) = \mathrm{a_e} e^{\mathrm{b_e U}} = \left(\frac{\mathrm{a_e} e^{\mathrm{b_e U}} + \mathrm{a_e} e^{-\mathrm{b_e U}}}{2}\right) + \left(\frac{\mathrm{a_e} e^{\mathrm{b_e U}} - \mathrm{a_e} e^{-\mathrm{b_e U}}}{2}\right) , \qquad (5.2)$$

where a_e is the SMR, b_e is the metabolic transport rate (MTR), Φ_f is:

$$\Phi_f(\mathrm{U}) = \left(\frac{\mathrm{a_e} e^{\mathrm{b_e U}} + \mathrm{a_e} e^{-\mathrm{b_e U}}}{2}\right) = \mathrm{a_e} cosh(\mathrm{b_e U}) \quad , \qquad (5.3)$$

and Θ_f is:

$$\Theta_f(\mathrm{U}) = \left(\frac{\mathrm{a_e} e^{\mathrm{b_e U}} - \mathrm{a_e} e^{-\mathrm{b_e U}}}{2}\right) = \mathrm{a_e} sinh(\mathrm{b_e U}) \qquad (5.4)$$

The even and odd parts of the function e^{U} are known as the hyperbolic cosine (denoted *cosh*) and hyperbolic sine (denoted *sinh*) functions of U, respectively (Finney and

Thomas, 1994). Therefore, the TEF (equation 4.1) can be expressed as the sum of *cosh* and *sinh* of U:

$$M = f(U) = a_e e^{b_e U} = a_e cosh(b_e U) + a_e sinh(b_e U) \quad (5.5)$$

Equation 5.5 is an important characterization of the TEF, because in this form it can be related to the HPF. The even-odd decomposition of the HPF (equation 4.3) is:

$$M = f(U) = a_p + \mu U^{b_p} = \left(\frac{(a_p + \mu U^{b_p}) + (a_p - \mu U^{b_p})}{2} \right) + \left(\frac{(a_p + \mu U^{b_p}) - (a_p - \mu U^{b_p})}{2} \right), \quad (5.6)$$

where a_p is the SMR, b_p is the MTR, μ is the standard cost of swimming (SCOS), Φ_f is:

$$\Phi_f(U) = \left(\frac{(a_p + \mu U^{b_p}) + (a_p - \mu U^{b_p})}{2} \right) = a_p \quad , \quad (5.7)$$

and Θ_f is:

$$\Theta_f(U) = \left(\frac{(a_p + \mu U^{b_p}) - (a_p - \mu U^{b_p})}{2} \right) = \mu U^{b_p} \quad (5.8)$$

The even part of the HPF (equation 5.7) collapses to a point, that is, the value of a_p. The odd part of the HPF (equation 5.8) describes the power function, μU^{b_p}.

At this stage, it is easy to determine how equation 5.3 is related to equation 5.7, and how equation 5.4 is related to equation 5.8. In chapter IV, I described analytically how the values of SMR between the two models converged, that is, when b_e approaches zero (or stated mathematically, $b_e \rightarrow 0$). This condition is imposed in order for equations 5.3 and 5.7 to converge to a shared value of SMR (a). If $b_e \rightarrow 0$, then $a_e = a_p = a$, because $cosh(b_e U \rightarrow 0) \cong 1$. Hence, equation 5.7 can also be expressed equivalently as equation 5.3, with the condition that $b_e \rightarrow 0$ is imposed. This is one part of the unified model completed. What about the relationship between equations 5.4 and 5.8? If by letting the a_e term in equation 5.4 take the value β, then there exists a solution such that β

multiplied to b_e equals μ, when $b_e \rightarrow 0$; and, if by placing a power term b_p of U in equations 5.3 and 5.4, then equations 5.3, 5.4, 5.7, and 5.8 converge to the following unified expression:

$$M = f(U) = \left(\frac{a e^{b_e U^{bp}} + a e^{-b_e U^{bp}}}{2} \right) + \left(\frac{\beta e^{b_e U^{bp}} - \beta e^{-b_e U^{bp}}}{2} \right) \qquad (5.9)$$

Equation 5.9 equals the TEF (equation 4.1) when $a = \beta$, $b_p = 1$, and $b_e > 0$; and equation 5.9 equals the HPF (equation 4.3) when $\mu = \beta b_e$, $b_p > 1$, and $b_e \rightarrow 0$. Therefore, equation 5.9 can be simplified to include the hyperbolic functions, *cosh* and *sinh*:

$$M = f(U) = a\, cosh(b_e U^{b_p}) + \beta\, sinh(b_e U^{b_p}) \qquad (5.10)$$

Equation 5.10 represents a unified model of active respirometry. Thus, when the proper conditions are imposed, equation 5.10 either becomes the TEF (equation 4.1) or the HPF (equation 4.3). The difference in SMR between the two models arises from two conditions: (1) if $b_e \rightarrow 0$, then $\Phi_f(U) = a\, cosh(b_e U^{b_p}) = a = a_p$; and, if $b_p = 1$, then $\Phi_f(U) = a\, cosh(b_e U) =$ equation 5.3. In order for SMR (a) to be shared between the TEF and the HPF, both models must converge towards linearity; because, if $b_e \rightarrow 0$, then the TEF becomes linear; and, if $b_p = 1$, then the HPF becomes linear. The question then is, why must b_p equal 1?—perhaps, when Brett (1964) first determined that $M = f(U)$ can be modeled (not predicted!) best as an ordinary *e* function. However, according to equation 5.10, the TEF is a special case of an exponential-power function (EPF):

$$M = f(U) = [a_e cosh(b_e U^{b_p}) + a_e sinh(b_e U^{b_p})] = a_e e^{b_e U^{bp}} \quad , \qquad (5.11)$$

where $b_p > 1$. The EPF is a new general model of active respirometry and can be proven via another characterization other than the one described in equation 5.10. However, equation 5.10 is computationally expensive even though it represents a perfectly acceptable unified model of active respirometry. Therefore, I describe an analogous unified model of active respirometry that is much less computationally expensive.

Limit of a sequence

The exponential function e^U may be defined variously; for example, as the sum of *cosh*(U) and *sinh*(U)—the example described above; and as a limit of a sequence (MacDonald et al., 1937; Melzak, 1975):

$$e^U = \lim_{\gamma \to \infty} \left(1 + \frac{U}{\gamma} \right)^{\gamma} \tag{5.12}$$

Remarkably, equation 5.12 represents unity with the EPF and the HPF:

$$M = f(U) = a \left(1 + \frac{b_e U^{b_p}}{\gamma} \right)^{\gamma} \quad , \tag{5.13}$$

where γ is a conditional parameter. Hence, when $\gamma \to \infty$, equation 5.13 naturally equals the EPF:

$$M = f(U) = a_e e^{b_e U^{bp}} \quad ; \tag{5.14}$$

and when γ = 1, equation 5.13 equals the HPF:

$$M = f(U) = a_p + (a_p b_e) U^{b_p} \quad , \tag{5.15}$$

where $a_p b_e = \mu$. It is easy to see that TEF is a special case of the EPF—that is, if $\gamma \to \infty$ and $b_p = 1$, then the EPF becomes the TEF.

I have shown that when the TEF and the HPF are mathematically linked, the parameter b_p is a component of the unified model (equations 5.10 and 5.13); and that b_p must be greater than 1 (in the HPF) to represent an exponential change in M with respect to the change in U—a phenomenon in vertebrates that has been described in countless studies dating back to the 1960's. It has come to my attention from this analysis that energetic costs cannot be described accurately for the EPF ($\gamma \to \infty$; equation 5.13) when $b_p = 1$ (i.e., for the TEF) because this function lacks the parameter SCOS (μ); the same is true for the HPF (γ = 1; equation 5.13) when $b_p = 1$. If $b_p = 1$ for the HPF, then the HPF becomes the traditional linear function (TLF): $M = f(U) = a_p + \mu U$, where μ takes the

properties of b_p. So, in this case, the parameter μ does not represent SCOS but energy cost of transport (ECOT). The TLF clearly misrepresents $M = f(U)$ because, according to Videler and Nolet (1990), energetic costs cannot be accurately described from a linear relationship. Therefore, b_p must be greater than 1. So, why is there an apparent discrepancy in b_p between the TEF and HPF? The answer is simple—there is no discrepancy because b_p is a component of the unified model (equations 5.10 and 5.13), and it must be greater than 1 in order to describe energetic costs accurately.

To illustrate this issue, I depict graphically the EPF (equation 5.14) for three hypothetical curves when $b_p > 1$ (Appendix B). Then, I predict these curves using the TEF (i.e., the EPF when $b_p = 1$). The idea here is to show that the TEF can predict the EPF with great "accuracy" (i.e., high squared-correlation coefficients; r^2) except that it is obviously not a true representation of the actual function.

The conditional parameter γ is very interesting because it represents the dynamics of oxygen consumption (metabolism) between the two models. From a physical sense, γ represents fission between the two models—that is, the EPF for $\gamma \rightarrow \infty$ and the HPF for $\gamma = 1$; and, γ may represent fusion of the two models—that is, γ may take a value greater than 1 but much less than required for convergence to the *e* function. The latter is a novel idea, and I have yet to bring closure to it. There is tremendous potential for exploration of ideas on this new concept of metabolic "fusion" dynamics. From an evolutionary point-of-view, fission and fusion of respirometric models may represent a metabolic strategy of organisms to adapt to their environment. Because this is a new concept, I am currently working on tackling this issue from different disciplines.

If more information is needed to fully grasp the analyses presented above, I highly recommend two excellent articles on the history and theory of the *e* function; they were a source of indispensable knowledge from which this chapter developed: Cajori (1913)—for its history and Huntington (1916)—for its theory.

CHAPTER VI
BODY SHAPE ADAPTATIONS IN BLUEGILL SUNFISH: TRADE-OFFS BOTH IN SWIMMING PERFORMANCE AND METABOLIC MAINTENANCE

> *One must regard nature reasonably and naturally as one would the truth, and be contented only with a representation of it which errs to the smallest possible extent.*
>
> — János Bolyai (1802–1860)

Introduction

Body shape is a main factor contributing to hydrodynamic drag (resistance) in fishes (Lighthill, 1969; Pettersson and Hedenström, 2000; Webb, 1975; Wu, 1971), and is highly correlated with swimming efficiency, which is directly associated with reproduction (Webb, 1994; Videler, 1993; Ohlberger et al., 2006) and therefore subject to selection pressures that increase fitness (Priede, 1985; Ohlberger et al., 2006). Body shape places constraints on the capacity and efficiency of fish to use foods and habitats (Wainwright, 1991, 2002; Mathews, 1998; Svanbäck and Eklöv, 2004; Ohlberger et al., 2006). In particular, many fish species have formed shallow bodies for efficient swimming, especially when subjected to flowing water habitats, which is ideal for convergent evolution to reduce swimming costs in such habitats (Scarnecchia, 1988; Ohlberger et al., 2006). Hence, hydrodynamic resistance decreases as a result of streamlining, that is, the process of becoming shallow-bodied (Vogel, 1981).

Also, there might be potential for body shape diversification in this system. For instance, a fitness trade-off between swimming efficiency (= inverse measure of metabolic transport rate; MTR) and metabolic maintenance (= direct measure of standard metabolic rate; SMR) should occur among morphs specialized for either a still water habitat, where high MTR is accompanied by low SMR, or a flowing water habitat, where low MTR is accompanied by high SMR. The following three propositions lead to the

hypothesis that a trade-off could exist between MTR (i.e., swimming cost) and SMR (i.e., maintenance cost) across different water flow-rate habitats: (1) deep-bodied fishes have a significantly lower maintenance cost than shallow-bodied individuals (Pettersson and Brönmark,1999); (2) deep-bodied fishes are more maneuverable than stable, while shallow-bodied individuals are more stable than maneuverable (Chwang and Wu, 1974–1976; Webb, 1993); (3) swimming efficiency is a direct measure of stability—high swimming efficiency implies low hydrodynamic resistance implies high stability (Chwang and Wu, 1974–1976; Webb, 1993).

To evaluate swimming efficiency in fishes, it is imperative to evaluate the force of resistance (F_d ; equation 3.5). However, direct measurement of F_d is very difficult because it requires complex measurements of several hydromechanical factors (Fung, 1990). Therefore, investigators often take an alternative approach, that is, by measuring the fish's total metabolic (oxygen consumption) rate during sustained swimming, because the expenditure of energy during swimming, or the MTR, is reflected in the rate of change of total oxygen consumption over the change in swimming speed (Tucker, 1970, 1975). Hence, the MTR contains information on aerobic swimming efficiency and is frequently used for comparing swimming costs among fishes (Korsmeyer et al., 2001). The MTR can be derived accurately from the hydrodynamics-based power function. Estimating SMRs, and consequently maintenance costs, can easily be done by extrapolating to zero swimming speed (see chapters IV and V for details).

In this study, I focus on two-dimensional body shape (i.e., multivariate traits composing body shape) of bluegill sunfish to explain differences in both maintenance and swimming costs between a still water habitat and a flowing water habitat. The primary objectives of the study were to (1) evaluate SMR and MTR as a metabolic maintenance trait and as a hydrodynamic swimming trait, respectively and (2) compare bluegills with respect to their metabolic maintenance costs and hydrodynamic swimming costs in relation to habitat and body shape characteristics. In addition to evaluating the relationship between SMR, MTR and shape, the standard cost of swimming (SCOS) was

calculated and evaluated as an intermediary trait describing the physiologic (as opposed to the hydrodynamic) response due to swimming.

The secondary objectives of the study were to (1) formulate robust estimates of SMR, SCOS, and MTR from noisy respirometric data and (2) delineate a robust methodology for evaluating the relationship between multivariate body shape and multivariate components of swimming performance.

Materials and methods

A total of 23 bluegills were caught live from Little Brazos River (LBR) and 36 from Moehlman's Slough (MO; Brazos River oxbow lake) in Brazos County, Texas, USA using wire-mesh stationary traps. Bluegills were transferred to the laboratory after capture and held in aquaria, where they were habituated to experimental conditions. They were subjected to constant water aeration and filtration at a temperature of 24 ± 0.5^{o}C—the approximate temperature of the two habitats during the time of capture.

Eight bluegills (~3 from LBR and ~5 from MO) were caught early morning followed by a 24-hour habituation period with no feeding. After habituation, one bluegill per hour was randomly selected for experimentation for a total consecutive run of 8 hours. After experimentation, fish were immersed in a lethal bath of the anaesthetic MS-222 (dose > 100 ppm) and then taken to the Large Animal Clinic, Texas A&M University, College Station for x-raying and, subsequently, for multivariate morphometric analysis. This procedure is in accordance to a certified Animal Use Protocol, #2004-93.

Experiments were conducted in a modified Brett-type swim tunnel respirometer designed by LoligoSystems, Netherlands. The respirometer, submerged in an aerated freshwater bath (24 ± 0.5^{o}C), was made of transparent Perspex and consisted of a 38.5-liter recirculation loop with water flow produced by a propeller (Korsmeyer et al., 2002). Rectilinear flow was sustained by a honeycomb flow-straightener (7 mm aperture diameter) followed by baffle and deflector screens that produced micro-turbulent flow through the swimming section (depth, 10.25 cm; width, 10.25 cm; length, 41 cm) (Korsmeyer et al., 2002). According to the frequency output (measured in hertz) of the

propeller's motor controller, flow speed was calibrated using a standard flow meter. Oxygen partial pressure in the respirometer was measured with an oxygen probe (Oxyguard Handy Series—galvanic cell, self-polarizing, and self-temperature compensating).

The time span of these experiments was approximately 16 weeks between the months of April and July of 2005. Specimens of bluegills from LBR (6.36–10.34 cm in total length weighing 10.28–46.78 g) and from MO (7.51–10.80 cm in total length weighing 18.75–51.50 g) were used in the study.

Respirometric analysis

The following procedure is nearly identical to the methods described in Korsmeyer et al. (2002):

> The respirometer was periodically flushed with freshwater from the bath for 4 minutes followed by a 1 minute closed mixing period and then 5 minutes of closed respirometry, during which the decrease of oxygen partial pressure in the system was recorded every second. The flushing, mixing, and measurement cycles were automated by computer, providing a measure of oxygen consumption rate every 10 minutes per swimming speed per fish for a total of 6 swimming speeds ranging from 1.0 to 3.5 body lengths per second (bls^{-1}) with 0.5 bls^{-1} step-wise increments.

Due to the solid-blocking effect, flow (swimming) speeds were corrected by using the equation of Bell and Terhune (1970):

$$U = U_o \left(1 + \left(0.8 \gamma \left(\frac{A_m}{A_s} \right)^{1.5} \right) \right) , \qquad (6.1)$$

where U is the corrected swimming speed, U_o is the original swimming speed, γ is a shape factor for the fish measured in body length over body thickness, A_m is the maximum cross-sectional area of the fish, and A_s is the cross-sectional area of the swimming section. Body thickness was calculated as the average of the fish depth and width (Korsmeyer et al., 2002). The cross-sectional area of the fish was assumed to be elliptical based on the maximal depth and width measurements (Korsmeyer et al., 2002).

An intermittent flow system allowed short-interval measurements of total metabolic (oxygen consumption) rate, which was determined from the slope of a linear regression of the decrease in oxygen partial pressure over time for each measurement cycle (i.e., for each swimming speed), using the equation:

$$M = f(t) = \chi\eta v \,, \tag{6.2}$$

where M is the total oxygen consumption rate, t is the time is seconds, χ is the slope, η is the solubility of oxygen in the water, and v is the volume of the fish subtracted from the volume of the respirometer.

SMR, which is a direct measure of maintenance cost, was derived from two analytical models that were used to characterize the relationship between equations 6.1 and 6.2: the traditional exponential function (TEF; equation 4.1) and the hydrodynamics-based power function (HPF; equation 6.3). The HPF was also used to derive SCOS (inverse measure of aerobic swimming capacity) and MTR (inverse measure of aerobic swimming efficiency). The exponent of the TEF (equation 4.1) also represents the MTR. However, unlike the MTR from the HPF, the MTR from the TEF is dependent on the SMR, which may confound results if significant differences of SMR exist within or among bluegill populations. Therefore, only the HPF was used to derive aerobic swimming efficiency in order to ensure independence of MTR from SMR (see chapters IV and V).

A novel robust parameter estimation method of the HPF was developed to correct noisy respirometric data, where the squared correlation coefficients (r^2) of M = f(t) across any swimming speed were between 0.38 and 0.99. HPF can be described equivalently as hydrodynamics-based power (equation 6.3), exponential (equation 6.4), or polynomial (equation 6.5) functions:

$$(M - a) = f(U) = bU^c + \varepsilon \,, \tag{6.3}$$

$$(M - a) = f(U) = be^{cln(U)} + \varepsilon \,, \tag{6.4}$$

or

$$M = f(U) = a + bU^c + \varepsilon \ , \qquad (6.5)$$

where constant a is the SMR, constant b is the SCOS, constant c is the MTR, variable ε is measurement error, and compound variable (M – a) is the increment cost of swimming (ICOS) commonly known as the net cost of swimming (Korsmeyer et al., 2002) or metabolic power (Fung, 1990). All three characterizations (equations 6.3 – 6.5) yield identical parameter (i.e., a, b, and c) estimates. The expression (M – a) = f(U) in equations 6.3 and 6.4 makes it easy to understand how ICOS relates with U but makes it difficult to evaluate SMR (a) because both equations are compounded with it. Hence, many investigators have calculated incorrect values of MTR (c) by substituting SMR values derived from the TEF for a (chapter IV). Therefore, equation 6.5 is the best characterization of the HPF because it directly relates M to U and can be fitted to polynomials, which provide a convenient form of expression because they can be differentiated and integrated readily. Unlike equations 6.3 and 6.4, where SMR (a) has to be determined first before deriving SCOS (b) and MTR (c), differentiation of equation 6.5 fitted to a polynomial makes it easy to evaluate SCOS (b) and MTR (c) first before deriving SMR (a), which is mathematically more elegant since the estimate of SMR (a) depends on the estimate of MTR (c), not the other way around.

Aerobic swimming capacity is an inverse measure of SCOS (b) and is dependent on ECOT (c). SCOS (b) is the skeletal muscle capacity with which biochemical energy (ATP; adenosine triphosphate) is converted to mechanical power of the muscle (Fung, 1990), which becomes important for analyzing the physiologic response due to swimming. SCOS (b) is a function of the coefficient of power (C_p) and the coefficient of resistance (C_d) defined in chapter III. Surprisingly, the mathematical relationship between b, c, C_d, and C_p has not been addressed or shown in the literature. Below I characterize the relationship between b, c, C_d, and C_p:

$$C_d = \frac{\phi(F_d U)}{qU} = C_p = \frac{\phi(M-a)}{qU} = \frac{\phi(bU^c)}{qU} \ \mapsto \phi = \frac{(qC_d)U}{(bU^c)} = \beta U \ , \qquad (6.6)$$

where F_d is the force of resistance (equation 3.5), q is the dynamic force (equation 3.2), and ϕ is a dimensionless measure of the overall efficiency of swimming (not to be confused with MTR). It is easy to see that $F_d U$ (i.e., the product of force and speed) is power (capacity); and, swimming capacity is a measure of ICOS (equations 5.3 and 5.4). From equation 6.6, C_p ($=C_d$) is the metabolic power (= M – a) over the dynamic power (= qU); and, the overall efficiency of swimming (ϕ) is the work done by the resistance force (= $q C_d U = F_d U$; see equation 3.5) over metabolic capacity (= bU^c).

The robust parameter estimation method begins by calculating the first derivative of equation 5 with respect to U, which yields the familiar expression (equation 4.4):

$$\frac{d\mathrm{M}}{d\mathrm{U}} = (\mathrm{b})(\mathrm{c})\mathrm{U}^{\mathrm{c}-1} \tag{6.7}$$

followed by calculating the second derivative of equation 6.5 with respect to U:

$$\frac{d^2\mathrm{M}}{d\mathrm{U}^2} = (\mathrm{b})(\mathrm{c})(\mathrm{c}-1)\mathrm{U}^{\mathrm{c}-2} \quad , \tag{6.8}$$

and then finally dividing equation 6.7 by equation 6.8:

$$\left(\frac{d\mathrm{M}}{d\mathrm{U}}\right)\left(\frac{d^2\mathrm{M}}{d\mathrm{U}^2}\right)^{-1} = \left(\frac{1}{\mathrm{c}-1}\right)\mathrm{U} + \psi \quad , \tag{6.9}$$

where constant ψ is a pseudo-parameter equal to zero for any value of a, b, and c only when power functions of the forms described above (i.e., equations 6.3 – 6.5) are satisfied and all values of variable ε are equal to zero. Thus, ψ is dependent on the form of expression and the values of ε. In addition, ψ is correlated with c only when any value of ε is not equal to zero. In a perfect system with no error, ψ does not exist, according to the calculations described above. However, no system is without error and thus ψ becomes useful for numerically representing a non-perfect system.

The next step is to model M = *f*(U) such that ψ approaches zero, which represents the correct form of expression (i.e., equation 6.5 is satisfied) and ε approaches zero. For a linear expression, the line equation that best fits the original data, in theory, should yield close parameter estimates. For nonlinear expressions such as equation 6.5, the polynomial equation that best fits the original data does not always yield close parameter estimates (i.e., multiple solutions may be attained when there is error). In fact, for high error (i.e., standard deviations of $\varepsilon > 0.1$), the best-fit curve almost always yields poor parameter estimates because the best fit also best predicts error. Therefore, the objective of this method is to model M = *f*(U) to yield the most likely parameter estimates of the original measurements of M = *f*(U).

Maximum likelihood parameter estimation (MLPE) is one of the best known methods to fit nonlinear expressions, but even this method is subject to high error especially when parameter constraints are not imposed. Although constraints help increase the predictability capacity of MLPE, many systems do not have constraints. Even for systems where some of the constraints are known, the parameters whose constraints are unknown are left subjected to low predictability and can even lower the predictability of the parameters whose constraints are known. Therefore, unless the constraints of all of the parameters are known, MLPE for a high order (> 2.0) nonlinear system, such as equation 6.5, does not perform well under high error. For fish, the power term c can take any value between 1.1 and 3.0 (Videler and Nolet, 1990).

Equation 6.9 is uniquely devised to extract pseudo-parameter ψ from the HPF that holistically captures variable ε but no discernible relationship can be deduced between them because ε is a random variable occupying negative and positive real values and ψ is a constant that is correlated with c. Nevertheless, the value of ψ deviates from zero when any value of ε deviates from zero and therefore the closer the values of ε approach zero the closer the value of ψ also approaches zero (i.e., ψ is a holistic function of ε).

A third-order polynomial is the highest order expression that can be fitted to equation 6.5 because its power term, according to Videler et al. (1990), cannot take any

value greater than 3.0. Therefore, increasing the order of the polynomial past 3.0 is redundant and could become problematic—a high order polynomial fluctuates between data points when ε is present. A third-order polynomial remains relatively stiff when ε is present and yields enough accuracy for expressions with power terms less than or equal to 3.0.

Cubic Hermite Splines are special third-order polynomials that are excellent for this system because they can be modified to fit $M = f(U)$ with various stiffness (smoothness) values by changing the tuning parameter (λ) from a modified form of the Catmull-Rom spline (ξ):

$$\xi = \frac{U - 1}{\lambda} \quad , \tag{6.10}$$

where λ is equal to 2 for a third-order polynomial of highest fit (i.e., lowest sum squared residuals). As the value of λ decreases from 2, the error term of the spline model has more weight and thus the fit becomes less stiff and more curved. On the other hand, as the value of λ increases from 2, the fit becomes stiffer and less curved. Equation 6.10 is important in cubic Hermite splines because it allows one to change possible curve fits across a set of data points (Becker et al., 1981). It should be noted that if λ deviates from 2, then the correlation between the spline fit $M = f(\xi)$ and the original respirometric data $M = f(U)$ decreases (i.e., increasing the sum squared residuals). However, it is not the best fit $M = f(\xi)$ that is important; rather, it is the best predicted parameter estimates of $M = f(U)$ that is imperative.

Turning our attention back to pseudo-parameter ψ, as λ randomly varies between 1 and 3, ψ approaches zero such that the predicted spline $M = f(\xi)$ is expressed in the appropriate form (i.e., equation 6.5) and that all values of ε approach zero. Thus, when all the ψ values are inverted (i.e., ψ^{-1}) for random values of λ between 1 and 3, a few spikes can be detected from the following plot:

$$\psi^{-1} = f(\lambda) \tag{6.11}$$

The spikes are simply the result of large changes in ψ^{-1} for small changes in λ. Only a few, usually 2, 3, or 4 spikes are detected, which correspond to possible solutions for M = *f*(U). Only one solutions (i.e., one λ), however, will result in M = *f*(ξ) that best predicts the parameter estimates for M = *f*(U). A Monte Carlo Analysis (MCA), where λ is randomly generating ψ^{-1} values, is used to simulate and subsequently plot equation 6.11 in order to detect spikes that represent possible solutions (figure 6.1). Occasionally, more than one solution may result in predicted parameter estimates that seem reasonable. The recommended procedure to take in this situation would be to choose the λ closest to 2—that is, a solution that also yields a higher correlation with M = *f*(U). Simulated trials have strongly supported this procedure.

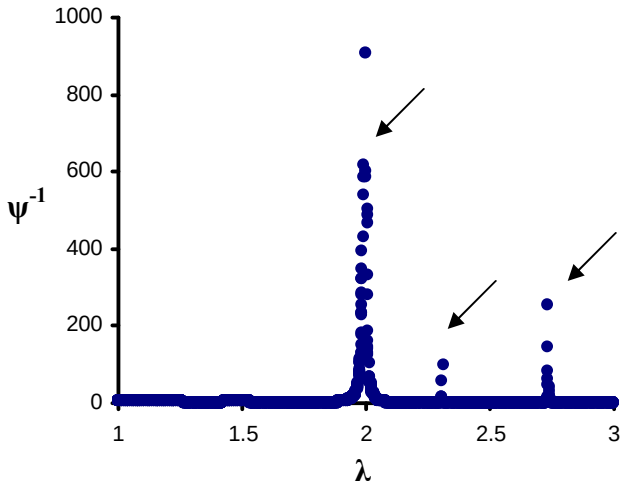

Figure 6.1. The relationship between pseudo-parameter ψ^{-1} and tuning parameter λ (equation 6.11; 3,000 random generations). Arrows represent possible solutions at λ = 2.0, 2.3, and 2.7. Only one λ, however, yields the best predicted estimates.

The cubic Hermite splines were constructed by splicing 4 third-order basis functions (Becker et al., 1981). These basis functions are linearly independent (i.e., orthogonal), which implies that each basis function associated with a particular node is constrained to 1 when evaluated at that node and is constrained to 0 at every other node

in the element (Becker et al., 1981). Then, the original cubic, a third-order polynomial, takes the following form:

$$M = f(\xi) = \varphi_0 + \varphi_1\xi + \varphi_2\xi^2 + \varphi_3\xi^3 \tag{6.12}$$

and impose the constraints (Becker et al., 1981):

$$M = f(0) = \varphi_0 = \Omega_1 \ , \tag{6.13}$$

$$M = f(1) = \varphi_0 + \varphi_1 + \varphi_2 + \varphi_3 = \Omega_2 \ , \tag{6.14}$$

where φ_i are the i^{th} cubic Hermite spline coefficients, Ω_1 is startpoint of the curve, and Ω_2 is the endpoint of the curve. Naturally, the cubic Hermite spline components Ω_1 and Ω_2 depend on parameters a, b, and c. One more computation is needed to complete the derivation of the cubic Hermite basis functions, that is, take the first derivative of equation 6.12:

$$\frac{dM}{d\xi} = \varphi_1 + 2\varphi_2\xi + 3\varphi_3\xi^2 \tag{6.15}$$

and impose the constraints (Becker et al., 1981):

$$\frac{dM}{d\xi} = f(0) = \varphi_1 = \Omega_3 \ , \tag{6.16}$$

$$\frac{dM}{d\xi} = f(1) = \varphi_1 + 2\varphi_2 + 3\varphi_3 = \Omega_4 \ , \tag{6.17}$$

where Ω_3 is the starting tangent of the curve (i.e., the rate at which the curve leaves Ω_1) and Ω_4 is the ending tangent of the curve (i.e., the rate at which the curve leaves Ω_2). The cubic Hermite spline components Ω_3 and Ω_4 only depend on parameters b and c because equations 6.16 and 6.17 are analogous to equation 6.7. However, by dividing equation 6.16 into equation 6.17, c depends solely on Ω_3 and Ω_4, because this operation is analogous to equation 6.9. The equation relating c with Ω_3 and Ω_4 is (figure 6.2):

$$c = 1 - \left[0.9 ln \left(\frac{\Omega_3}{\Omega_4} \right) \right] = 1 + \left[0.9 ln \left(\frac{\Omega_4}{\Omega_3} \right) \right] \quad (6.18)$$

Equation 6.18 represents a new general solution for c that comes directly from M = $f(\xi)$. Thus, the MTR can also be described as the logarithm of the relative tangent of the curve. Because a and b depend on c, equation 6.18 can be used to solve for a and b using equation 4.10 or 4.11.

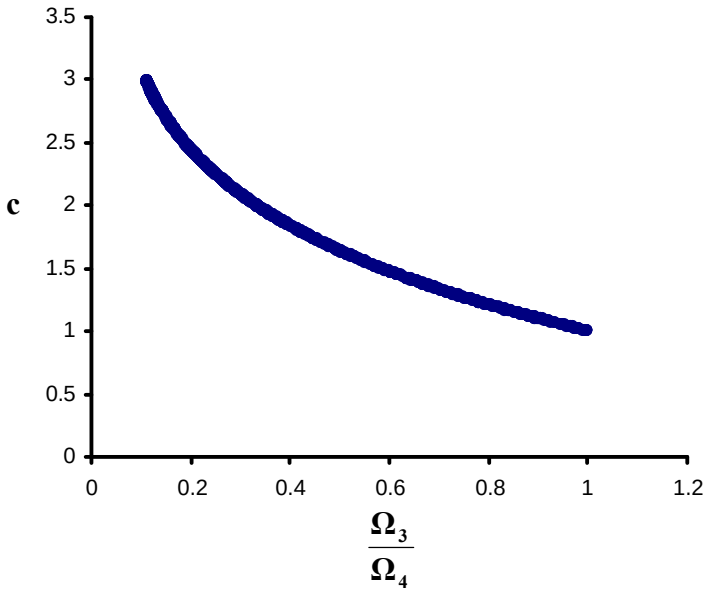

Figure 6.2. The relationship between MTR (c) and the cubic Hermite spline coefficients (=Ω_3 over Ω_4) (equation 6.18; 1, 000 random generations).

The four equations 6.13, 6.14, 6.16, and 6.17 in the four unknowns φ_0, φ_1, φ_2, and φ_3 are solved to give:

$$\varphi_0 = \Omega_1 \ , \quad (6.19)$$

$$\varphi_1 = \Omega_3 \ , \quad (6.20)$$

$$\varphi_2 = 3\Omega_2 - 3\Omega_1 - 2\Omega_3 - \Omega_4 \ , \quad (6.21)$$

and

$$\varphi_3 = \Omega_3 + \Omega_4 + 2\Omega_1 - 2\Omega_2 \tag{6.22}$$

Substituting φ_0, φ_1, φ_2, and φ_3 back into equation 6.12 then gives:

$$M = f(\xi) = \Omega_1 + \Omega_2\xi + (3\Omega_2 - 3\Omega_1 - 2\Omega_3 - \Omega_4)\xi^2 + (\Omega_3 + \Omega_4 + 2\Omega_1 - 2\Omega_2)\xi^3 \tag{6.23}$$

or, rearranging equation 6.23:

$$M = f(\xi) = \omega_1\Omega_1 + \omega_2\Omega_3 + \omega_3\Omega_2 + \omega_4\Omega_4 \ , \tag{6.24}$$

where ω_i are the i^{th} cubic Hermite basis functions, which are (Becker et al., 1981):

$$\omega_1 = 1 - 3\xi^2 + 2\xi^3 \ , \tag{6.25}$$

$$\omega_2 = \xi(\xi - 1)^2 \ , \tag{6.26}$$

$$\omega_3 = \xi^2(3 - 2\xi) \ , \tag{6.27}$$

and

$$\omega_4 = \xi^2(\xi - 1) \tag{6.28}$$

The final step required to solve Ω_i involves minimizing the sum squared residuals (ε^2), or maximizing the correlation between the predicted spline $M = f(\xi)$ and the original respirometric data $M = f(U)$:

$$\varepsilon^2 = \sum_{j=1}^{n} \left[\{M = f(U_j)\} - \{M = f(\xi_j)\} \right]^2 \tag{6.29}$$

or

$$\varepsilon^2 = \sum_{j=1}^{n} \left[M^j - \left(\omega_1^j\Omega_1 + \omega_2^j\Omega_3 + \omega_3^j\Omega_2 + \omega_4^j\Omega_4 \right) \right]^2 \ , \tag{6.30}$$

where n is the total number of measurements of $M = f(U)$. Next, minimize equation 6.30 such that the derivative of ε^2 with respect to Ω_i equals zero:

$$\frac{d\varepsilon^2}{d\Omega_1} = \sum_{j=1}^{n} 2\omega_1^j \left[\mathrm{M}^j - \left(\omega_1^j \Omega_1 + \omega_2^j \Omega_3 + \omega_3^j \Omega_2 + \omega_4^j \Omega_4 \right) \right] = 0 \ , \tag{6.31}$$

$$\frac{d\varepsilon^2}{d\Omega_2} = \sum_{j=1}^{n} 2\omega_2^j \left[\mathrm{M}^j - \left(\omega_1^j \Omega_1 + \omega_2^j \Omega_3 + \omega_3^j \Omega_2 + \omega_4^j \Omega_4 \right) \right] = 0 \ , \tag{6.32}$$

$$\frac{d\varepsilon^2}{d\Omega_3} = \sum_{j=1}^{n} 2\omega_3^j \left[\mathrm{M}^j - \left(\omega_1^j \Omega_1 + \omega_2^j \Omega_3 + \omega_3^j \Omega_2 + \omega_4^j \Omega_4 \right) \right] = 0 \ , \tag{6.33}$$

and

$$\frac{d\varepsilon^2}{d\Omega_4} = \sum_{j=1}^{n} 2\omega_4^j \left[\mathrm{M}^j - \left(\omega_1^j \Omega_1 + \omega_2^j \Omega_3 + \omega_3^j \Omega_2 + \omega_4^j \Omega_4 \right) \right] = 0 \ , \tag{6.34}$$

which can be expressed in matrix form:

$$2\begin{bmatrix} \omega_1^j \mathrm{M}^j \\ \omega_2^j \mathrm{M}^j \\ \omega_3^j \mathrm{M}^j \\ \omega_4^j \mathrm{M}^j \end{bmatrix} - 2\begin{bmatrix} \left(\omega_1^j\right)^2 & \omega_1^j \omega_2^j & \omega_1^j \omega_3^j & \omega_1^j \omega_4^j \\ \omega_2^j \omega_1^j & \left(\omega_2^j\right)^2 & \omega_2^j \omega_3^j & \omega_2^j \omega_4^j \\ \omega_3^j \omega_1^j & \omega_3^j \omega_2^j & \left(\omega_3^j\right)^2 & \omega_3^j \omega_4^j \\ \omega_4^j \omega_1^j & \omega_4^j \omega_2^j & \omega_4^j \omega_3^j & \left(\omega_4^j\right)^2 \end{bmatrix} \begin{bmatrix} \Omega_1 \\ \Omega_2 \\ \Omega_3 \\ \Omega_4 \end{bmatrix} = \begin{bmatrix} 0 \\ 0 \\ 0 \\ 0 \end{bmatrix} \ , \tag{6.35}$$

and rearranged to solve for Ω_i:

$$\begin{bmatrix} \left(\omega_1^j\right)^2 & \omega_1^j \omega_2^j & \omega_1^j \omega_3^j & \omega_1^j \omega_4^j \\ \omega_2^j \omega_1^j & \left(\omega_2^j\right)^2 & \omega_2^j \omega_3^j & \omega_2^j \omega_4^j \\ \omega_3^j \omega_1^j & \omega_3^j \omega_2^j & \left(\omega_3^j\right)^2 & \omega_3^j \omega_4^j \\ \omega_4^j \omega_1^j & \omega_4^j \omega_2^j & \omega_4^j \omega_3^j & \left(\omega_4^j\right)^2 \end{bmatrix}^{-1} \begin{bmatrix} \omega_1^j \mathrm{M}^j \\ \omega_2^j \mathrm{M}^j \\ \omega_3^j \mathrm{M}^j \\ \omega_4^j \mathrm{M}^j \end{bmatrix} = \begin{bmatrix} \Omega_1 \\ \Omega_2 \\ \Omega_3 \\ \Omega_4 \end{bmatrix} \ , \tag{6.36}$$

where solved values of Ω_i are substituted into equation 6.24 resulting in $\mathrm{M} = f(\xi)$. To make the tuning parameter λ in equation 6.10 useful in practice, one of the basis functions must be modified such that it becomes a function of U instead of ξ (Becket et al., 1981):

$$\omega_1 = f(\xi_{\lambda=2}) = 1 - 3\xi^2 + 2\xi^3 = f(U) = 1 - 3\left(\frac{U^2 - 2U + 1}{4}\right) + 2\left(\frac{U^3 - 3U^2 + 3U - 1}{8}\right), \quad (6.37)$$

where $\omega_1 = f(\xi)$ is substituted in equation 6.24 and $\omega_1 = f(U)$ is substituted in equations 6.30 – 6.36. Hence, when λ deviates from 2, $\omega_1 = f(U)$ remains constant but $\omega_1 = f(\xi)$ varies.

Using equation 5 (HPF) and applying equations 6.7 – 6.37 (robust parameter estimation) on 59 bluegills, the respirometric results (a, b, and c for each bluegill) can be described as blocks X_m:

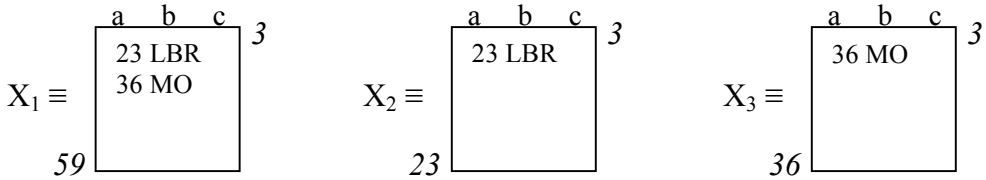

Because the respirometric parameters (a, b, and c) are expressed in different units of measurement, *z*-transforming (standardizing) each of them was necessary in order to make analysis of each comparable:

$$Z_m = \left[\frac{X_{ij} - \overline{X}_j}{\sigma_j}\right], \quad (6.38)$$

where Z_m is the m_X x *3* matrix of *z*-transformed X_m, X_{ij} refers to the element of X_m in the *i* row and the *j* column, $\overline{X}_j$ refers to the average of all the elements of X_m in the *j* column, and σ_j refers to the standard deviation of all the elements of X_m in the *j* column. The numerator in equation 1 represents mean-centering X_m to zero and the denominator represents scaling X_m to unit standard deviation (= 1). The elements in equation 38 are dimensionless because σ_j carries equivalent units of measurement with X_j.

Morphometric analysis

Multivariate body shape can be described as a collection of covarying traits consisting of 2-dimensional type I homologous coordinates (landmarks) along the periphery of the fish's body (figure 6.3). Although fineness ratios (ς; equation 3.6) of an elliptical body of revolution have been used to determine the influence of univariate shape on hydrodynamic resistance (Lanweber, 1961; Webb, 1975; Blake, 1983; Ohlberger et al., 2006), the type I homologous landmarks used in this study are better for capturing and defining the overall (i.e., multivariate) affect of body shape on the dynamics of the boundary layer flow because they are multivariate and thus covary in multidimensional shape space.

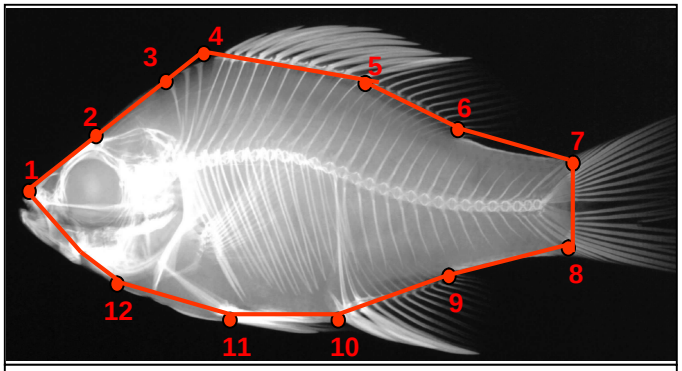

Figure 6.3. An x-ray of a typical bluegill sunfish digitized with 12 homologous landmarks using tpsDig.

Using tpsDig (ver 1.40), which is a morphometric freeware program designed by F. J. Rohlf, 12 type I homologous landmarks were obtained by digitizing x-ray images of each of the 59 total bluegills. Then, using tpsRelw (ver. 1.42), three separate analyses of generalized Procrustes superimposition of landmark data followed by principal components analysis (PCA) were performed (chapter I): the first analysis was designed to evaluate the relationship between body shape (W_1) and respirometry (Z_1) between habitats (i.e., between LBR and MO); the second and third analyses were designed to evaluate the relationship between body shape and respirometry within habitats—that is,

within LBR (W_2) and within MO (W_3), respectively. All three blocks were corrected for allometric effects using Burnaby's (1966) method (equation 2.19). The three allometry-free shape blocks are:

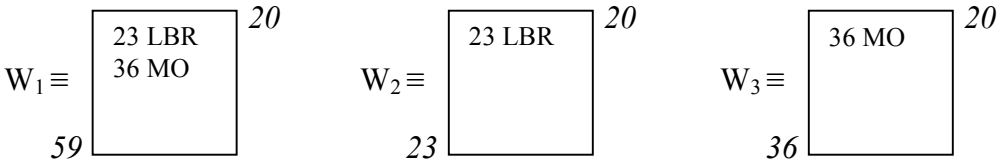

Statistical analysis

The most compelling indication of body shape diversification is a strong relationship (i.e., correlation or covariation) between body shape and swimming performance (i.e., MTR and SCOS; fitness components) because the link between them is central to the study of adaptation (Pettersson and Hedenström, 2000). Indeed, this relationship explains body shape diversification via divergent natural selection (i.e., adaptation → evolution). One of the best methods to describe the covariation between morphological variation and fitness variation is partial least-squares analysis (PLS). This method, unfortunately, has not become popular among ecologists or biologists partly because of the scarcity of software containing it; in addition, many investigators are more familiar with its conceptual and counterintuitive analog, canonical correlation analysis (CCoA). Therefore, I describe in detail below the mathematical framework of PLS.

PLS is an unconstrained partial ordination method that is commonly used to describe the covariation between two blocks of multivariate data (Zelditch et al., 2004). PLS is mathematically similar to PCA and conceptually similar to CCoA. Unlike CCoA and linear regression, PLS describes symmetric axes of covariation, where matrices do not comprise causes and effects (Zelditch et al., 2004). This makes PLS an attractive method, especially for evaluating the relationship between shape variables (as one matrix) and swimming performance components (as the other matrix).

PLS begins with at least two distinct blocks of data: W (M_W x N_W) and Z (M_Z x N_Z), both of which share objects, that is, $M_W = M_Z$. A joint asymmetric matrix Ψ is then calculated by pre-multiplying W^T to Z (Phatak and De Jong, 1997):

$$\Psi = W^T Z \tag{6.39}$$

where Ψ is a N_W x N_Z matrix representing linear combinations of both blocks such that the space of W is transposed onto the space of Z. Partial regression coefficients (partial eigenvectors; singular vectors) and their corresponding covariances (partial eigenvalues; singular values) can be obtained by performing a two-step eigendecomposition (singular-value decomposition; SVD):

$$\Psi\Psi^T = V\Lambda_L V^T \tag{6.40}$$

and

$$\Psi^T\Psi = U\Lambda_R U^T \ , \tag{6.41}$$

where $\Psi\Psi^T$ is a N_W x N_W left symmetric matrix, $\Psi^T\Psi$ is a N_Z x N_Z right symmetric matrix, V is a N_W x N_W orthonormal set ($V^TV = I$) of left singular vectors, U is a N_Z x N_Z orthonormal set ($U^TU = I$) of right singular vectors, Λ_L is a N_W x N_W diagonal matrix of squared singular values, Λ_R is a N_Z x N_Z diagonal matrix of squared singular values, and the N_Z squared singular values of $\Lambda_L = \Lambda_R$. Thus, PLS of the joint matrix Ψ is a linear function (i.e., linear combination) of the two unshared components N_W and N_Z with respect to the shared component $M_W = M_Z$. Equations 6.40 and 6.41 are then combined to form the equation (Phatak and De Jong, 1997):

$$\Psi = \hat{V}(\Lambda)^{\frac{1}{2}}\hat{U}^T \ , \tag{6.42}$$

where $\Sigma = (\Lambda)^{\frac{1}{2}}$ is a N_Z x N_Z diagonal matrix of singular values because N_Z must be less than N_W, $\hat{V}$ describes orthonormal partial linear regression coefficients (partial slopes) of the unshared component represented by the rows of Ψ, $\hat{U}$ describes the partial slopes of

the unshared component represented by the columns of Ψ, and Σ represents covariation (not variation) between each pair of singular vectors from $\hat{V}$ and $\hat{U}$. The components of covariation between blocks are described by the singular values of Σ, which can also be determined from the covariances between (Phatak and De Jong, 1997):

$$\Xi_W = W\hat{V} \tag{6.43}$$

and

$$\Xi_Z = Z\hat{U} \quad , \tag{6.44}$$

where Ξ_W is a M_W x N_Z matrix of singular scores describing the partial ordinations of W projected onto the space of Z and Ξ_Z is a M_Z x N_Z matrix of singular scores describing the partial ordinations of Z projected onto the space of W. Because $M_W = M_Z$, equations 6.43 and 6.44 can be plotted together (because $\hat{V}$ and $\hat{U}$ represent singular axis-pairs), which describe the relationship between the two unshared components of W and Z (two distinct descriptors) with respect to their shared component (one predictor). Equations 6.43 and 6.44 characterize PLS of the N_Z singular axes of W and Z. The proportion (percent) of the major component of covariation (Σ_1) between W and Z is determined by dividing Σ_1 by the sum of all Σ.

It is important to note that PLS can only operate on an asymmetric matrix Ψ—that is, blocks W and Z must be distinct. In other words, SVD yields right and left singular vectors only when $W \neq Z$. If $W = Z$, then the joint block $\Psi = W^TZ$ is symmetric and therefore SVD of Ψ is equivalent to ED of W^TW or Z^TZ. In this case, PLS no longer describes covariation between W and Z, rather it describes variation in W or Z (i.e., PLS becomes PCA). Basically, the only relevant difference between PLS and PCA is that PLS operates on an asymmetric matrix $\Psi = W^TZ$ (equation 6.37); whereas PCA operates on a symmetric matrix $H = W^TW$.

An intuitive geometric interpretation of SVD can be very helpful for understanding the mathematics of PLS (equations 6.39 – 6.44). Let A be a *4* x *2* matrix of x-y coordinates describing a quadrilateral (figure 6.4):

$$A = \begin{bmatrix} 1 & 1 \\ 1 & -1 \\ -1 & -1 \\ -1 & 1 \end{bmatrix} \tag{6.45}$$

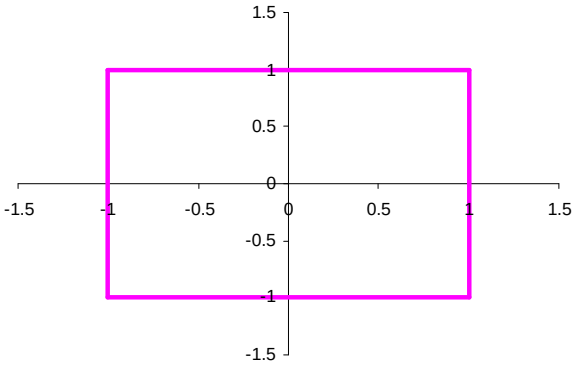

Figure 6.4. Mean-centered quadrilateral described from matrix A (equation 6.45).

Then, using a 2-dimensional rotation matrix V, rotate A 28.6^o clockwise (i.e., transpose V):

$$V = \begin{bmatrix} \cos(\theta) & \sin(\theta) \\ -\sin(\theta) & \cos(\theta) \end{bmatrix} = \begin{bmatrix} 0.88 & 0.48 \\ -0.48 & 0.88 \end{bmatrix}, \tag{6.46}$$

$$AV^T = \begin{bmatrix} 1.36 & 0.40 \\ 0.40 & -1.36 \\ -1.36 & -0.40 \\ -0.40 & 1.36 \end{bmatrix}, \tag{6.47}$$

where θ is equal to 0.5 radians (=28.6^o); and using a 2-dimensional uniform deformation matrix Σ, compress A in the y-axis by 0.5 units:

$$\Sigma = \begin{bmatrix} 1 & 0 \\ 0 & 0.5 \end{bmatrix} , \tag{6.48}$$

$$B = AV^T\Sigma = \begin{bmatrix} 1.36 & 0.20 \\ 0.40 & -0.68 \\ -1.36 & -0.20 \\ -0.40 & 0.68 \end{bmatrix} , \tag{6.49}$$

where B represents the transformation of A under rotation and compression (figure 6.5).

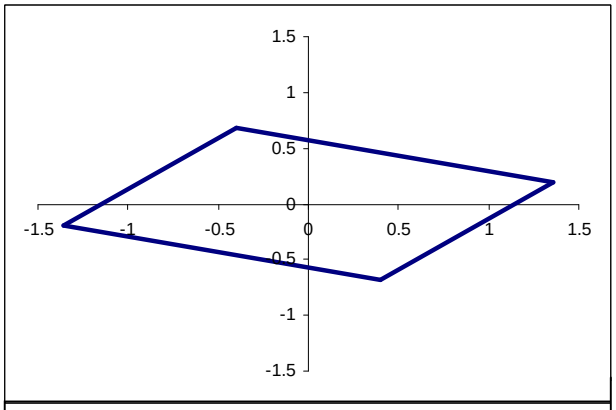

Figure 6.5. Mean-centered, rotated, and compressed quadrilateral described from matrix B (equation 6.49).

SVD of A^TB should recover the rotational and scaling effects imposed on A. Following equations 6.39 – 6.42, the joint matrix Ψ:

$$\Psi = \frac{A^TB}{h} = \begin{bmatrix} 0.86 & -0.24 \\ 0.48 & 0.44 \end{bmatrix} , \tag{6.50}$$

where h is the number of x-y coordinates (i.e., $h = 4$). Then, SVD of Ψ:

$$\Psi\Psi^T = \begin{bmatrix} 0.83 & 0.32 \\ 0.32 & 0.42 \end{bmatrix} = \begin{bmatrix} 0.88 & -0.48 \\ 0.48 & 0.88 \end{bmatrix} \cdot \begin{bmatrix} 1 & 0 \\ 0 & 0.25 \end{bmatrix} \cdot \begin{bmatrix} 0.88 & 0.48 \\ -0.48 & 0.88 \end{bmatrix} \tag{6.51}$$

and

$$\Psi^{T}\Psi = \begin{bmatrix} 1 & 0 \\ 0 & 0.25 \end{bmatrix} = \begin{bmatrix} 1 & 0 \\ 0 & 1 \end{bmatrix} \cdot \begin{bmatrix} 1 & 0 \\ 0 & 0.25 \end{bmatrix} \cdot \begin{bmatrix} 1 & 0 \\ 0 & 1 \end{bmatrix}, \tag{6.52}$$

where equations 6.51 and 6.52 are combined to recover the rotational and scaling effects (via SVD of Ψ):

$$\Psi = \hat{V}\Sigma\,\hat{U}^{T} = \begin{bmatrix} 0.88 & -0.48 \\ 0.48 & 0.88 \end{bmatrix} \cdot \begin{bmatrix} 1 & 0 \\ 0 & 0.5 \end{bmatrix} \cdot \begin{bmatrix} 1 & 0 \\ 0 & 1 \end{bmatrix} \tag{6.53}$$

Then, PLS projects A onto the space of B:

$$\Xi_{A} = A\hat{V}^{T} = \begin{bmatrix} 1.36 & 0.40 \\ 0.40 & -1.36 \\ -1.36 & -0.40 \\ 0.40 & 1.36 \end{bmatrix}, \tag{6.54}$$

where the first column of Ξ_{A} is singular axis 1 from A (Ξ_{A1}), the second column of Ξ_{A} is singular axis 2 from A (Ξ_{A2}), and the elements of Ξ_{A1} and Ξ_{A2} are called singular scores; and PLS projects B onto the space of A:

$$\Xi_{B} = A\hat{U} = \begin{bmatrix} 1.36 & 0.20 \\ 0.40 & -0.68 \\ -1.36 & -0.20 \\ 0.40 & 0.68 \end{bmatrix}, \tag{6.55}$$

where the first column of Ξ_{B} is Ξ_{B1} and the second column of Ξ_{B} is Ξ_{B2}. The covariation between Ξ_{A1} and Ξ_{B1} is $\Sigma_{1} = 1$, and the covariation between Ξ_{A2} and Ξ_{B2} is $\Sigma_{2} = 0.5$. Therefore, geometrically, the singular vectors ($\hat{V}$ and $\hat{U}$) are orthonormal projections and the singular values (Σ) are uniform deformations.

Covaritation between shape and respirometric variables

If there are significant interactions between W_1 and Z_1, then PLS cannot be performed accurately using W_1 because significant habitat interactions with a, b, and/or c yield conflicting covariance structures. In other words, PLS determines singular vector-pairs in nearly perpendicular directions due to significant habitat (LBR and MO) interactions with a, b, and/or c. These nearly perpendicular singular vector-pairs essentially cancel each other and the loadings (partial regression coefficients) are nearly zero along the singular axes of W_1 and Z_1; what remains accounted for in PLS is only the variation in W_1 and Z_1, not the covariation between W_1 and Z_1. This is a vitally important issue because PLS cannot be performed accurately using any two blocks of data. Thus, the reason for separating W_2 and W_3 from W_1 is because of this issue of conflicting covariance structures in PLS. Matrices W_2 and W_3 lack shape differences between habitats because they only represent shape variation within a habitat, not between habitats like W_1. Hence, there are no conflicting covariance structures between W_2 and Z_2, and between W_3 and Z_3. PLS can thus be performed accurately using these matrices.

To verify whether significant interactions exist between W_1 and Z_1 just perform MANCOVA, where shape (W_1) is regressed on habitat (i.e., LBR and MO), centroid size (cs), SMR (a) , SCOS (b), MTR (c), habitat x cs, habitat x SMR, habitat x SCOS, habitat x MTR. The last three interactions are then evaluated using the p-statistic, which determines whether the interactions are significant (i.e., p-statistic < 0.05 implies significance). Table 6.1 below shows the result of the MANCOVA (software: JMP ver. 5.0.1).

Table 6.1. Results of the MANCOVA.

Effect	p-statistic	Effect	p-statistic
habitat	0.0025	habitat x cs	0.5914
cs	0.0394	habitat x SMR	0.9404
SMR	0.2763	habitat x SCOS	0.6963
SCOS	0.3526	habitat x MTR	0.9103
MTR	0.4831		

The interactions between habitat and Z_1 are not significant, which implies there are no conflicting covariance structures between W_1 and Z_1. PLS can then be performed accurately using these two matrices:

$$\Psi_1 = W_1^T Z_1 \quad , \tag{6.56}$$

where Ψ_1 is the *20* x *3* joint matrix representing linear combinations of W_1 and Z_1 such that the space of W_1 is transposed onto the space of Z_1. Singular vector-pairs and their corresponding singular values can be obtained by performing SVD of equation 6.56:

$$\Psi_1 \Psi_1^T = V_1 \Lambda_{L1} V_1^T \tag{6.57}$$

and

$$\Psi_1^T \Psi_1 = U_1 \Lambda_{R1} U_1^T \quad , \tag{6.58}$$

where $\Psi_1 \Psi_1^T$ is a *20* x *20* left symmetric matrix, $\Psi_1^T \Psi_1$ is a *3* x *3* right symmetric matrix, V_1 is a *20* x *20* orthonormal set of left singular vectors, U_1 is a *3* x *3* orthonormal set of right singular vectors, Λ_{L1} is a *20* x *20* diagonal matrix of squared singular values, Λ_{R1} is a *3* x *3* diagonal matrix of squared singular values, and the 3 squared singular values of Λ_{R1} equals the first three squared singular values of Λ_{L1}. Thus, PLS of the joint matrix Ψ_1 is a linear combination of the 20 shape and 3 respirometric components with respect to the 59 bluegills. Equations 6.57 and 6.58 are then combined to form the SVD equation:

$$\Psi_1 = \hat{V}_1 \Sigma_1 \hat{U}_1^T \quad , \tag{6.59}$$

where Σ_1 *3* x *3* diagonal matrix of singular values, $\hat{V}_1$ (*20* x *3*) describes orthonormal partial slopes of the 20 shape components projected onto Z_1, $\hat{U}_1$ (*3* x *3*) describes the partial slopes of the 3 respirometric components projected onto W_1, and Σ_1 represents covariation between each pair (i.e., 3 pairs) of singular vectors from $\hat{V}_1$ and $\hat{U}_1$. The

components of covariation between blocks are described by the singular values of Σ_1, which can also be determined from the covariances between:

$$\Xi_{W_1} = W_1 \hat{V}_1 \tag{6.60}$$

and

$$\Xi_{Z_1} = Z_1 \hat{U}_1 \quad , \tag{6.61}$$

where Ξ_{W_1} is a *59* x *3* matrix of singular scores describing the partial ordinations of W_1 projected onto the space of Z_1 and Ξ_{Z_1} is a *59* x *3* matrix of singular scores describing the partial ordinations of Z_1 projected onto the space of W_1. Because Ξ_{W_1} and Ξ_{Z_1} are in the same space, each pair of singular scores (axes) can be plotted together (figures 6.6 and 6.7)—that is, the first singular axis of W_1 ($\Xi_{W_1}^{1}$; *59* x *1*) can be plotted with the first singular axis of Z_1 ($\Xi_{Z_1}^{1}$; *59* x *1*).

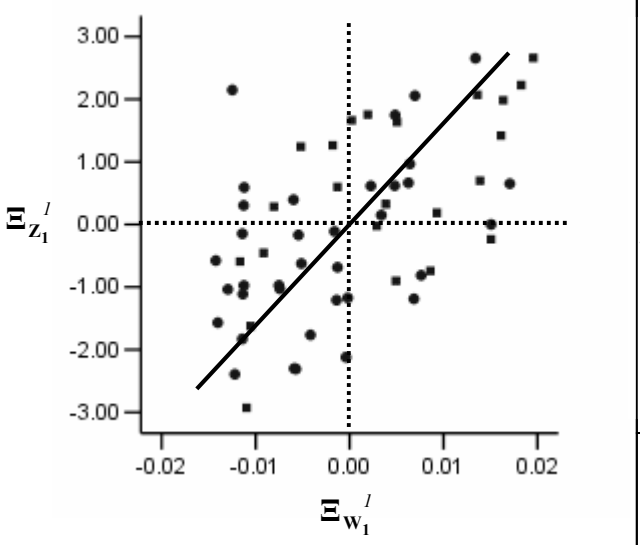

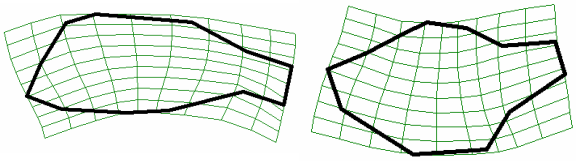

Low SMR (a)
High SCOS (b)
Low MTR (c)

High SMR (a)
Low SCOS (b)
High MTR (c)

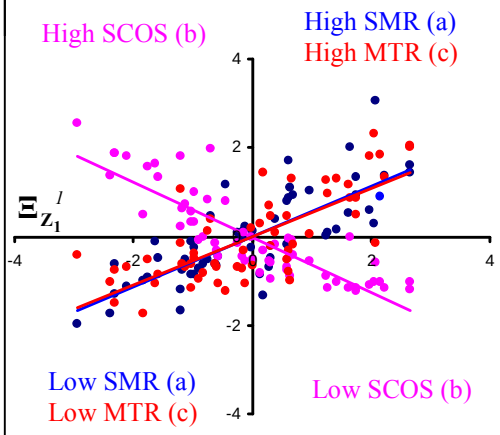

Figure 6.6. Thin-plate spline visualizations of singular warp $\Xi_{W_1}^{1}$. *Left*—the relationship between the 1st singular axis-pair between LBR and MO ($\Xi_{Z_1}^{1}$ ≡ respirometric parameters and $\Xi_{W_1}^{1}$ ≡ body shape), which accounted for 54.56% of the total covariation between W_1 and Z_1 (p-statistic = 0.041; 10,000 random permutations). *Top*—the relationship between Z_1 (≡ *z*-transformed a, b, and c) and $\Xi_{Z_1}^{1}$. All visualizations have been magnified by 3x (tpsRegr).

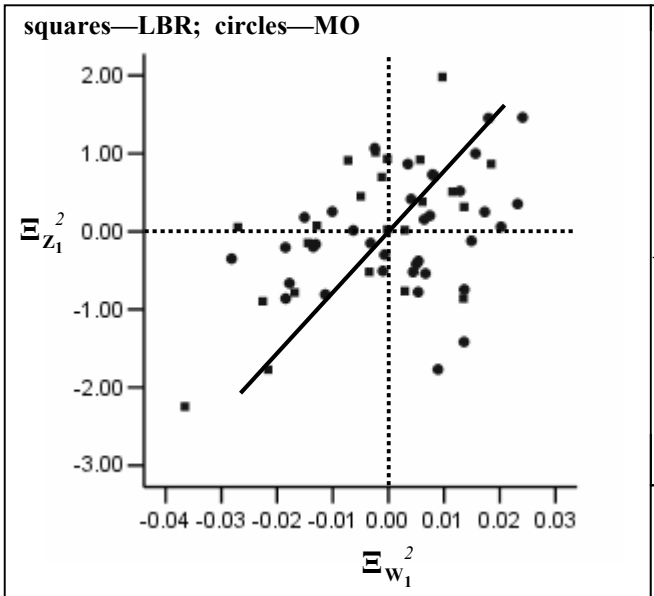

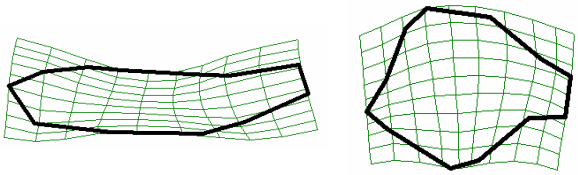

High SMR (a)
Low MTR (c)

Low SMR (a)
High MTR (c)

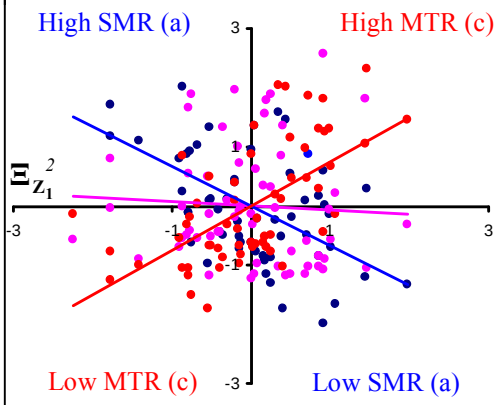

Figure 6.7. Thin-plate spline visualizations of singular warp $\Xi_{W_1}^2$. *Left*—the relationship between 2nd singular axis-pair between LBR and MO, which accounted for 35.25% of the total covariation between W_1 and Z_1 (p-statistic = 0.002; 10,000 random permutations). *Top*—the relationship between Z_1 and $\Xi_{Z_1}^2$. All visualizations have been magnified by 3x (tpsRegr).

Decompose the $\Xi_{W_1}^{\ 1}$ divergent shape axis into its uniform components of shape deformation:

negative axis ≡ 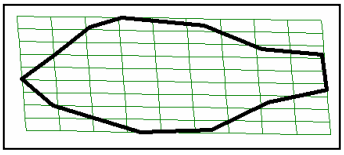 positive axis ≡ 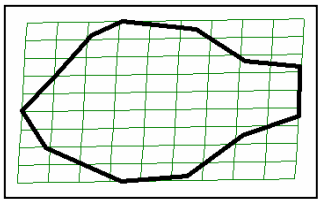

and its non-uniform components of shape deformation:

negative axis ≡ 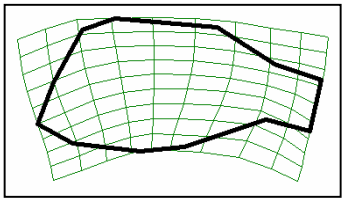 positive axis ≡ 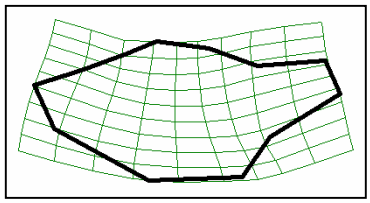

Also, decompose the $\Xi_{W_1}^{\ 2}$ divergent shape axis into its uniform components of shape deformation:

negative axis ≡ 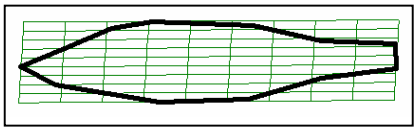 positive axis ≡ 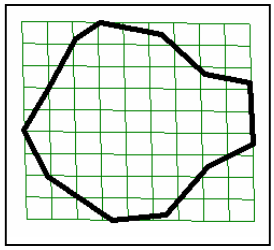

and its non-uniform components of shape deformation:

negative axis ≡ 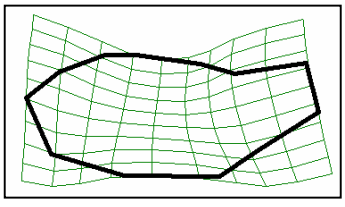 positive axis ≡ 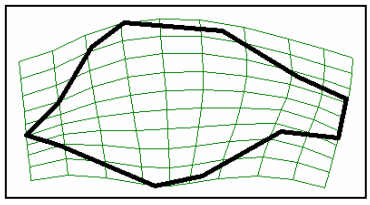

The $\Xi_{W_1}^{1}$ shape axis clearly describes a shallow- and deep-bodied divergent shape generalization, where bluegills from LBR and MO show convergent shape patterns for low SMR, low MTR, and high SCOS, and for its incident inverse (i.e., high SMR, high MTR, and low SCOS). The negative shape axis of $\Xi_{W_1}^{1}$ describes bluegills with a low metabolic maintenance cost (≡ low SMR), a high swimming efficiency (≡ low MTR), and a low swimming capacity (≡ high SCOS). The positive shape axis of $\Xi_{W_1}^{1}$ describes bluegills with a high metabolic maintenance cost (≡ high SMR), a low swimming efficiency (≡ high MTR), and a high swimming capacity (≡ low SCOS). These results suggest that the $\Xi_{W_1}^{1}$ shape axis does not represent a trade-off between swimming efficiency (c; purely hydrodynamic → fluid dynamic efficiency of propulsion) and metabolic maintenance (a; purely physiologic → metabolic response due to the environment); but, it does suggest a trade-off between skeletal muscle capacity and swimming efficiency (i.e., a trade-off in swimming performance), because SCOS (b) is the physiologic response due to swimming and MTR (c) is the hydrodynamic response due to swimming. Implications of this interesting trade-off are addressed in the *Discussion*.

The $\Xi_{W_1}^{2}$ shape axis also describes a shallow- and deep-bodied divergent shape generalization, where bluegills from LBR and MO show convergent shape patterns for high SMR and low MTR, and for its incident inverse (i.e., low SMR and high MTR). SCOS contributes very little to the divergent shape effect of $\Xi_{W_1}^{2}$—that is, its partial regression slope is essentially zero. The negative shape axis of $\Xi_{W_1}^{2}$ describes bluegills with a high metabolic maintenance cost (≡ high SMR) and a high swimming efficiency (≡ low MTR). The positive shape axis of $\Xi_{W_1}^{2}$ describes bluegills with a low metabolic maintenance cost (≡ low SMR) and a low swimming efficiency (≡ high MTR). These results suggest that the $\Xi_{W_1}^{2}$ shape axis does represent a trade-off between swimming efficiency and metabolic maintenance.

Repeat equations 6.56 – 6.59 using W_2 and Z_2. Then, the joint matrix representing linear combinations of W_2 and Z_2 is Ψ_2 (*20* x *3*). Thus, the SVD equation is:

$$\Psi_2 = \hat{V}_2 \Sigma_2 \hat{U}_2^T \quad , \tag{6.62}$$

where Σ_2 *3* x *3* diagonal matrix of singular values, $\hat{V}_2$ (*20* x *3*) describes orthonormal partial slopes of the 20 shape components projected onto Z_2, $\hat{U}_2$ (*3* x *3*) describes the partial slopes of the 3 respirometric components projected onto W_2, and Σ_2 represents covariation between each pair (i.e., 3 pairs) of singular vectors from $\hat{V}_2$ and $\hat{U}_2$. The components of covariation between blocks are described by the singular values of Σ_2, which can also be determined from the covariances between:

$$\Xi_{W_2} = W_2 \hat{V}_2 \tag{6.63}$$

and

$$\Xi_{Z_2} = Z_2 \hat{U}_2 \quad , \tag{6.64}$$

where Ξ_{W_2} is a *23* x *3* matrix of singular scores describing the partial ordinations of W_2 projected onto the space of Z_2 and Ξ_{Z_2} is a *23* x *3* matrix of singular scores describing the partial ordinations of Z_2 projected onto the space of W_2. Because Ξ_{W_2} and Ξ_{Z_2} are in the same space, each pair of singular scores (axes) can be plotted together (figure 6.8). Only the second singular axis-pair ($\Xi_{W_2}^2$ and $\Xi_{Z_2}^2$) was plotted because it was significant.

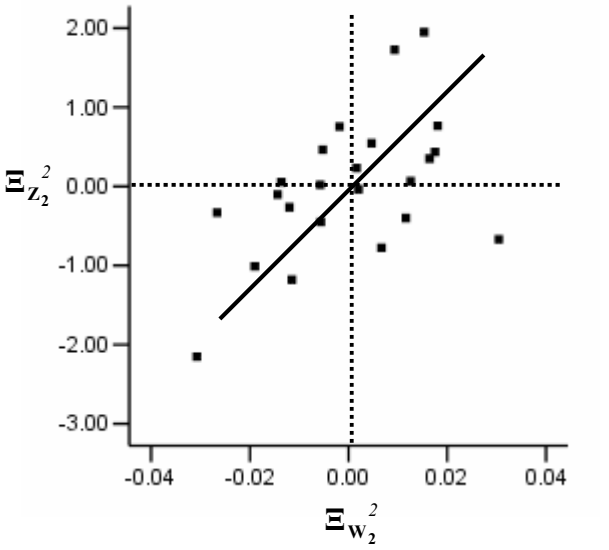

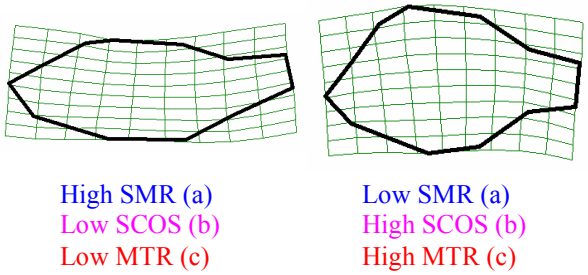

High SMR (a)
Low SCOS (b)
Low MTR (c)

Low SMR (a)
High SCOS (b)
High MTR (c)

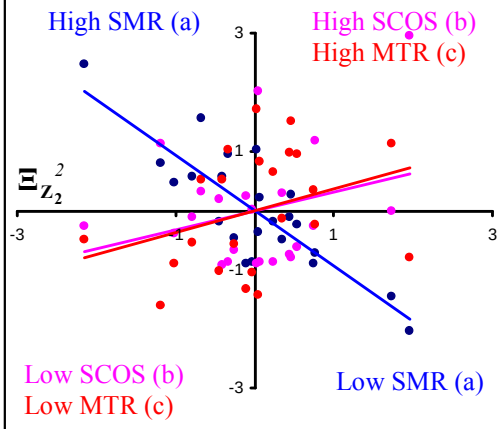

Figure 6.8. Thin-plate spline visualizations of singular warp $\Xi_{W_2}^2$. *Left*—the relationship between 2nd singular axis-pair within LBR ($\Xi_{Z_2}^2 \equiv$ respirometric parameters and $\Xi_{W_2}^2 \equiv$ body shape), which accounted for 38.67% of the total covariation between W_2 and Z_2 (p-statistic = 0.042; 10,000 random permutations). *Top*—the relationship between Z_2 and $\Xi_{Z_2}^2$. All visualizations have been magnified by 3x (tpsRegr).

The $\Xi_{W_2}^2$ shape axis is essentially identical to the $\Xi_{W_1}^2$ shape axis, except that $\Xi_{W_2}^2$ accounted for approximately 3% more covariation than $\Xi_{W_1}^2$ between blocks. The $\Xi_{W_2}^2$ shape axis describes a shallow- and deep-bodied divergent shape generalization, where bluegills within LBR show convergent shape patterns for high SMR, low SCOS, and low MTR, and for its incident inverse (i.e., low SMR, high SCOS, and high MTR). These results suggest that the $\Xi_{W_2}^2$ shape axis represents a trade-off between swimming performance (i.e., SCOS and MTR) and metabolic maintenance. This trade-off makes perfect sense for bluegills in a flowing water habitat, because bluegills require more than

just being hydromechanically fit for swimming against flowing water (due to body shape adaptations aimed at reducing hydrodynamic resistance). According to figure 6.8, they also require being physiologically fit for swimming against flowing water (due to skeletal muscle adaptations aimed at providing a high conversion rate of ATP to mechanical power of the muscles). Basically, the $\Xi_{W_2^2}$ divergent shape axis represents an adaptive response due to flowing water. Because SCOS depends on MTR, bluegills that are hydromechanically fit for swimming against flowing water spend more time swimming in the stream, where physiological acclimation (cardiovascular conditioning and/or myoplasticty) to physically intense activity can occur.

Repeat equations 6.56 – 6.59 using W_3 and Z_3. Then, the joint matrix representing linear combinations of W_3 and Z_3 is Ψ_3 (*20* x *3*). Thus, the SVD equation is:

$$\Psi_3 = \hat{V}_3 \Sigma_3 \hat{U}_3^T \quad , \tag{6.65}$$

where Σ_3 *3* x *3* diagonal matrix of singular values, $\hat{V}_3$ (*20* x *3*) describes orthonormal partial slopes of the 20 shape components projected onto Z_3, $\hat{U}_3$ (*3* x *3*) describes the partial slopes of the 3 respirometric components projected onto W_3, and Σ_3 represents covariation between each pair (i.e., 3 pairs) of singular vectors from $\hat{V}_3$ and $\hat{U}_3$. The components of covariation between blocks are described by the singular values of Σ_3, which can also be determined from the covariances between:

$$\Xi_{W_3} = W_3 \hat{V}_3 \tag{6.66}$$

and

$$\Xi_{Z_3} = Z_3 \hat{U}_3 \quad , \tag{6.67}$$

where Ξ_{W_3} is a *36* x *3* matrix of singular scores describing the partial ordinations of W_3 projected onto the space of Z_3 and Ξ_{Z_2} is a *36* x *3* matrix of singular scores describing the partial ordinations of Z_3 projected onto the space of W_3. Because Ξ_{W_2} and Ξ_{Z_2} are in the same space, each pair of singular scores (axes) can be plotted together (figure 6.9). None of the 3 singular axis-pairs were significant (i.e., the p-statistics were greater than 0.05). Only the first singular axis-pair was relatively close to significance (i.e., p-statistic = 0.172, as opposed to 0.546 and 0.824). Therefore, I chose to plot the first singular-axis-pair ($\Xi_{W_3}^{1}$ and $\Xi_{Z_3}^{1}$), even though it does not represent a statistically significant divergent shape effect.

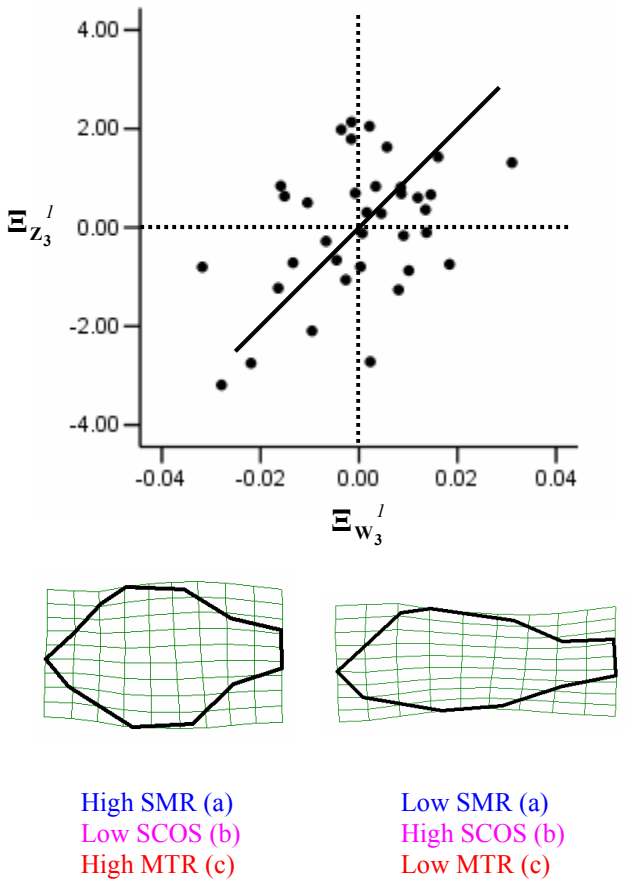

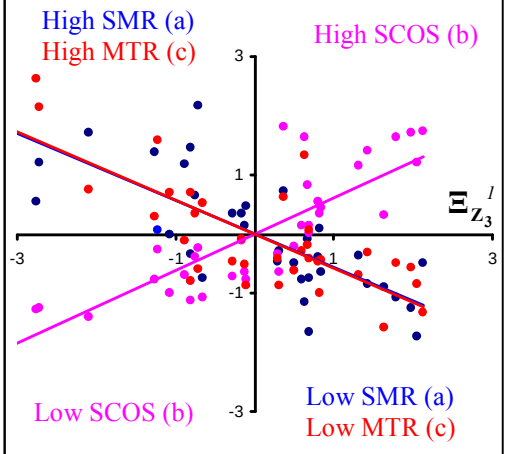

Figure 6.9. Thin-plate spline visualizations of singular warp $\Xi_{W_3}^{1}$. *Left*—the relationship between 1st singular axis-pair within MO ($\Xi_{Z_3}^{1} \equiv$ respirometric parameters and $\Xi_{W_3}^{1} \equiv$ body shape), which accounted for 60.69% of the total covariation between W_3 and Z_3 (p-statistic = 0.172; 10,000 random permutations). *Top*—the relationship between Z_3 and $\Xi_{Z_3}^{1}$. All visualizations have been magnified by 3x (tpsRegr).

The $\Xi_{W_3}^{1}$ shape axis is nearly identical to the $\Xi_{W_2}^{2}$ shape axis, except that $\Xi_{W_3}^{1}$ accounted for approximately 20% more covariation than $\Xi_{W_2}^{2}$ between blocks and that the $\Xi_{W_3}^{1}$ divergent shape effect is not significant. The chart below summarizes the results of figures 6.6 – 6.8.

Parameters of the HPF	**Interpretation**
SMR (a)	metabolic response due to the environment and genome
SCOS (b)	physiologic response due to swimming – a measure of capacity skeletal muscle adaptations (muscle ATP conversion rate)
MTR (c)	hydrodynamic response due to swimming – a measure of efficiency body shape adaptations (shallow- and deep-bodied)
Shape-Respirometric Response	**Trade-off**
between LBR and MO:	
If {SMR ‖ MTR} = *A*, then SCOS x *A*	between swimming capacity and metabolic maintenance between swimming capacity and swimming efficiency
If SCOS = Ø, then SMR x MTR	between metabolic maintenance and swimming efficiency
within LBR:	
If {SCOS ‖ MTR} = *B*, then SMR x *B*	between metabolic maintenance and swimming capacity between metabolic maintenance and swimming efficiency
The symbol ‖ denotes "matches with" and represents no trade-off. The symbol x denotes "crosses with" and represents a trade-off. The symbol Ø represents neutrality.	

Discussion

Ohlberger et al. (2006) investigated the relationship between a univariate measure of body shape (i.e., fineness ratio; equation 3.6) and swimming efficiency (MTR) from two species of cyprinid fish under controlled environmental conditions. Their analysis suffers from a lack of robustness with respect to morphological, physiological, and statistical calculations. Firstly, their morphometric analysis of body shape consisted of a univariate traditional trait, namely, a fineness ratio. Although the fineness ratio is a well-established measure of slenderness, it is also an incomplete representation of body-shape design; a fineness ratio does not provide enough information on body shape to formulate a robust analysis of the relationship between swimming performance and morphology. Secondly, they use inappropriate estimates of SMR (see chapters IV and V). Thirdly, their statistical analysis, where fineness ratios were regressed on MTR values, is inadequate and provides nothing that is substantive; least-squares regression, which is an asymmetric method, relates cause and effect with shape and swimming efficiency, which is ill-conceived from an evolutionarily perspective. There is no evidence to suggest that swimming efficiency predicts morphology, or morphology predicts swimming efficiency. Morphology and swimming efficiency, however, may simply covary—nothing that suggests a cause-and-effect relationship. With multivariate shape and respirometric parameters, and confirming insignificance of habitat interactions with effects of interest, PLS is a formative method to analyze the covariation between two blocks of multivariate data because PLS does not assume that one block causes the other; but, rather views both blocks as linearly related to the same underlying causes (Zelditch et al., 2004). Also, PLS is a robust method to investigate possible trade-offs between effects on shape.

The significant trade-off between swimming efficiency and metabolic maintenance between river and oxbow lake habitats, and within the river—both shape effects are equivalent—suggests a metabolic-hydrodynamic interaction. The interaction is due to the synergistic effects of optimal cruising speed (U_m) with SMR (a) and aerobic swimming capacity (= inverse measure of SCOS; b^{-1}), because U_m is proportional to

SMR and aerobic swimming capacity ($= b^{-1} \propto \phi$). Weihs (1973) calculated U_m using dimensional analysis of fluid dynamics (see equations 3.1–3.5). I substituted Weihs' (1973) derivation of U_m for the parameters in equation 6.6:

$$U_m = \sqrt{\frac{\beta a}{(qC_d)U^{-2}}} = \sqrt{\frac{(\phi U^{-1})(F_d U)}{(F_d)U^{-2}}} = \sqrt{\phi U^2} \qquad (6.68)$$

From equation 6.68, it clear that U_m is directly proportional to SMR (a) and ϕ ($\propto b^{-1}$). Many investigators have come to the conclusion that U_m depends solely on MTR—that is, fish with high aerobic swimming efficiencies have higher optimal cruising speeds. Figure 6.6 does not support this conclusion. Equations 6.6 and 6.68 show that U_m also depends on SCOS (a parameter that has been neglected or misunderstood by many investigators). It turns out that the position of the caudal peduncle (not necessarily a shallow- and deep-bodied shape effect) is the divergent shape characterization that is consistent with U_m. Fish with erect caudal peduncles have higher optimal cruising speeds because they have either high maintenance costs (high SMR) or high aerobic swimming capacities (low SCOS); whereas, fish with prone caudal peduncles have lower optimal cruising speeds because they have either low maintenance costs (low SMR) or low aerobic swimming capacities (high SCOS). The hydrodynamic nature of the U_m shape effect (or, I should say, positional effect of the caudal peduncle) is unknown.

In figures 6.6 – 6.8, a shallow- and deep-bodied divergent shape generalization is associated with MTR; shallow-bodied fish are more efficient at swimming than deep-bodied fish. This is consistent with the results of Ohlberger et al. (2006). SMR, however, is not associated with a shallow- and deep-bodied shape effect, which is inconsistent with the results of Pettersson and Hedenström (1999) and Ohlberger et al. (2006).

Taken together, the results show that shallow-bodied bluegills from both the river and oxbow may or may not optimally swim faster with higher swimming efficiencies (low MTR) compared to deep-bodied bluegills from both the river and oxbow. On the other hand, shallow-bodied bluegills from the river optimally swim faster with higher

swimming efficiencies (low MTR), thus having a significantly higher swimming performance compared to deep-bodied bluegills from the river.

As far as maintenance cost is concerned, shallow-bodied bluegills from the river require more sustenance (due to a higher SMR) than deep-bodied bluegills; and, if SMR is high, then fish need to have either a low SCOS (high aerobic swimming capacity → high U_m) or a low MTR (high aerobic swimming efficiency) in order to have high foraging performance—an adaptive strategy, perhaps, aimed at increasing survivorship. This is consistent with the results shown in figures 6.6 – 6.8.

In figure 6.6, there exists an interesting trade-off between aerobic swimming capacity and aerobic swimming efficiency—that is, a trade-off between skeletal muscle capacity and the fluid dynamic efficiency of propulsion, respectively. It is well known that prolonged physically intense activity (which can be induced by water flow) significantly increases cardiovascular and skeletal muscle capacity (Bone, 1975; Korsmeyer et al., 1997; Gallaugher et al., 2001; Farrell, 2002; Pelster et al., 2003; Gamperl et al., 2004). This conditioning not only increases the rate of blood flow to high metabolically active tissues such as cardiac and skeletal muscles (which increases aerobic swimming capacity—see Bone, 1975), but also decreases the rate of blood flow to low metabolically active tissues such as the gut (for fishes: Hernadez et al., 2002; Farrell et al., 2001) and gonads (for mammals: Lotgering et al., 1983; Meyer et al., 1994; Morris et al., 1956). This raises some interesting questions as to how assimilation efficiency and fecundity are affected by the redistribution of blood flow during prolonged physically intense activity in fishes. Also, the physiological adaptations that may be associated with fishes subjected to water flow (such as those adaptations seen in figures 6.6 – 6.8) could manifest into internal morphological adaptations such as shorter gut lengths, smaller gonads, and larger cardiac and skeletal muscles (Covell et al., 1991). Hence, the functional consequences of these physiological and morphological adaptations associated with flowing water habitats can be related to reproduction and therefore fitness.

CHAPTER VII
CONCLUSION

I value the discovery of a single even insignificant truth more highly than all the argumentation on the highest questions which fails to reach a truth.

— Galileo Galilei (1564–1642)

Chapter synthesis

The main objectives of the dissertation were to (1) derive SMR, MTR, and SCOS from respirometric data using the HPF (see chapters IV, V, and VI for mathematical details) and (2) compare these three estimates with bluegills from flowing and still-water habitats (chapter VI). The main idea behind this comparison is that bluegills (freshwater sunfish, in general) are more shallow-bodied from flowing water habitats compared to bluegills from still-water habitats. It has been suggested that shallow-bodied fish are more efficient at swimming against high water flow than deep-bodied fish because water flow, like body shape, is a factor contributing to hydrodynamic resistance and streamlining delays the point of boundary layer separation (chapters II and III).

The overall swimming efficiency (= resistance over thrust) is composed of hydrodynamic and physiologic components, both of which represent different aspects of the relationship between resistance and thrust (figure 7.1). For instance, there are several factors responsible for contributing to hydrodynamic resistance—the principal contributor being body shape. Thus, body shape adaptations, such as streamlining, aim at reducing hydrodynamic resistance in the presence of water flow in order to counteract the drag forces due to the wave speed (w_2)—see figure 7.1. Thus, streamlining in fish is an adaptive response to increase swimming efficiency. If hydrodynamic resistance decreases as a result of streamlining, then the thrust to overcome resistance also decreases, thereby increasing the overall swimming efficiency. However, it is possible that the thrust or metabolic power required to overcome resistance is compromised due to a decrease in the overall capacity of the skeletal muscles to generate mechanical

power. This is where the physiological state of the fish matters in regard to swimming efficiency.

The relationship between metabolic power and swimming speed (where w_1 is assume to be equivalent to U; see figure 7.1 and chapter III) can be best characterized by the HPF (equation 4.2), where the MTR (b_p) depends on factors contributing to hydrodynamic drag (Webb, 1993), such as the geometry of the fish's body and its attitude relative to the flow (Lighthill, 1969; Wu, 1971; Webb, 1975, 1978; Fung, 1990); and the SCOS (μ) depends on physiological factors that are characteristic of swimming performance, such as the overall capacity of skeletal muscle, which is proportional to mitochondrial density (Davies et al., 1981; Videler, 1993; Pelster et al., 2003). As the resistive forces increase, mechanical power generated by the skeletal muscles must also increase for the fish to swim. The overall capacity of the skeletal muscles then determines the amount of oxygen consumption needed to generate mechanical power to overcome the resistive forces (see figure 7.1). The MTR, on the other hand, is directly proportional to the force of drag exerted by the water on the fish's body (Webb, 1993). Pettersson and Hedenström (2000) showed that high-drag morphs (i.e., deep-bodied fishes) have higher MTRs and therefore lower swimming efficiencies compared to low-drag morphs (i.e., shallow-bodied fishes).

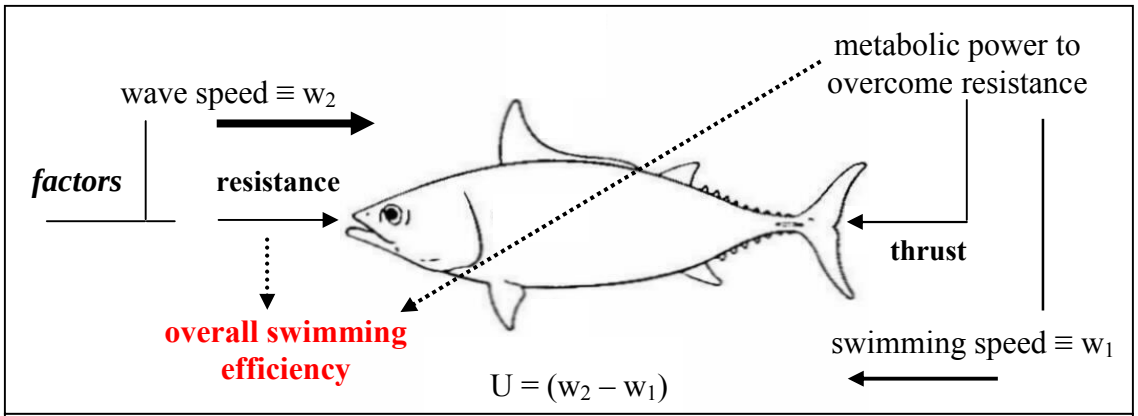

Figure 7.1. Forces acting on a swimming fish, where resistance over thrust represents the overall swimming efficiency. The relationship between metabolic power and swimming speed (w_1) is characterized best by the hydrodyanmics-based power function (HPF; equation 4.2), where w_1 is assumed to be equivalent to the relative velocity (U). Fish cartoon adapted from Magnuson (1978).

The physiological consequences, such as maintenance (i.e., SMR) and muscle compensations (i.e., SCOS) resulting in high energetic costs associated with resistance-reducing strategies (i.e., reducing MTR), are the most interesting results from chapter VI. For instance, in figure 7.2, shallow-bodied bluegills are efficient swimmers (i.e., low swimming costs) but have high maintenance costs (i.e., high costs of living) and low swimming capacities (i.e., low mitochondrial densities). On the other hand, deep-bodied bluegills are inefficient swimmers (high swimming costs) but have low maintenance costs (i.e., low costs of living) and high swimming capacities (high mitochondrial densities). This is a clear example of divergent natural selection acting on MTR. For convergence, however, the position of the caudal peduncle is consistent with the range of w_1, or optimal swimming speed (U_m). Bluegills with erect caudal peduncles have a large range of w_1 without suffering much cost of swimming compared to bluegills with prone caudal peduncles (figure 7.2). The adaptive physiological response to high U_m is due to a high aerobic swimming capacity (i.e., low SCOS) because swimming efficiency is low (i.e., high MTR) and metabolic maintenance is high (i.e., high SMR). In other words, bluegills that are inefficient swimmers (i.e., high MTR—high energy output rate per unit distance) and require a higher energy intake (i.e., high SMR) cannot survive unless they gain the ability to increase their foraging capacity through thrust or metabolic power reduction (i.e., low SCOS)—see figure 7.2. This is perhaps one of the most remarkable adaptive physiological responses due to shape and standard metabolism.

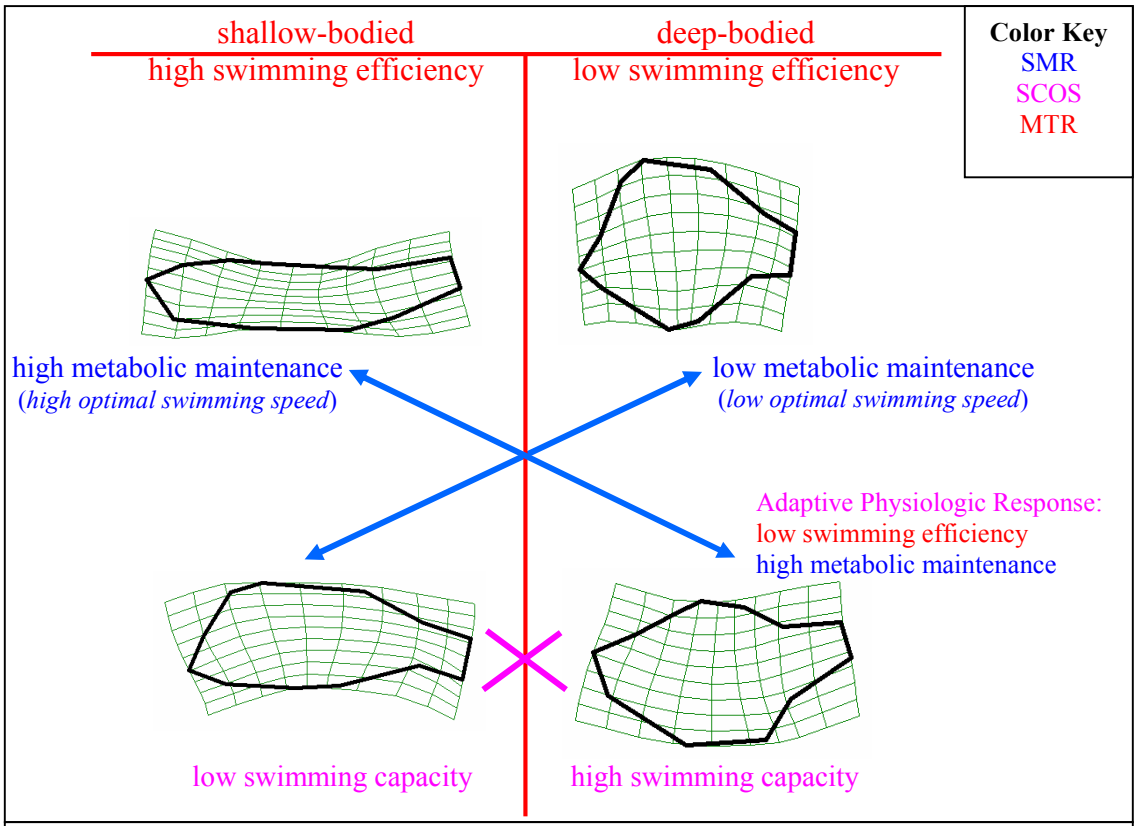

Figure 7.2. Thin-plate spline visualizations attributable to singular scores from partial least-squares analysis, where the covariation between shape and SMR, MTR, and SCOS were tested simultaneously (chapter VI). The visualizations show an adaptive physiologic response due to a trade-off between MTR and SMR.

REFERENCES

Bainbridge, R. A., 1958. The speed of swimming of fish as related to size and to the frequency and amplitude of the tail beat. J Exp Biol 37: 109–133.

Bainbridge, R. A., 1963. Caudal fin and body movement in the propulsion in some fish. J Exp Biol 40: 23–56.

Beamish, F. W. H., 1978. Swimming capacity. In Fish Physiology, vol. 7 (ed.W. S. Hoar and D. J. Randall), pp. 101–189. Academic Press, New York.

Becker, A. B., Carey, G. F., and Oden, J. T., 1981. Finite Elements: An Introduction. Englewood Cliffs, Prentice-Hall, NJ.

Blake, R. W., 1983. Functional design and burst-and-coast swimming in fishes. Can J Zool 61: 2491–2494.

Bone, Q., 1975. Muscular and energetic aspects of fish swimming. In Swimming and Flying in Nature (ed. T.Y. Wu, C.J. Brokow, and C. Brennen), pp. 493–528, Plenum Press, New York.

Bookstein, F. L., 1996. Combining the tools of geometric morphometrics. In Adavances in Morphometrics (ed. L. F. Marcus, M. Corti, A. Loy et al.), pp. 131–151, Plenum Press.

Breder, C. M., 1926. The locomotion of fishes. Zoologica 4: 159–297.

Brett, J. R., 1963. The energy required for swimming by young sockeye salmon with a comparision of drag force on dead fish. Trans Royal Soc Can 1: 441–457.

Brett, J. R., 1964. The respiratory metabolism and swimming performance of young sockeye salmon. J Fish Res Bd Can 21: 1183–1226.

Burnaby, T. P., 1966. Growth-invariant discriminant functions and generalized distances. Biometrics 22: 96–110.

Cajori, F., 1913. History of the exponential and logarithmic concepts. Am Math Mon 20: 205–210.

Campbell, N. A. and Atchley, W. R., 1981. The geometry of canonical variates analysis. Syst Zool 30: 268–280.

Chwang, A. T. and Wu, T. Y., 1974–1976. Hydrodynamics of low-Reynolds-number flow. Part I: (1974) Rotation of axisymmetric prolate bodies. J Fluid Mech 63: 607–622. Part III: (1975) Motion of spheriodal particle in quadratic flows. *ibid*. 72: 17–34. Part IV: (1976) Translation of spheroids. *ibid*. 75: 677–689.

Covell, J . W., Smith, M., Harper, D. G., Blake, R. W., 1991. Skeletal muscle deformation in the lateral muscle of the intact rainbow trout Oncorhynchus mykiss during fast start maneuvers. J Exp Biol 156: 453–466.

Davies, K. J. A., Packer, L., Brooks, G. A., 1981. Biochemical adaptation of mitochondria, muscle, and whole-animal respiration to endurance training. Arch Biochem Biophys 209: 538–553.

Dryden, I. L. and Mardia, K. V., 1998. Statistical Shape Analysis. John Wiley & Sons.

Farrell, A. P., Thorarensen, H., Axelsson, M., Crocker, C. E., Gamperl, A. K., and Cech, J. J., 2001. Gut blood flow in fish during exercise and severe hypercapnia. Comp Biochem Physiol A Mol Intgr Physiol 128: 551–563.

Farrell, A. P., 2002. Cardiorespiratory performance in salmonids during exercise at high temperature: insights into cardiovascular design limitations in fishes. Comp Biochem Physiol A Mol Integr Physiol 132: 797–810.

Finney, R. L. and Thomas, G. B., 1994. Calculus. (Second Edition) Addison-Wesley, Massachusetts.

Fung, Y. C., 1990. Biomechanics: Motion, Flow, Stress, and Growth. Springer-Verlag, New York.

Gallaugher, P. E., Thorarensen, H., Kiessling, A., and Farrell, A. P., 2001. Effects of high intensity exercise training on cardiovascular function, oxygen uptake, internal oxygen transport and osmotic balance in Chinook salmon (*Oncorhynchus tshawytscha*) during critical speed swimming. J Exp Biol 204: 2861–2872.

Gamperl, A. K. and Farrell, A. P., 2004. Cardiac plasticity in fishes: environmental influences and intra-specific differences. J Exp Biol 207: 2539–2550.

Gordon, M. S., Chin, H. G., Vojkovich, M., 1989. Energetics of swimming in fishes using different modes of locomotion: I. Labriform swimmers. Fish Physiol Biochem 6: 341–352.

Hernandez, M. D., Mendoiola, P., de Costa, J., Zamora, S., 2002. Effects of intense exercise traning on rainbow trout growth, body composition and metabolic responses. J Physiol Biochem 58: 1–7.

Huntington E. V., 1916. An elementary theory of the exponential and logarithmic functions. Am Math Mon 23: 241–246.

Hussain, S. S. and Sprent P., 1983. Non-parametric regression. J Royal Stat Soc Series A 146: 182–191.

Korsmeyer, K. E. and Dewar, H., 2001. Tuna metabolism and energetics. In Tuna: Physiology, Ecology and Evolution (ed. B. A. Block and E. D. Stevens), pp. 35–78. Academic Press, San Diego.

Korsmeyer, K. E., Steffensen, J. F., and Herskin J., 2002. Energetics of median and paired fin swimming, body and caudal fin swimming, and gait transition in parrotfish (*Scarus schlegeli*) and triggerfish (*Rhinecanthus aculeatus*). J Exp Biol 205: 1253–1263.

Lancaster. P., 1969. Theory of Matrices. Academic Press, New York.

Landweber, L., 1969. Motion of emmersed and floating bodies. In Handbook of Fluid Dynamics (ed. V. L. Streeter). McGraw-Hill, New York.

Langerhans, R. B. and DeWitt, T. J., 2004. Shared and unique features of evolutionary diversification. Am Nat 164: 335–349.

Lauder, G. V., 1996. The argument from design. In: Adaptation (ed. M. R. Rose and G. V. Lauder), pp. 55- 91. San Diego.

Legendre, P. and Legendre L., 1998. Numerical Ecology. Elsevier, Amsterdam.

Lighthill, J., 1969. Hydromechanics of aquatic animal propulsion—a survey. Ann Rev Fluid Mech 1: 413–446.

Lighthill, J., 1975. Mathematical Biofluiddynamics, Soc Indus Appl Math Philadelphia.

Lotgering, F. K., Gilbert, R. D., Longo, L. D., 1983. Exercise responses in pregnant sheep: oxygen consumption, uterine blood flow and blood volume. J Appl Physiol 55: 834-841.

MacDonald, J. K. L. and Sharpe, F. R., 1937. On some series arising from a definition of the exponential function. Am Math Mon 44: 312–315.

Mathews, W. J., 1998. Patterns in freshwater fish ecology. Kluwer Academic, New York.

Meyer, W. R., Pierce, E. F., Katz, V. L., 1994. The effect of exercise on reproductive function and pregnancy. Curr Opin Obstet Gynecol 6: 293-299.

Melzak, Z. A., 1975. On the exponential function. Am Math Mon 82: 842–844.

Metcalfe, N. B., Taylor, A. C., and Thorpe, J. E., 1995. Metabolic rate, social status and life history strategies in Atlantic salmon. Anim Behav 49: 431–436.

Morris, N., Osborn, S. B., Compos, G. R., Hartz, M.V., 1956. Effecitive uterine blood flow during exercise in normal and pre-eclamptic pregnancies. Lancet 2: 481-484.

Moyle, P. B. and Cech, J. J., 2004. Fishes: An Introduction to Ichthyology. Prentice-Hall, NJ.

Newman, J. N., 1973. The force on a slender fish-like body. J Fluid Mech 58: 689–702.

Newman J. N. and Wu, T. Y., 1973. A generalized slender-body theory for fish-like forms. J Fluid Mech 57: 673–693.

Ohlberger, J., Staaks, G., and Holker, F., 2006. Swimming efficiency and the influence of morphology on swimming costs in fishes. J Comp Physiol B 176: 17–25.

Pelster, B., Sanger, A. M., Siegele, M., and Schwerte, T., 2003. Influence of swim training on cardiac activity, tissue capillarization, and mitochondrial density in muscle tissue of zebrafish larvae. Am J Physiol Regul Integr Comp Physiol 285: 339–347.

Pettersson, L. B. and Brönmark, C., 1999. Energetic consequences of an inducible morphological defense in crucian carp. Oecologia 121: 12–18.

Pettersson, L. B. and Hedenström A., 2000. Energetics, cost reduction and functional consequences of fish morphology. Proc R Soc Lond B Biol Sci 267: 759–764.

Phatak, A and De Jong, S., 1997. The geometry of partial least-squares. J Chemometrics 11: 311-338.

Plaut, I., 2001. Critical swimming speed: its ecological relevance. Comp Biochem Physiol 131: 41–50.

Priede, I. G., 1985. Metabolic scope in fishes. In Fish Energetics: New Perspectives (ed. P Tytler and P Calow), pp. 33–64. John Hopkins University Press, Baltimore.

Rohlf, F. J., 1990. Rotational fit (Procrustes) methods. In Proceedings of the Michigan Morphometrics Workshop (ed. F. J. Rohlf and F. L. Bookstein), pp. 227–236, University of Michigan Museum of Zoology.

Scarnecchia, D. L., The importance of streamlining in influencing fish community structure in channelized and unchannelized reaches of a prairie stream. Reg Riv Res Manage 2: 155–166.

Steffensen, J. F., 1989. Some errors in respirometry of aquatic breathers: how to avoid and correct them. Fish Physiol Biochem 6: 49–59.

Svanbäck R. and Eklöv. P., 2004. Morphology in perch affects habitat specific feeding efficiency. Funct Ecol 18: 503–510.

Tucker, V. A., 1970. Energetic cost of locomotion in animals. Comp Biochem Physiol A 34: 841–846.

Tucker, V. A., 1975. The energetic sot of moving about. Am Sci 63: 413–419.

Videler, J. J., 1993. Fish Swimming. Chapman and Hall, New York.

Videler, J. J. and Nolet, B. A., 1990. Costs of swimming measured at optimum speed: scale effects, differences between swimming styles, taxonomic groups and submerged and surface swimming. Comp Biochem Physiol 97A: 91–99.

Vogel, S., 1981. Life in moving fluids. Willard Grant Press, Boston.

Wainwright, P. C., 1991. Ecomorphology: experimental functional anatomy for ecological problems. Am Zool 31: 635–645.

Wainwright, P. C., 2002. Ecomorphology of locomotion in labrid fishes. Environ Biol Fishes: 65, 47–62.

Walker, J. A., 2004. Dynamics of pectoral fin rowing in a fish with an extreme rowing stroke: the threespine stickleback. J Exp Biol 207: 1925–1939.

Wardle, C. S., Soofiani, N. M., O'Neill, F. G., Glass, C. W. and Johnstone, A. D. F., 1996. Measurements of aerobic metabolism of a school of horse mackerel at different swimming speeds. J Fish Biol 49: 854–862.

Webb, P. W., 1975. Hydrodynamics and energetics of fish propulsion. Bull Fish Res Bd Can 190: 109–119.

Webb, P. W., 1978. Hydrodynamics: nonscombroid fish. In: Fish Physiology, vol. 7 (ed. W. S. Hoar and D. J. Randall), pp. 189–237. Academic Press, New York.

Webb, P. W., 1993. Swimming. In The Physiology of Fishes (ed. D. H. Evans), pp. 47–73. CRC Press, Boca Raton.

Webb, P. W., 1994. Exercise performance of fish. In: Comparative Vertebrate Exercise Physiology: Phyletic Adaptations. (ed. J. H. Jones), pp. 1–49. Academic, San Diego.

Weihs, D., 1973. Optimal fish cruising speed. Nature 245: 48–50.

Wieser, W. and Medgyesy, N., 1990. Aerobic maximum for growth in the larvae and juveniles of cyprinid fish, *Rutilus rutilus*: implications for energy budgeting in small poikilotherms. Func Ecol 4: 233–242.

Winemiller, K. O., Tarim, S., Shormann, D., and Cotner, J. B., 2000. Fish assemblage structure in relation to environmental variation among Brazos River oxbow lakes. Trans Am Fish Soc: 129, 451-468.

Wu, T. Y., 1971. Hydromechanics of swimming propulsion. Part III: Swimming and optimum movements of slender fish with side fins. J Fluid Mech 46: 545–568.

Wu, T. Y., 1977. Introduction to the scaling of aquatic animal locomotion. In Scale Effects in Animal Locomotion, (ed. T. J. Pedley), pp. 203–232. Academic Press, New York.

Yates, G. T., 1983. Hydromechanics of body and caudal fin propulsion. Chapter 6 in Fish Biomechanics. (ed. P. W. Webb and D. Weihs), Praeger Scientific, New York.

Zelditch, M. L, Swiderski, D. L, Sheets, H. D, Fink, W. L., 2004. Geometric Morphometrics for Biologists: a primer. Elsevier Academic Press, San Diego.

APPENDIX A

Variables	**Interpretation**
M	total metabolic rate measured during sustained swimming (*dependent* on U)
U	measured sustained swimming speed (*independent*)
ε	measurement error in M as a function of U, or error in M = *f*(U)
Constants	**Interpretation**
$a_{(e,p)}$	SMR evaluated at U = 0
$b_{(e,p)}$	MTR contains information on aerobic swimming efficiency, which is a measure of the exponential change in ICOS with respect to the change in U
μ	SCOS contains information on aerobic swimming capacity, which is a measure of metabolic power
Compound variables	**Interpretation**
$\left(\frac{M}{a_e}\right)$	$ICOS_e$ is the metabolic increment (by division) due to swimming
$(M - a_p)$	$ICOS_p$ is the metabolic increment (by subtraction) due to swimming
Parameter subscripts	**Interpretation**
e	TEF
p	HPF
Abbreviations	**Interpretation**
HPF	hydrodynamics-based power function
ICOS	increment cost of swimming
MTR	metabolic transport rate
SCOS	standard cost of swimming
SMR	standard metabolic rate
TEF	traditional exponential function

APPENDIX B

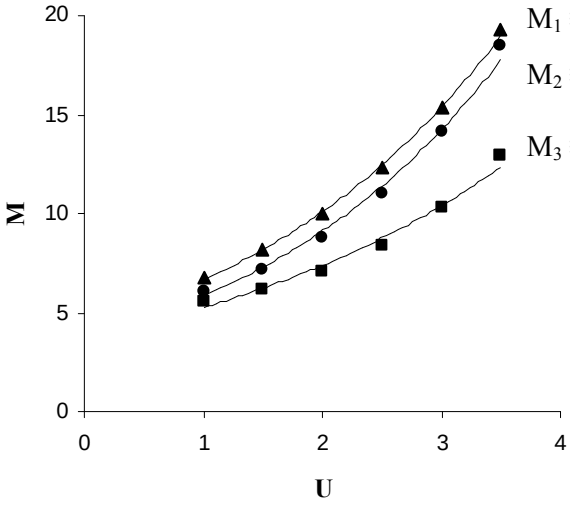

U	M_1	M_2	M_3
1	6.749	6.107	5.526
1.5	8.145	7.220	6.153
2	9.961	8.803	7.083
2.5	12.308	11.023	8.413
3	15.342	14.135	10.298
3.5	19.267	18.523	12.974

Actual (EPF)	**TEF (fit)**	r^2
$M_1 = 5.0e^{0.3U^{1.2}}$	$M_1 = 4.36e^{0.42U}$	0.998
$M_2 = 5.0e^{0.2U^{1.5}}$	$M_2 = 4.74e^{0.45U}$	0.993
$M_3 = 5.0e^{0.1U^{1.8}}$	$M_3 = 3.73e^{0.34U}$	0.983

VITA

Anthony Papadopoulos
4901 4th Street Apt.# 62
Lubbock, TX 79416

Education

2007	Ph.D.	Texas A&M University	Wildlife & Fisheries Sciences
2002	M.S.	Texas A&M University	Biomedical Engineering
2000	B.S.	Syracuse University	Bioengineering

Honors and Awards

2006	Fellowship to attend the NSF Geometrics Morphometrics Workshop, Iowa State University—Instructors: Dean C. Adams (Iowa State University), F. James Rohlf (SUNY Stony Brook), Dennis E. Slice (University of Vienna)
2003	Retroactive Scholarship Award ($1010) – for high productivity in research, Dept. of Health & Kinesiology, Texas A&M University
2002	Tuition Fellowship Award ($3000), Dept. of Health & Kinesiology, Texas A&M University
2002	Student Travel Award ($250), American Society for Gravitational and Space Biology Conference, Cape Canaveral, Florida
2002	4th Place Student Manuscript Award ($100), American College of Sports Medicine – Texas Chapter, Southwestern University
1999	Sigma Xi (Neuroscience Honorary Society), Syracuse University
1998	Harold Mitchel Scholarship, Syracuse University
1996-2000	Phi Eta Sigma National Honorary Society, Syracuse University

Publications

Papadopoulos A, Delp MD (2004) Vascular adaptation to microgravity – Reply. *J. Appl. Physiol.* 97: 1585-1587.

Papadopoulos A, Delp MD (2003) Effects of hindlimb unweighting on the mechanical and structure properties of the rat abdominal aorta. *J. Appl. Physiol.* 94: 439-445.

Muller-Delp J, Spier SA, Ramsey MW, Lesniewski LA, Papadopoulos A, Humphrey JD, Delp MD (2002) Effects of aging on vasoconstrictor and mechanical properties of rat skeletal muscle arterioles. *Am. J. Physiol. - Heart Circ. Physiol.* 282: H1843-H1854.

Papadopoulos A (*Physiol. Biochem. Zool.*, in review) On the hydrodynamics-based power function and its application in fish swimming energetics.